Advanced trapping of light in resonant dielectric metastructures for nonlinear optics

Kirill Koshelev

A thesis submitted for the degree of
Doctor of Philosophy of
The Australian National University

August, 2022

This page is intentionally left blank.

Declaration

This thesis is an account of research undertaken between March 2018 and February 2022 at the Nonlinear Physics Centre (Department of Fundamental and Theoretical Physics), Research School of Physics at The Australian National University while enrolled in the Doctor of Philosophy degree.

The research was carried out under the supervision of Dr. Sergey Kruk, Prof. Ilya Shadrivov and Prof. Yuri Kivshar.

Except where acknowledged in the customary manner, the material presented in this thesis is, to the best of my knowledge, original and has not been submitted in whole or part for a degree in any university.

Kirill Koshelev

August, 2022

List of publications

Papers in peer-reviewed journals with the results included in this thesis

(1) **K. Koshelev**, S. Lepeshov, M. Liu, A. Bogdanov, Yu. Kivshar, "Asymmetric metasurfaces and high-Q resonances governed by bound states in the continuum," Phys. Rev. Lett. **121**, 193903 (2018). DOI: 10.1103/PhysRevLett.121.193903

(2) L. Carletti, **K. Koshelev**, C. De Angelis, and Yu. Kivshar, "Giant nonlinear response at the nanoscale driven by bound states in the continuum," Phys. Rev. Lett. **121**, 033903 (2018). DOI: 10.1103/PhysRevLett.121.033903

(3) **K. Koshelev**, A. Bogdanov, Yu. Kivshar, "Meta-optics and bound states in the continuum," Science Bulletin (special issue) **64**, 836 (2019). DOI: 10.1016/j.scib.2018.12.003

(4) A. A. Bogdanov, **K. Koshelev**, P. V. Kapitanova, M. V. Rybin, S. S. Gladyshev, Z. F. Sadrieva, K. B. Samusev, Yu. S. Kivshar, and M. F. Limonov, "Bound states in the continuum and Fano resonances in the strong mode coupling regime," Advanced Photonics **1**, 016001 (2019). DOI: 10.1117/1.AP.1.1.016001

(5) **K. Koshelev**, G. Favraud, A. Bogdanov, Yu. Kivshar, and A. Fratalocchi, "Nonradiating photonics with resonant dielectric nanostructures," Nanophotonics **8**, 725 (2019). DOI: 10.1515/nanoph-2019-0024

(6) **K. Koshelev**, Y. Tang, K. Li, D.-Y. Choi, G. Li, Yu. Kivshar, "Nonlinear metasurfaces governed by bound states in the continuum," ACS Photonics **6**, 1639 (2019). DOI: 10.1021/acsphotonics.9b00700

(7) **K. Koshelev**, A. Bogdanov, Yu. Kivshar, "Engineering with Bound States in the Continuum," Optics&Photonics News **31**, 38-45 (2020). DOI: 10.1364/OPN.31.1.000038

(8) **K. Koshelev**, S. Kruk, E. V. Melik-Gaykazyan, J.-H. Choi, A. Bogdanov, H.-G. Park, Yu. Kivshar, "Subwavelength dielectric resonators for nonlinear nanophotonics", Science **367**, 288-292 (2020). DOI: 10.1126/science.aaz3985

(9) (Equal first authors) N. Bernhardt[*], **K. Koshelev**[*], S. White, K. W. Ch. M., J. E. Fröch, S. Kim, T. T. Tran, D.-Y. Choi, Yu. Kivshar, A. S. Solntsev, "Quasi-BIC Resonant En-

---

[*] Equal contributions

hancement of Second-Harmonic Generation in WS2 Monolayers," Nano Letters **20**, 5309–5314 (2020). DOI: 10.1021/acs.nanolett.0c01603

(10) **K. Koshelev**, Yu. Kivshar, "Dielectric resonant metaphotonics," ACS Photonics (special issue) **8**, 102–112 (2021). DOI: 10.1021/acsphotonics.0c01315

(11) (Equal first authors) M. Odit*, **K. Koshelev***, S. Gladyshev, K. Ladutenko, Yu. Kivshar, A. Bogdanov, "Observation of supercavity modes in subwavelength dielectric resonators," Advanced Materials **33**, 2003804 (2021). DOI: 10.1002/adma.202003804

(12) E. Melik-Gaykazyan, **K. Koshelev**, J.-H. Choi, S. Kruk, A. Bogdanov, H.-G. Park, Yu. Kivshar, "From Fano to quasi-BIC resonances in individual dielectric nanoantennas," Nano Letters **21**, 1765–1771 (2021). DOI: 10.1021/acs.nanolett.0c04660

(13) (Equal first authors) I. Sinev*, **K. Koshelev***, Zh. Liu*, A. Rudenko, K. Ladutenko, A. Shcherbakov, Z. Sadrieva, M. Baranov, T. Itina, J. Liu, A. Bogdanov, Yu. Kivshar, "Observation of Ultrafast Self-Action Effects in Quasi-BIC Resonant Metasurfaces," Nano Letters **21**, 8848–8855 (2021). DOI: 10.1021/acs.nanolett.1c03257

(14) (Equal first authors) G. Zograf*, **K. Koshelev***, A. Zalogina*, V. Korolev*, D.-Y. Choi, M. Zurch, C. Spielmann, B. Luther-Davies, D. Kartashov, S. Makarov, S. Kruk, Yu. Kivshar, "High-harmonic generation from resonant dielectric metasurfaces empowered by bound states in the continuum," ACS Photonics **9**, 567–574 (2022). DOI: 10.1021/acsphotonics.1c01511

Preprints with the results included in this thesis

(1) **K. Koshelev**, Z. Sadrieva, A. Shcherbakov, Yu. Kivshar, A. Bogdanov, "Bound states in the continuum in photonic structures," arXiv preprint, arXiv:2207.01441 (2022).

Other papers in peer-reviewed journals

(1) L. Wang, S. Kruk, K. Koshelev, I. Kravchenko, B. Luther-Davies, Yu. Kivshar, "Nonlinear wavefront control with all-dielectric metasurfaces," Nano Lett. **18**, 3978 (2018). DOI: 10.1021/acs.nanolett.8b01460

(2) K. L. Koshelev, S. K. Sychev, Z. F. Sadrieva, A. A. Bogdanov, and I. V. Iorsh, "Strong coupling between excitons in transition metal dichalcogenides and optical bound states in the continuum," Phys. Rev. B **98**, 161113(R) (2018). DOI: 10.1103/PhysRevB.98.161113

(3) E. V. Melik-Gaykazyan, K. L. Koshelev, J.-H. Choi, S. S. Kruk, H.-G. Park, A. A. Fedyanin, Yu. S. Kivshar, "Enhanced second-harmonic generation with structured light in AlGaAs nanoparticles driven by magnetic response," JETP Letters **109**, 131 (2019). DOI: 10.1134/S0021364019020036

---

*Equal contributions

(4) K. Koshelev, Yu. Kivshar, "Light trapping gets a boost," Nature **574**, 491 (2019). DOI: 10.1038/d41586-019-03143-w

(5) E. Mikheeva, K. Koshelev, D.-Y. Choi, S. Kruk, J. Lumeau, R. Abdeddaim, I. Voznyuk, S. Enoch, Yu. Kivshar, "Photosensitive chalcogenide metasurfaces supporting bound states in the continuum," Optics Express **27**, 33847 (2019). DOI: 10.1364/OE.27.033847

(6) Q. Yang, S. Kruk, Y. Xu, Q. Wang, Y. K. Srivastava, K. Koshelev, I. Kravchenko, R. Singh, J. Han, Yu. Kivshar, and I. Shadrivov, "Mie-resonant membrane Huygens' metasurfaces," Advanced Functional Materials **29**, 1906851 (2020). DOI: 10.1002/adfm.201906851

(7) (Equal first authors) Y. Liang*, K. Koshelev*, F. Zhang*, H. Lin, S. Lin, J. Wu, B. Jia, Yu. Kivshar, "Bound states in the continuum in anisotropic plasmonic metasurfaces," Nano Letters **20**, 6351–6356 (2020). DOI: 10.1021/acs.nanolett.0c01752

(8) (Equal first authors) E. Tiguntseva*, K. Koshelev*, A. Furasova*, P. Tonkaev, V. Mikhailovskii, E. V. Ushakova, D. G. Baranov, T. Shegai, A. A. Zakhidov, Yu. Kivshar, S. V. Makarov, "Room-Temperature Lasing from Mie-Resonant Nonplasmonic Nanoparticles," ACS Nano **14**, 8149–8156 (2020). DOI: 10.1021/acsnano.0c01468

(9) F. J.F. Löchner, A. George, K. Koshelev, T. Bucher, E. Najafidehaghani, A. Fedotova, D.-Y. Choi, Th. Pertsch, I. Staude, Yu. Kivshar, A. Turchanin, F. Setzpfandt, "Second-harmonic generation from MoS2 monolayers enhanced by resonant dielectric metasurfaces," ACS Photonics **8**, 218–227 (2021). DOI: 10.1021/acsphotonics.0c01375

(10) (Equal first authors) Y. Liang*, H. Lin*, K. Koshelev*, F. Zhang, Y. Yang, J. Wu, Yu. Kivshar, B. Jia, "Full-Stokes polarization perfect absorption with diatomic metasurfaces," Nano Letters **21**, 1090–1095 (2021). DOI: 10.1021/acs.nanolett.0c04456

(11) Y. Jahani, E. R. Arvelo, F. Yesilkoy, K. Koshelev, Ch. Cianciaruso, M. De Palma, Yu. Kivshar, H. Altug, "Imaging-based spectrometer-less optofluidic biosensor with dielectric metasurfaces for detection of extracellular vesicles," Nature Communications **12**, 3246 (2021). DOI: 10.1038/s41467-021-23257-y

(12) M.-S. Hwang, H.-Ch. Lee, K.-H. Kim, K.-Y. Jeong, S.-H. Kwon, K. Koshelev, Yu. Kivshar, H.-G. Park, "Ultralow-threshold super-BIC laser," Nature Communications **12**, 4135 (2021). DOI: 10.1038/s41467-021-24502-0

Selected conference talks

(1) Kirill Koshelev, Yuri Kivshar, "Bound states in the continuum empowering resonant plasmonic structures," METANANO 2021, online, dates 13.09.21-17.09.21.

(2) Kirill Koshelev, George Zograf, Viacheslav Korolev, Anastasia Zalogina, Duk-Yong Choi, Richard Hollinger, Barry Luther-Davies, Michael Zurch, Daniil Kartashov, Christian

---

*Equal contributions

Spielmann, Sergey Makarov, Sergey Kruk, Yuri Kivshar, "Generation of High Harmonics in Silicon Metasurfaces Boosted by Bound States in the Continuum," CLEO Europe 2021, dates 21.06.21-25.05.21.

(3) Kirill Koshelev, I. Sinev, Z. Liu, A. Rudenko, K. Ladutenko, A. Shcherbakov, Z. Sadrieva, T. Itina, A. Bogdanov, Y. Kivshar, "Observation of Ultrafast Self-Action Effects in Resonant Dielectric Metasurfaces," CLEO 2021, online, dates 9.05.21 - 14.05.21.

(4) (Invited) Kirill Koshelev, ICYPPT 2021, online, dates 26.04.21-30.04.21.

(5) Kirill Koshelev, George Zograf, Viacheslav Korolev, Anastasia Zalogina, Duk-Yong Choi, Richard Hollinger, Barry Luther-Davies, Michael Zurch, Daniil Kartashov, Christian Spielmann, Sergey Makarov, Sergey Kruk, Yuri Kivshar, "Silicon metasurfaces with bound states in the continuum for high-harmonic generation," 2021 SPIE Optics & Optoelectronics, online, dates 19.04.21 - 23.04.21.

(6) (Extended) Kirill Koshelev, George Zograf, Viacheslav Korolev, Anastasia Zalogina, Duk-Yong Choi, Richard Hollinger, Barry Luther-Davies, Michael Zurch, Daniil Kartashov, Christian Spielmann, Sergey Makarov, Sergey Kruk, Yuri Kivshar, "Bound States in the Continuum for Enhanced Generation of High Optical Harmonics," OSA Advanced Photonics congress 2020, online, dates 13.07.20-16.07.20.

(7) Kirill Koshelev, Sergey Kruk, Mikhail Odit, Elizaveta Melik-Gaykazyan, Jae-Hyuck Choi, Sergey Gladyshev, Konstantin Ladutenko, Hong Gyu Park, Andrey Bogdanov, Yuri Kivshar, "Observation of Supercavity Modes in Individual Subwavelength Dielectric Resonators," CLEO, online, USA, dates 11.05.20-15.05.20.

(8) Kirill Koshelev, Sergey Kruk, Elizaveta Melik-Gaykazyan, Jae-Hyuck Choi, Andrey Bogdanov, Hong Gyu Park, and Yuri Kivshar, "Observation of highly efficient second-harmonic generation at the nanoscale driven by bound states in the continuum", SPIE Photonics West 2020, San Francisco, U.S., dates 01.02.20 - 06.02.20.

(9) Kirill Koshelev, Sergey Kruk, Jae-Hyuck Choi, Elizaveta Melik-Gaykazyan, Andrey Bogdanov, Daria Smirnova, Hong Gyu Park, and Yuri Kivshar, "Observation of Second-Harmonic Generation driven by Bound States in the Continuum," International Conference Metanano 2019, St Petersburg, Russia, dates 15.07.19 - 19.07.19.

(10) K. L. Koshelev, S. K. Sychev, Z. F. Sadrieva, A. A. Bogdanov, I. V. Iorsh, "Light-matter interaction between photonic bound states in the continuum and bright excitons in transition metal dichalcogenides ," International Conference Metanano 2018, Sochi, Russia, dates 17.09.18 - 21.09.18.

(11) K. L. Koshelev, L. Carletti, C. De Angelis, Yu. S. Kivshar, "Giant nonlinear response of subwavelength dielectric resonators enhanced by bound states in the continuum," International Conference "PIERS", Toyama, Japan, dates 01.08.18 – 04.08.18.

(12) Kirill L. Koshelev, Andrey A. Bogdanov, Sergey A. Gladyshev, Zarina F. Sadrieva, P.V. Kapitanova, Mikhail V. Rybin, Kirill B. Samusev, Mikhail F. Limonov, Yuri S. Kivshar, "High-Q supercavity states in high-index subwavelength all-dielectric resonators," International Conference "PIERS", Toyama, Japan, dates 01.08.18 – 04.08.18.

(13) Luca Carletti, Kirill Koshelev, Constantino De Angelis, Yuri Kivshar, "Nonlinear nanophotonics and bound states in the continuum," International Conference “CLEO”, San Jose, USA, Dates 13.05.18-17.05.18.

Acknowledgment

This work would not have been possible without the absolute support of my colleagues, friends, and family.

I am deeply grateful to my primary supervisor Prof. Yuri Kivshar for unlimited support and thorough mentoring he provided me during my PhD journey. I am thankful to Yuri for sharing his genuine passion for optics and photonics. I was lucky to be a part of the Nonlinear Physics Centre headed by Yuri, the world leading research group in many areas of photonics, and I hope to continue my journey here as a postdoc in the coming years. Last but not least, I express a sincere gratitude to Yuri for supporting me unconditionally in very hard personal situations.

My deep appreciation goes to Dr. Andrey Bogdanov, my colleague, life mentor, supervisor and friend. Almost ten years ago, Andrey found me in the chambers of the Ioffe Institute as a young bewildered student who has passion for physics but does not know how shape it. I feel lucky that at that time Andrey offered me a job at the most fascinating research group I was ever associated with, Department of Nanophotonics and Metamaterials of ITMO University. Throughout these years, Andrey helped me to orient and develop my personality as a scientist. Andrey mentored me as a student, as a colleague, as a friend and every time his support was irreplaceable. I feel deeply indebted to Andrey for everything he did for me, for how he protected and guided me in the most complicated situations.

Furthermore, I would like to thank all colleagues and external collaborators who worked together on various projects during my PhD. This includes but is not restricted to my colleagues and collaborators from the Australian National University, ITMO University and a variety of institutions across Australia, Russia and the globe.

Last yet not least, I would like to thank my friends and family for their support. I am highly indebted to my beloved wife Elena Kosheleva, who deeply loves and strongly supports me

every single day independently on how hard my life can be.

Abstract

In the past two decades new frontiers emerged in the rapidly expanding field of nanophotonics that have revolutionized the conventional approaches to the manipulation of electromagnetic radiation at the nanoscale. The remarkable progress in the engineering of efficient nanostructured devices for functional flat optics and nonlinear photonics was achieved by using resonant dielectric metastructures operating through the excitation of Mie resonances and their collective configurations. Further progress in the subwavelength localization of light in Mie-resonant nanostructures and enhancement of their optical nonlinearities remained hampered by the leaky nature of optical modes. The last decade marked the series of intense studies of optical resonances with a giant quality factor, *bound states in the continuum (BICs)*, aimed to resolve this issue. The unique electromagnetic properties of BICs were examined as a versatile tool to tailor the optical response of photonic nanostructures, yet their physical nature and the feasibility of realization in the form of high-quality *quasi-BIC* resonances in planar and compact metadevices remains largely unexplored. Moreover, it remains unknown in many aspects how BICs can be utilized for the engineering of resonant nonlinear metasurfaces and nanoantennas for efficient frequency conversion and the observation of strong nonlinearities.

In this thesis, we are focused on the comprehensive analysis of fundamental physical properties of optical quasi-BICs in resonant dielectric metastructures and exploration of their practical feasibility for strong light confinement and nonlinear applications. We outline the general framework for design and optimization of nanostructured devices supporting quasi-BICs in the visible and infrared range for the maximization of the local fields and associated enhancement of optical nonlinearities. More specifically, we focus on planar *metasurfaces with broken-symmetry meta-atoms*, and *individual subwavelength resonators* with a compact footprint, for which we test the utility of the developed concepts. Ultimately, we target the challenge of engineering of nonlinear dielectric metastructures with outstanding nonlinear performances, which may lead to new breakthroughs in the realization of efficient nonlinear frequency converters, low-threshold nanolasers, and compact quantum sources.

In Chapter 1 we overview the recent developments in the fields of nanophotonics, dielectric meta-optics, and optical BICs. We outline the motivation and structure of the thesis.

In Chapter 2 we propose the concept of light localization in dielectric metasurfaces composed of meta-atoms with a broken in-plane inversion symmetry by using quasi-BICs resonances. We show that the optical response of broken-symmetry metasurfaces can be tailored precisely by changing the asymmetry of the unit cell that induces the controllable change of the quasi-BIC quality factor. With this unified concept we explain the results of numerous earlier studies reporting on sharp Fano resonances, dark modes, metamaterial-induced electromagnetic transparency, trapped resonances in asymmetric plasmonic and dielectric metasurfaces observed in various spectral ranges from the visible to radio frequencies. We further explore the importance of parasitic losses originating due to fabrication imperfections in metasurfaces on the value of the field enhancement. We outline the criteria for the maximization of the local fields in realistic metasurfaces with imperfections by adjusting the structure geometry to satisfy the optimal coupling regime. Using these findings, we propose a universal framework for designing dielectric metasurfaces supporting sharp resonances with a specific operating wavelength and linewidth *on demand*.

Chapter 3 is focused on the analysis and experimental demonstration of nonlinear optical effects in broken-symmetry dielectric metasurfaces supporting quasi-BICs in the near-IR and mid-IR wavelength range. We generalize the optimal coupling criteria for the nonlinear regime for maximization of harmonic generation efficiency for low pump intensities. We design Si metasurfaces for third- and high-harmonic generation and prove experimentally that in the optimal coupling regime the conversion efficiency is maximized. Using the developed optimal coupling model, we demonstrate the enhancement of optical nonlinearities of two-dimensional Van der Waals materials integrated with Si metasurfaces supporting quasi-BICs. For strong field excitation, we demonstrate that Si metasurfaces tuned to the quasi-BIC resonance generate high-harmonic signal with the harmonic order up to the eleventh. We demonstrate pronounced self-action effects for ultrashort sub-picosecond pulse excitation of quasi-BICs in the near- and mid-IR and explain them in the model of resonantly enhanced photoionization of Si.

In Chapter 4 we propose the new mechanism of light trapping in isolated subwavelength dielectric resonators by the formation of quasi-BICs due to the destructive interference of several Mie modes in the far field. For a dielectric disk with a variable aspect ratio we demonstrate that quasi-BICs are manifested as high-Q resonances formed at an avoided resonance crossing of Mie mode dispersion branches. We study the near- and far-field properties of quasi-BICs and show that the cancellation of radiative losses is related to the suppression of the dominant multipolar component of the field. We explore the manifestation of quasi-BICs in the scattering spectra and outline the connection between the maximization of the mode Q factor and the peculiarities of the scattering features. We show that the quasi-BICs can realized in subwavelength dielectric resonators with refractive index more than 2 in various spectral ranges from the visible to microwaves. The findings are verified in proof-of-principle experiments in the near-IR and radiofrequency range.

In Chapter 5 we examine the efficiency of harmonic generation from individual dielectric nanoresonators supporting quasi-BICs and outline the criteria for the maximization of conversion efficiency by optimizing the mode structure, pump spatial and temporal profile, and the environment design. We propose the theoretical model of second-harmonic generation for nanosctructures resonant at the pump and harmonic frequency beyond the phase matching and derive an analytical closed-form expression for the emitted harmonic power. We verify the developed model experimentally and show a record-high measured conversion efficiency of the optimized nonlinear nanoantenna.

Chapter 6 summarizes the results and concludes the thesis.

Contents

List of Abbreviations

BIC	bound state in the continuum
quasi-BIC	quasi-bound state in the continuum
Q factor	quality factor
high-Q	high-quality
ARC	avoided resonance crossing
MD	magnetic dipole
ED	electric dipole
MQ	magnetic quadrupole
EQ	electric quadrupole
SHG	second-harmonic generation
THG	third-harmonic generation
5HG	fifth-harmonic generation
HHG	high-harmonic generation
SH	second-harmonic
TH	third-harmonic
HH	high-harmonic
near-IR	near-infrared
mid-IR	mid-infrared
UV	ultraviolet
CMOS	complementary metal oxide semiconductor
SEM	scanning electron microscopy
EBL	electron beam lithography
TMD	transition metal dichalcogenide
FEM	finite element method

List of Figures

1 Introduction: resonant dielectric meta-optics

1.1 Overview

Nanophotonics and dielectric meta-optics. Nanophotonics is the rapidly developing frontier of optical research dealing with light-matter interaction between electromagnetic waves with frequencies typically in the range from the UV to the near-IR and media structured on the size scale of one to few hundred nanometers [1, 2]. Recent decades had witnessed striking progress in applying the physical concepts of nanophotonics to engineer efficient devices for diverse applications in nanoscale technologies, optical communication, ultrafast computation and advanced optoelectronics [3]. Historically, one of the first major research directions in nanophotonics is plasmonics that deals with deeply subwavelength localization of light in metallic nanoparticles or at metallic interfaces due to collective excitations of conduction electrons [4, 5]. Many efforts were done to develop plasmonic nanostructures with advanced optical properties for applications in biosensing, quantum technologies, photovoltaics [6–8]. Despite fast progress and many promising applications, practical use of plasmonic devices for complete control of electromagnetic radiation amplitude and phase was shown to be limited drastically, especially at visible frequencies. The major challenges plasmonics is facing are associated with high optical losses, low damage threshold and incompatibility with the standardized CMOS fabrication technologies. Moreover, the magnetic response of metallic nanostructures is weak and its enhancement requires designing of particles with sophisticated geometries [9].

The last decade has been marked by emergence of a new branch of nanophotonics, *dielectric meta-optics*, also called *Mie-tronics*, that combines studies of light manipulation with resonant nanostructures made of semiconductors and high-index dielectrics [19–21]. High-refractive index and low optical losses of most common dielectric materials, such as Si, Ge, GaAs, in the visible and infrared ranges allow for light confinement at a scale much smaller than the wavelength in the free-space via excitation of geometrical (Mie) resonances of the nanostructures [22]. In the recent years dielectric meta-optics attracted widespread interest as a flexible platform for light localization and strong enhancement of the near-field at the nanoscale and promising alternative to plasmonics. Moreover, metastructures composed of dielectric meta-atoms were shown to outperform their plasmonic counterparts in a variety of applications due to superior inherent material and resonant properties allowing for advanced control of the radiation wavefront and light confinement. More specific, the semi-

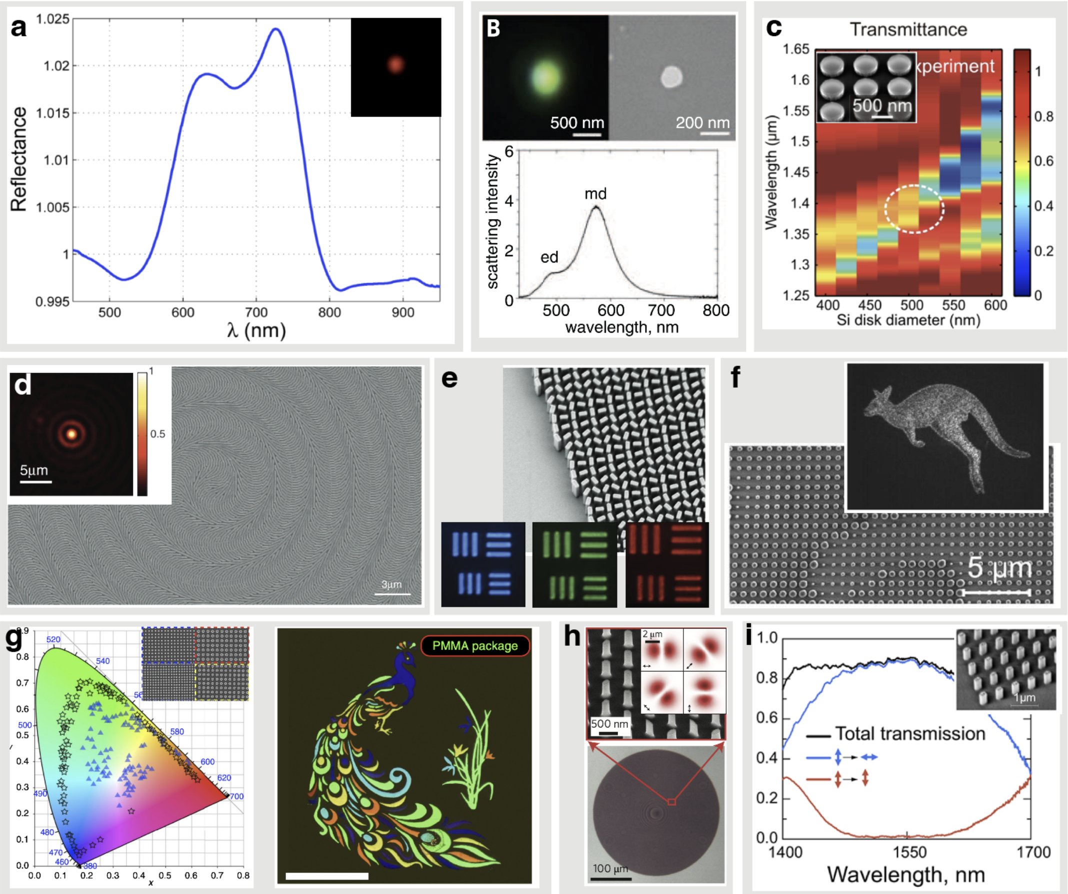

Figure 1.1: Dielectric metastructures in nanophotonics. (a, b) Observation of optical magnetic response in dielectric nanoparticles. (c) Directional scattering at overlapping electric and magnetic dipole resonances. (d-i) Functional dielectric metasurfaces. (d-e) Geometric phase lens for focusing and imaging. (f) Huygens' metasurface hologram. (g) Generation of structured colors. (h-i) Polarzation control with Q plates (h) and waveplates (i). (a) is adapted from [10], (b) is adapted from [11], (c) is adapted from [12], (d) is adapted from [13], (e) is adapted from [14], (f) is adapted from [15], (g) is adapted from [16], (h) is adapted from [17], (i) is adapted from [18]

conductor nature of common high-index dielectrics removes the constraints of compatibility with CMOS fabrication processes and manipulation with carrier density allows for tunability of optical response. The resonant response of dielectric metastructures is driven by excitation of Mie resonances, that represent displacement currents, thus both electric- and magnetic-type response can be observed with comparable strengths [10, 11, 23–25], see Figs. 1.1a,b. The simplicity of realization of magnetic response allows to engineer nanoantennas for efficient control of directionality and expands the range of functionalities of dielectric nanostructures as building blocks of functional devices [12, 26], see Fig. 1.1c.

Dielectric metasurfaces, that represent ordered two-dimensional arrays of subwavelength dielectric meta-atoms, attract special attention among other metastructures because of their high potential for flat optics as compact devices for control of amplitude, phase, polarization and propagation direction of a wavefront of light [27–29]. The main principles governing response of dielectric metasurfaces are related to the physics of Huygens' surfaces, reso-

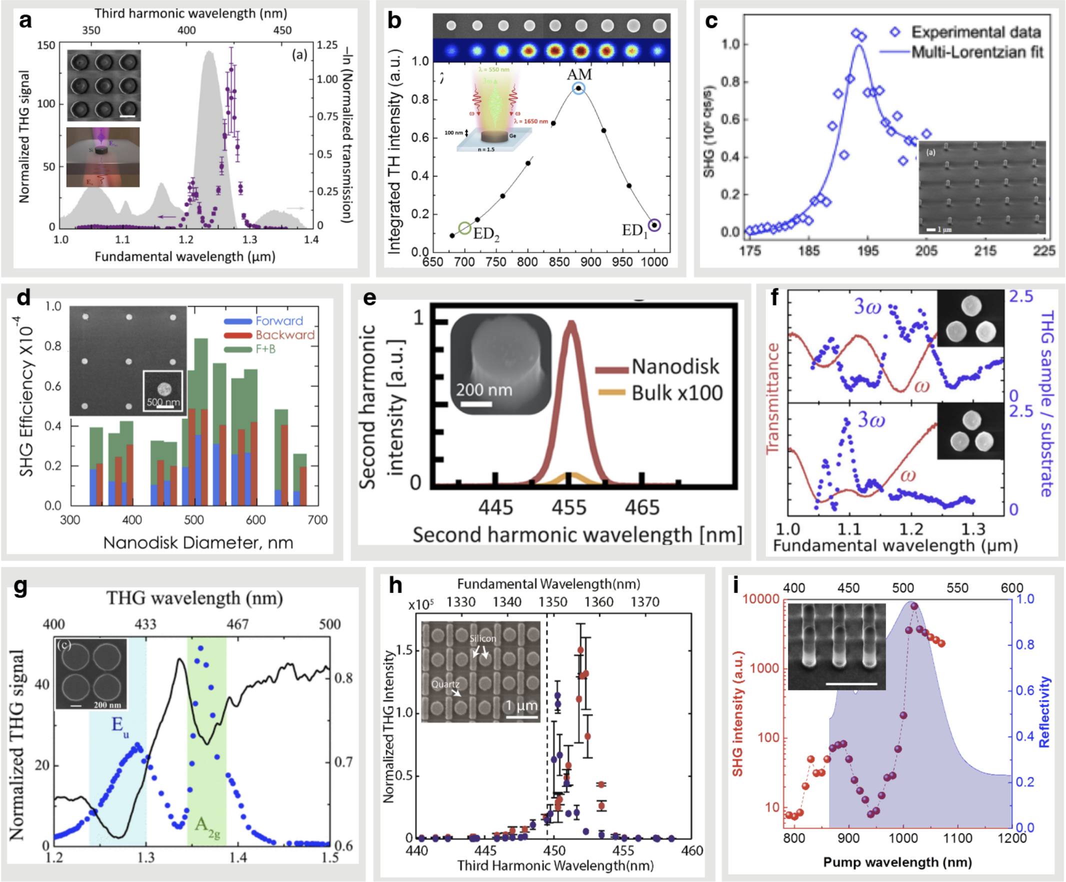

Figure 1.2: Generation of optical harmonics with resonant dielectric metastructures. (a-b) THG in Mie-resonant nanoparticles. (c-e) SHG in Mie-resonant nanoparticles. (f-g) THG in oligomers. (h-i) THG (h) and SHG (i) in metasurfaces. (a) is adapted from [35], (b) is adapted from [36], (c) is adapted from [37], (d) is adapted from [38], (e) is adapted from [39], (f) is adapted from [40], (g) is adapted from [41], (h) is adapted from [42], (i) is adapted from [43].

nant phase, form birefringence, and geometric phase [18, 30–32]. Recent studies demonstrate highly efficient dielectric metasurfaces based on these principles for image differentiation, vortex and hologram generation, beam deflection, creation of compact lenses, structured colouring [13–17, 33, 34], see Figs. 1.1d-i. In addition to high efficiency of wavefront control, functional dielectric metasurfaces provide extra degrees of freedom inaccessible in conventional diffractive optics. They include ultrasmall device footprint, strong effective birefringence with high spatial resolution of gradients, and scalability of fabrication.

Nonlinear meta-optics. In the last decade, active and nonlinear metastructures attract widespread interest of the nanophotonics community, especially, *nonlinear resonant metasurfaces*. Nonlinear metasurfaces are expected to meet the growing demand for tailored nonlinear optical response, combining nonlinear wavefront engineering and efficient frequency conversion at the subwavelength scale. Strong nonlinear response from optically thin structures requires enhancement of light-matter interactions beyond the values that can be achieved in non-resonant bulk nonlinear media. First, plasmonic nonlinear metasurfaces

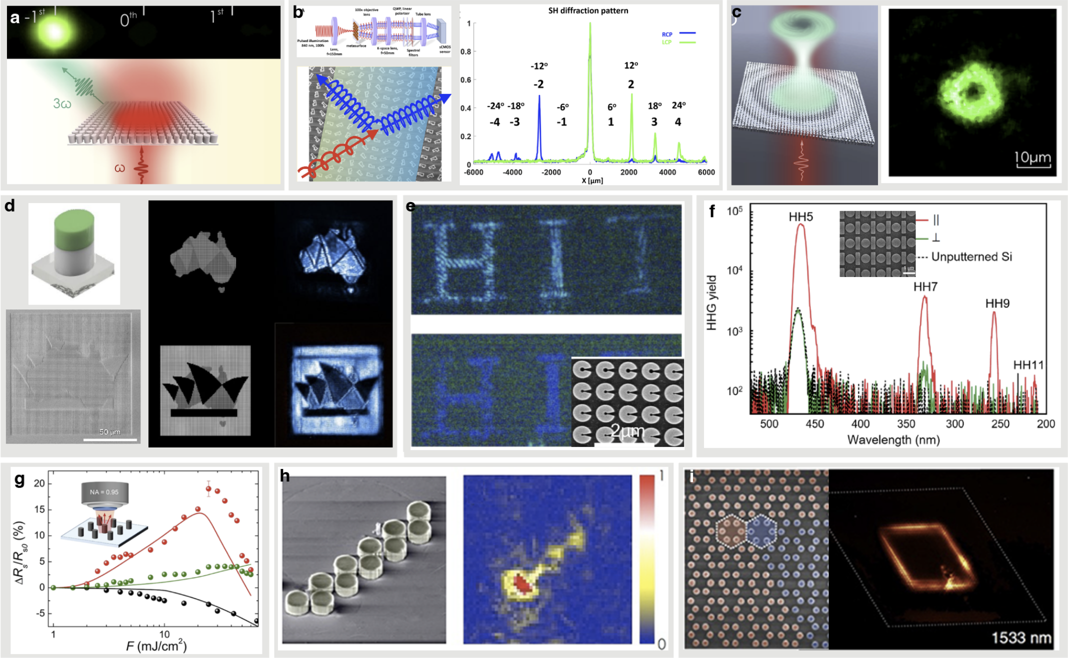

Figure 1.3: Functional and topological nonlinear optics with dielectric metasurfaces. (a-b) Nonlinear beam steering. (c) Nonlinear vortex generation. (d) Asymmetric parametric generation of images. (e) Nonlinear holography. (f) Generation of high-harmonics. (i) Ultrafast optical switching. (h-i) Topologically-nontrivial nonlinear metasurfaces. (a) and (c) is adapted from [44], (b) is adapted from [45], (d) is adapted from [46], (e) is adapted from [47], (f) is adapted from [48], (g) is adapted from [49], (h) is adapted from [50], (i) is adapted from [51].

were suggested to enlarge light-matter interaction by exploiting strong fields at metallic surfaces originating from inherently large nonlinear susceptibility of metals [52]. However, low damage threshold due to energy dissipation into heat and small mode volumes limit strongly the efficiency of nonlinear optical processes in plasmonic nonlinear metasurfaces and the focus of studies has shifted towards dielectric nonlinear metasurfaces [53–55]. Large bulk nonlinearities of many common dielectrics combined with strong resonant field enhancement and overlapping of Mie resonances with the volume of material make nonlinear dielectric metasurfaces a promising platform for observation of nonlinear optical processes. Strong Mie resonances represent a natural way to enhance the parametric signal at the subwavelength scale beyond the traditional phase-matching with high efficiency potentially comparable to the conversion efficiency of macroscopic nonlinear crystals. First studies of Mie-driven harmonic generation in individual dielectric nanoparticles and oligomers demonstrated very large improvement of conversion efficiencies up to the scale of $10^{-5}-10^{-4}$% for third-harmonic signal [35, 36, 40] and $10^{-3}-10^{-2}$% for the second-harmonic signal [37–39], see Figs. 1.2a-g. Moreover, resonant excitation of Mie modes of magnetic nature were shown to produce nonlinear magnetic response from dielectric metastructures [41, 56, 57]. Using the concept of Mie resonances, a large number of examples of nonlinear dielectric metasurfaces was demonstrated for second- and third-harmonic generation [42, 43, 58] with reasonably high efficiencies far much exceeding the efficiencies of their plasmonic analogues, see

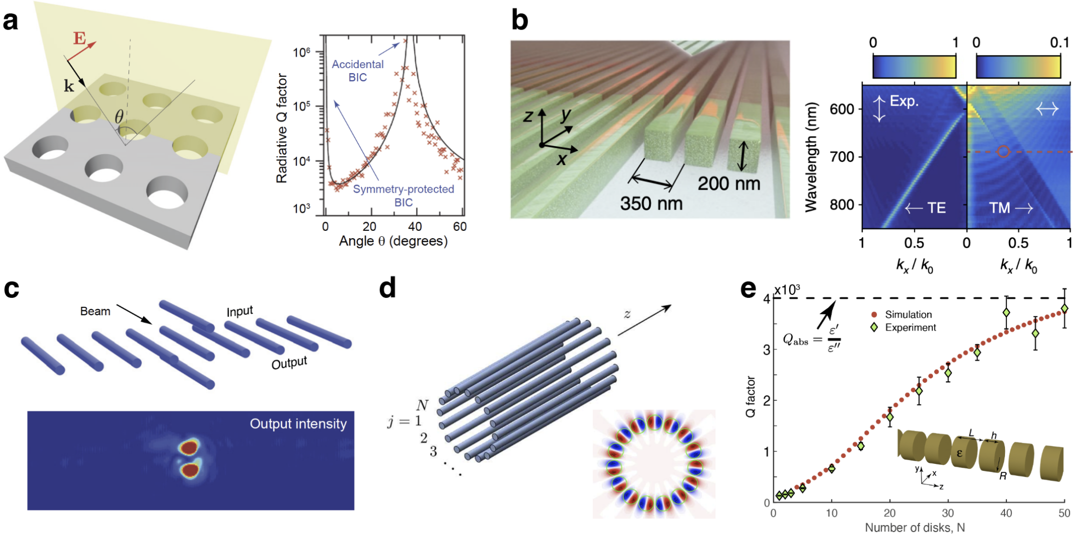

Figure 1.4: Optical bound states in the continuum (BICs) in photonic dielectric structures. (a) Photonic crystal slabs. (b) Gratings. (c) Waveguides with defects. (d) Circular arrays of waveguides. (e) Chains of subwavelength resonators. (a) is adapted from [64], (b) is adapted from [65], (c) is adapted from [66], (d) is adapted from [67], (e) is adapted from [68].

Figs. 1.2h-i.

Recent progress in engineering of dielectric metasurfaces with enhanced optical nonlinearities paved the way towards wavefront manipulation in the nonlinear regime. The principles of resonant and geometric phase extended to the nonlinear regime allowed for encoding of the predefined phase pattern in shape and geometry of the meta-atoms producing structured wavefront while keeping the conversion efficiency at the maximum level. As a result, nonlinear phase control was used for efficient beam steering, vortex generation, holography, imaging, asymmetric parametric generation of images [44–47, 59], see Figs. 1.3a-e. In addition, strong optical response allowed for development of broadband frequency mixers and observation of ultrafast optical switching and high-harmonic generation [48, 49, 60–63], see Figs. 1.3f-g. Moreover, enhanced nonlinearities in metasurfaces enabled engineering of photonic systems with nontrivial topological properties manifested in the nonlinear response [50, 51], see Figs. 1.3h-i.

Light trapping with bound states in the continuum. Further enhancement of optical nonlinearities in resonant dielectric metastructures remains hampered by the leaky nature of optical modes. The rate of radiative energy leakage of the modes defining the strength of the local fields depends on the degree of light confinement inside the structure, i.e. on the quality of the structure as an optical resonator. Thus, the key concept underlying the improvement of functionalities of many linear and nonlinear metastructures is the use of constituent elements characterized by high quality factors (Q factors) of the resonances. A typical optical resonator traps light by the use of total internal reflection effect or multiple back-scatterings from periodic structures such as photonic crystals. Efficiency of light trapping in resonators characterized by the mode Q factor is weakly dependent on the resonator geometry but de-

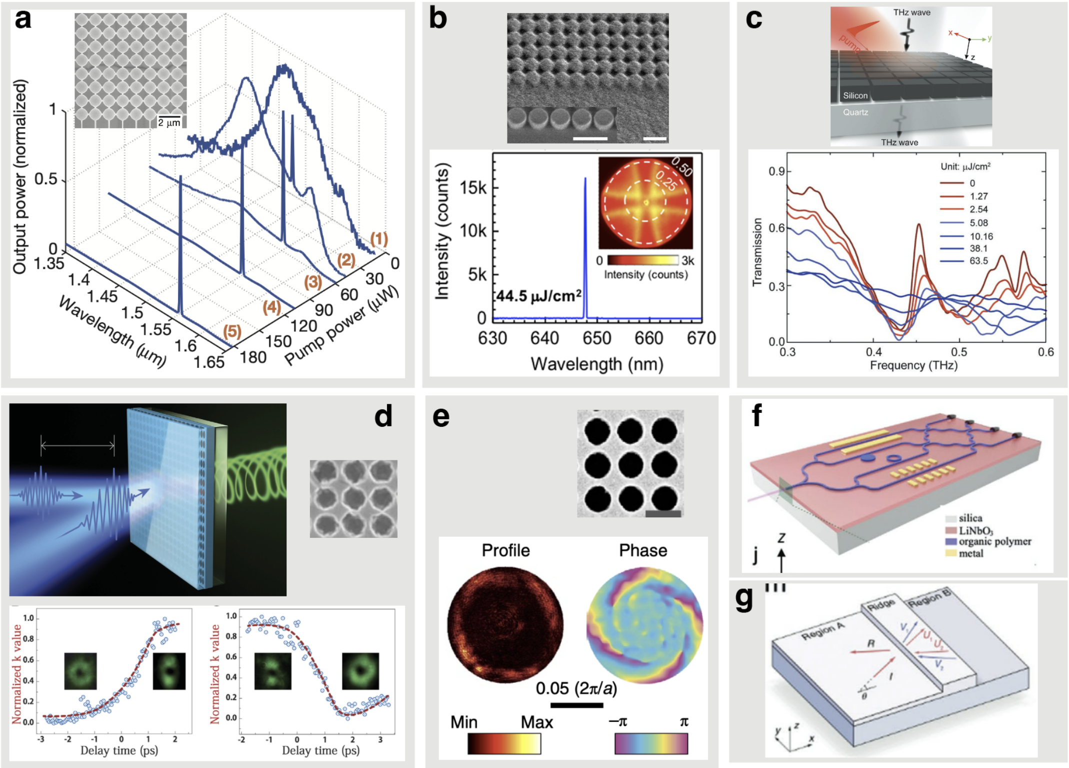

Figure 1.5: Selected applications of optical quasi-BICs in dielectric metastructures. (a,b) Low-threshold lasing. (c) Active terahertz photonics. (d,e) Vortex generation. (f,g) Integrated photonic devices: photonic circuit (f) and Gires–Tournois interferometer (g). (a) is adapted from [71], (b) is adapted from [72], (c) is adapted from [73], (d) is adapted from [74], (e) is adapted from [75], (f) is adapted from [76], (g) is adapted from [77].

pends strongly on the quality of "mirrors" that confine the radiation. The standard ways to increase the Q factor rely on increase of the structure size or applying complex designs to confine light, such as cavities in photonic bandgap structures [69] or whispering-gallery-mode resonators [70]. For subwavelength dielectric nanostructures, Mie theory predicts relatively low values of the quality factor, e.g. in the visible and near-IR range the Q factor is of order of 5 to 10 for nanoparticles made of conventional optical materials such as Si, Ge, and AlGaAs [20]. The Mie modes in metasurfaces possess a higher Q factor up to 50 due to multi-particle interferences but its value is still insufficient for strong local field enhancement.

This thesis aims to explore the advanced physical mechanisms of strong light confinement in resonant dielectric metastructures by using the physics of mode interferences for enhancement of local fields and associated increase of optical nonlinearities. The most recent and promising frontier in that field is *bound states in the continuum* (BICs), that represent special optical resonances embedded into the continuous spectrum of the environment but decoupled from the radiation [78, 79]. Along with Fano resonances [80, 81] and nonradiating dynamic current configurations in the form of optical anapoles [82–84], they provide a way to increase the local fields in dielectric metastructures. Historically, BICs were predicted nearly a century ago as a mathematical curiosity in quantum mechanics [85], but as a universal wave phenomenon they were later identified in atomic physics, acoustics, hydrodynamics and elastic waves in solids. In photonics, the BICs were re-discovered only in the recent decade as a simple tool to achieve very large Q factor required for enhancement light matter interaction [66, 86, 87]. The physical properties of optical BICs were analysed theoretically and experimentally for a variety of photonic dielectric metastructures, including waveguides with defects, gratings [88–93], photonic crystal slabs and metasurfaces [64, 94–100], chains of nanoparticles [68, 101–104], see examples in Figs. 1.4a-e.

In practice, infinitely high Q factors of BICs are limited by a finite size of samples, material absorption, structural disorder and surface scattering [105]. As a result, BICs are transformed into states with a giant Q factor often treated as quasi-BICs. Quasi-BICs in dielectric metastructures were shown to be advantageous for a wide span of applications, including lasing, active terhertz photonics, polaritonics, photonic integrated circuits and integrated Gires–Tournois interferometer, and biophotonics and sensing [71–73, 76, 77, 106–111], see Figs. 1.5a-c,f,g. Optical BICs were shown to demonstrate topological stability against perturbations, preserving structural symmetry [112]. Due to their topological properties they represent vortex centers in the polarization directions of far-field radiation, which carry conserved and quantized topological charges. This property was realized for quasi-BICs and used for vortex generation [65, 74, 75, 113], see Figs. 1.5d-e. Their polarization properties were used to engineer uniderectional high-Q resonances [114]. Later, a concept of super-BIC was suggested by merging several BICs in the wavevector space and producing a resonance with increased robustness to the fabrication disorders that allowed to observe sharp resonances with Q more that 10^5 in photonic crystal slabs and membranes [115, 116]. The super-BICs shown their potential for lasing applications because of record-low threshold [117]. Very recently, chiral BICs and quasi-BICs were studied in application to generation of strong chiroptical signals [118–120].

1.2 Motivation and thesis outline

The recent decade marks a series of intense studies of optical quasi-BICs in nanostructured materials, however, their physical nature in many systems, feasibility of their realization in form of high-Q resonances in planar metasurfaces and their potential for nonlinear optics remain largely unexplored. This thesis aims at addressing key challenges with a scope of both fundamental and practical interests on how one can make use of optical quasi-BICs in dielectric metasurfaces and their meta-atoms, *individual subwavelength resonators*, in the linear and nonlinear regime. We explore the physical mechanisms determining the formation of quasi-BICs in these structures and study how the system geometry can be tuned to maximize the mode quality factor (Chapter 2 and Chapter 4). We outline the general framework for design and optimization of resonant dielectric metastructures supporting quasi-BICs within the frequency range of interest and maximization of the local field enhancement and associated enhancement of optical nonlinearities. We target the challenge of engineering of nonlinear dielectric metastructures with outstanding nonlinear performances, which may lead to

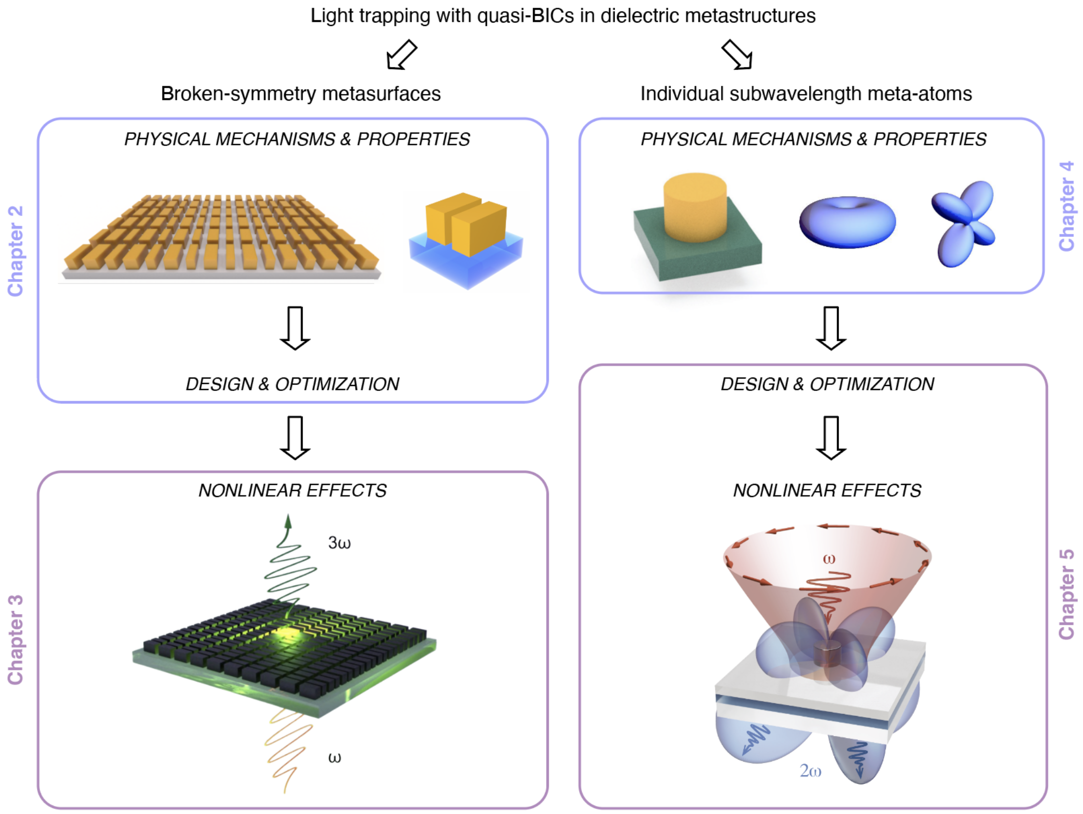

Figure 1.6: Thesis outline and organization.

new breakthroughs in realization of efficient nonlinear frequency converters, low-threshold nanolasers, and compact quantum sources (Chapter 3 and Chapter 5).

A more detailed outline of the chapter structure and content is provided below and schematically shown in Fig. 1.6.

Chapters 2 and 3 target light trapping with quasi-BICs and enhancement of optical nonlinearities in dielectric metasurfaces with broken in-plane inversion symmetry. In Chapter 2 we reveal that metasurfaces created by seemingly different lattices of asymmetric meta-atoms can support high-Q quasi-BICs arising from a distortion of symmetry-protected BICs. We show that Q factor of the quasi-BICs can be tuned by the degree of the meta-atom asymmetry. Using this tunability, we outline the criteria for the maximization of the local field enhancement in realistic metasurfaces with parasitic losses due to fabrication imperfections by adjusting the structure to the optimal coupling regime. We present a general procedure to design sharp resonance with a specific operating wavelength and linewidth in dielectric metasurfaces by the use of scalability of Maxwell's equations and properties of quasi-BICs. This new approach forms an versatile tool for engineering of resonant metasurfaces on demand for applications relying on strong local field enhancement.

Chapter 3 is focused on analysis and experimental demonstration of nonlinear optical effects in broken-symmetry dielectric metasurfaces supporting quasi-BICs in the near-IR and mid-IR. We generalize the optimal coupling criteria for the nonlinear regime and derive the condition of maximization of harmonic generation in the limit of weak field excitation. We design Si metasurfaces for third- and high-harmonic generation and prove experimentally that in the optimal coupling regime the conversion efficiency can be boosted dramatically. In the regime of strong field interaction we achieve high-harmonic generation and strong self-action at the quasi-BIC resonance in Si metasurfaces. We explain the self-action in the model of free-carrier generation and demonstrate modification of metasurface resonant properties due to change of material parameters. We outline the strategy to increase optical nonlinearities of two-dimensional Van der Waals materials substantially by integrating them with resonant Si metasurfaces supporting quasi-BICs.

Chapters 4 and 5 are devoted to light trapping with quasi-BICs in individual subwavelength dielectric meta-atoms, their practical realization and potential for nonlinear applications. In Chapter 4 we propose a new mechanism of electromagnetic radiation localization in isolated subwavelength resonators by formation of quasi-BICs due to destructive interference of several Mie modes in the far field. For a dielectric disk with variable aspect ratio we show numerically and experimentally that quasi-BICs are manifested as high-Q resonances formed at avoided resonance crossing of Mie mode dispersion branches. We study the near- and far-field properties of quasi-BICs and show that the cancellation of radiative losses is related to the suppression of the dominant multipolar component of the field. We explore the manifestation of quasi-BICs in the scattering spectra and outline the connection between maximization of the mode Q factor and the peculiarities of the scattering features.

In Chapter 5 we examine the efficiency of harmonic generation from individual dielectric nanoresonators supporting quasi-BICs and outline the criteria for maximization of conversion efficiency by optimizing the mode structure, the pump spatial and temporal profile and the environment design. In more detail, we propose a theoretical model of SHG for nanostructures resonant at the pump and harmonic frequency beyond the phase matching and derive the analytical closed-form expression for the emitted SH power. We prove experimentally the theoretical and numerical results and show that the measured conversion efficiency of the optimized nonlinear nanoantenna at the quasi-BIC exceeds the efficiencies of SHG reported earlier for non-BIC plasmonic and dielectric nanoantennas by more than two orders of magnitude.

Finally, in Chapter 6 we outline the main conclusions for this thesis and provide a discussion on potential future studies in the field.

The overview of the field of optical BICs and quasi-BICs in dielectric meta-optics and resonant nanophotonics, highlighting the results described in this thesis is outlined in four published Review articles and one Review preprint with my lead contribution

(1) **K. Koshelev**, A. Bogdanov, Yu. Kivshar, "Meta-optics and bound states in the continuum," Science Bulletin (special issue) **64**, 836 (2019). DOI: 10.1016/j.scib.2018.12.003

(2) **K. Koshelev**, G. Favraud, A. Bogdanov, Yu. Kivshar, and A. Fratalocchi, "Nonradiating photonics with resonant dielectric nanostructures," Nanophotonics **8**, 725 (2019).

DOI: 10.1515/nanoph-2019-0024

(3) **K. Koshelev**, A. Bogdanov, Yu. Kivshar, "Engineering with Bound States in the Continuum," Optics&Photonics News **31**, 38-45 (2020). DOI: 10.1364/OPN.31.1.000038

(4) **K. Koshelev**, Yu. Kivshar, "Dielectric resonant metaphotonics," ACS Photonics (special issue) **8**, 102–112 (2021). DOI: 10.1021/acsphotonics.0c01315

(5) **K. Koshelev**, Z. Sadrieva, A. Shcherbakov, Yu. Kivshar, A. Bogdanov, "Bound states in the continuum in photonic structures," arXiv preprint, arXiv:2207.01441 (2022).

2 Light trapping in metasurfaces with broken in-plane symmetry

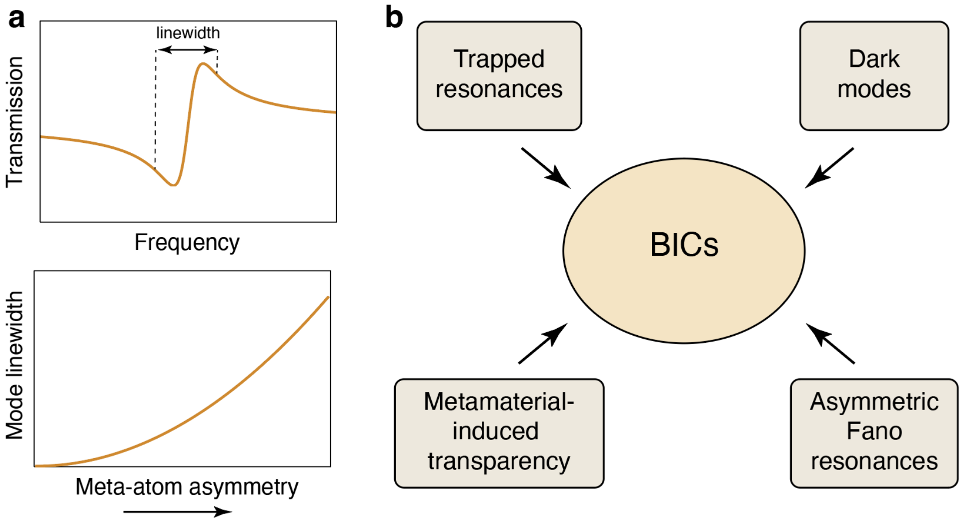

Figure 2.1: (a) Schematic of transmission spectrum and mode linewidth dependence on asymmetry in broken-symmetry metasurfaces. (b) Connection between BICs and other resonant effects observed in broken-symmetry metasurfaces.

Metasurfaces with a broken symmetry unit cell operating in different frequency ranges from microwaves to infrared attracted widespread attention in the last two decades. Many studies considered asymmetric plasmonic and dielectric metasurfaces demonstrating sharp resonances in transmission or reflection for the normal incidence excitation, which resonant linewidth depends strongly on the asymmetry of the meta-atom, as shown schematically in Fig. 2.1a. The observed effect was associated with trapped resonances in arrays of dielectric nanodisks [121] and split-ring structures [122, 123], Fano resonances [124–128], electromagnetically-induced transparency [129–133], and dark modes [134–136].

In this chapter, we generalize the findings on resonant properties of asymmetric metasurfaces and show that all of these effects are a manifestation of bound states in the continuum (BICs) as shown schematically in Fig. 2.1b. First, we make an introduction to the physics of BICs in periodic photonic structures, explaining the mechanism of their formation and main properties. Next, we present a general concept of quasi-BICs in broken-symmetry dielectric metasurfaces, formed from symmetry-protected BICs due to symmetry breaking, and derive the dependence of the Q factor on the asymmetry parameter. We associate the high-quality quasi-BICs with the peculiarities in scattering and derive the generalized Fano formula for transmission using the quasi-normal mode expansion of the Green's function. We study the effect of parasitic and non-radiative losses and derive the criteria for the maximization of the local field enhancement. Finally, we present a general procedure to design sharp resonance with a specific operating wavelength and linewidth in dielectric metasurfaces by the use of scalability of Maxwell's equations and properties of quasi-BICs.

Results presented in this chapter are partially included in the published References, listed below, where I am a lead author and my contribution is in theoretical aspects, numerical simulations, metasurface design and writing of the first draft of the paper

(1) **K. Koshelev**, S. Lepeshov, M. Liu, A. Bogdanov, Yu. Kivshar, "Asymmetric metasurfaces and high-Q resonances governed by bound states in the continuum," Phys. Rev. Lett. **121**, 193903 (2018). DOI: 10.1103/PhysRevLett.121.193903

(2) **K. Koshelev**, Y. Tang, K. Li, D.-Y. Choi, G. Li, Yu. Kivshar, "Nonlinear metasurfaces governed by bound states in the continuum," ACS Photonics **6**, 1639 (2019). DOI: 10.1021/acsphotonics.9b00700

(3) (Equal first authors) N. Bernhardt*, **K. Koshelev***, S. White, K. W. Ch. M., J. E. Fröch, S. Kim, T. T. Tran, D.-Y. Choi, Yu. Kivshar, A. S. Solntsev, "Quasi-BIC Resonant Enhancement of Second-Harmonic Generation in WS2 Monolayers," Nano Letters **20**, 5309–5314 (2020). DOI: 10.1021/acs.nanolett.0c01603

2.1 Introduction to optical bound states in the continuum

Bound states in the continuum represent a special group of optical resonances that do not have radiation losses and are completely decoupled from the continuum despite their resonant frequency is above the light line [78]. In this section we explain how they can be formed in periodic photonic structures. The periodic photonic structures represent open electromagnetic systems. They have more complicated description of the mode spectrum and mode interaction than the one used for closed systems. I.e., the eigenmode spectrum of closed systems consists of states with real frequencies and their interaction can be described in a framework of the total Hamiltionian $\hat{H}$ representing a sum of the Hamiltonian without interaction $\hat{H}_0$ and the interaction potential $\hat{V}$. The diagonal components of $\hat{V}$ are responsible for resonant frequency shift and the off-diagonal components are responsible for the internal mode coupling [137]. The interaction results in a mixing of eigenstates and appearance of avoided resonance crossings (ARCs) in the spectral response which is the characteristic feature of the strong coupling regime [138]. For open systems the modes are generally leaky and are interacting not only internally but also via the continuum of radiation waves.

Figure 2.2 shows schematic of mode interaction interpretation for open electromagnetic systems. The open system can be considered as a closed system with non-radiating modes $|A\rangle$

---

*Equal contributions

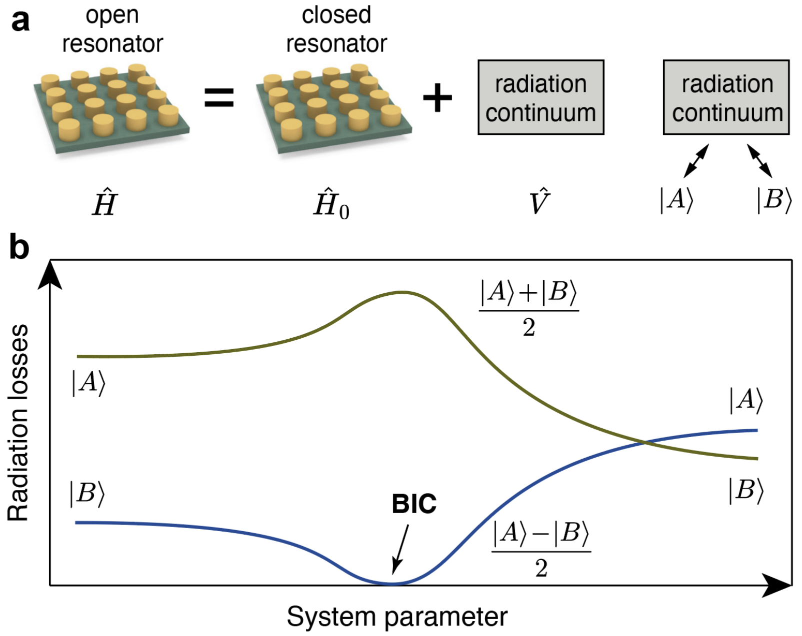

Figure 2.2: (a) Schematic description of an open resonator (dielectric metasurface) as a closed resonator interacting with the radiation continuum. (b) Change of radiation losses for interacting resonances $|A\rangle$ and $|B\rangle$ in the strong coupling regime. The mode marked with a blue line transforms into an accidental BIC with zero radiation losses via the change of the system parameters.

and $|B\rangle$ coupled to the continuum of the radiation modes outside of the resonator in accord with the Friedrich-Wintgen mechanism [139], see Fig 2.2a. While changing one of the system parameters, the modes can interact via the radiation continuum which leads to modification of their resonant frequencies and radiation losses [140]. More formally, Friedrich-Wintgen mechanism can be described in the framework of the temporal coupled mode theory. Approximating the system response with two resonant modes, we can describe it with a vector of complex amplitudes $\mathbf{a} = [a_A(t), a_B(t)]^T$ of states $|A\rangle$ and $|B\rangle$. The complex amplitudes evolve in time as:

$$\frac{d\mathbf{a}}{dt} = \hat{H}\mathbf{a}, \tag{2.1}$$

$$\hat{H} = \underbrace{\begin{pmatrix} \omega_A & \varkappa \\ \varkappa & \omega_B \end{pmatrix}}_{\hat{H}_0} - i \underbrace{\begin{pmatrix} \gamma_A & \sqrt{\gamma_A\gamma_B}e^{i\phi} \\ \sqrt{\gamma_A\gamma_B}e^{i\phi} & \gamma_B \end{pmatrix}}_{\hat{V}}. \tag{2.2}$$

Here, $\varkappa$ is responsible for the internal coupling, $\sqrt{\gamma_A\gamma_B}$ accounts for the coupling through the radiation continuum, and ϕ is the phase shift between the modes. The BIC forms when the radiative losses of one of the modes after interaction disappear. In the two-mode approximation this condition can be written as

$$\begin{aligned} &\kappa(\gamma_A - \gamma_B) = e^{i\phi}\sqrt{\gamma_A\gamma_B}(\omega_A - \omega_B) \\ &\phi = 0,\ \pi. \end{aligned} \tag{2.3}$$

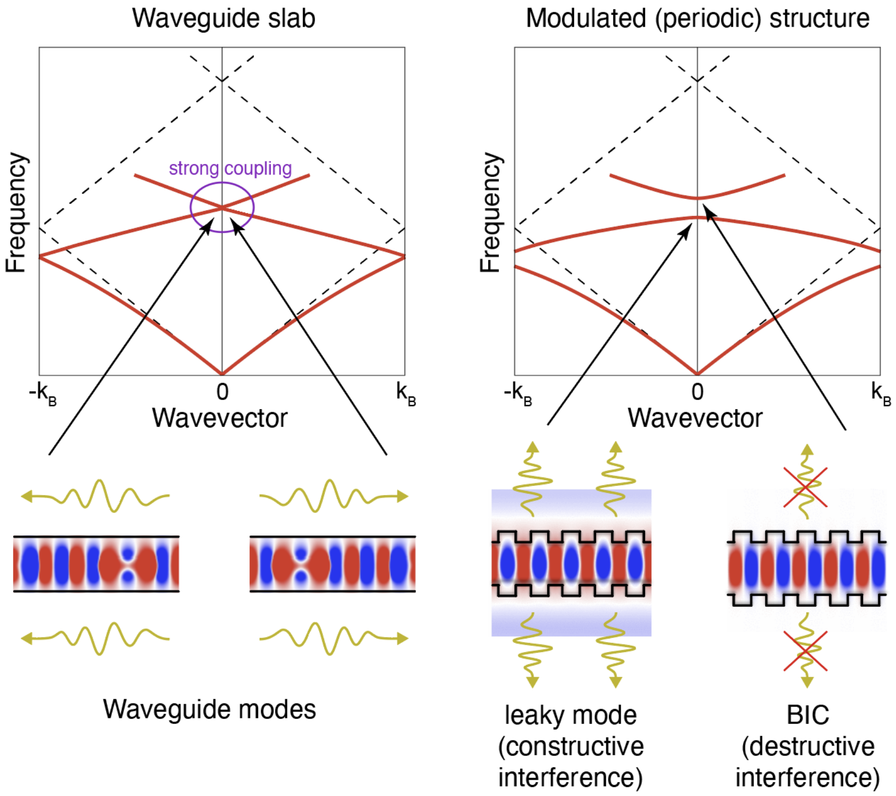

Figure 2.3: The mechanism of formation of symmetry-protected BICs in periodic photonic structures with in-plane inversion symmetry due to strong mode coupling at high symmetry points of the k-space.

This model can be used to engineer BICs in periodic photonic structures, including but not limited to gratings, photonic-crystal slabs or metasurfaces, for frequencies below the diffraction limit. The periodicity of the medium results in the coupling of guided modes to the continuum of radiation modes of the environment which induces leakage of the guided modes. Below the diffraction limit the modes are coupled to the zeroth-order diffraction channel so the two-mode approximation can be used.

There are two main approaches allowing to fulfill these conditions in periodic photonic structures. The first approach is to tune the parameters of two coupled resonances continuously, so the Eq. 2.3 is fulfilled at some specific set of system parameters. Figure 2.2b illustrates the characteristic change of radiation losses of two strongly coupled modes of an open resonator under continuous change of some system parameter, which defines the difference between resonant frequencies of non-interacting modes. The BICs that form due to accidental fulfillment of Eq. 2.3 are called *accidental BICs*, BICs due to parameter tuning. Usually, they can be achieved away from the high-symmetry points of the k-space [64].

The other way to realise BICs in periodic structures is related to the symmetry of the unit cell. The periodicity causes not only leaking of guided modes but also their backscattering which results in their strong coupling in high-symmetry points of the momentum space where their dispersion curves intersect. For structures with in-plane inversion symmetry, in the high-symmetry points of the wavevector space (e.g. Γ point for $k = 0$) the interacting

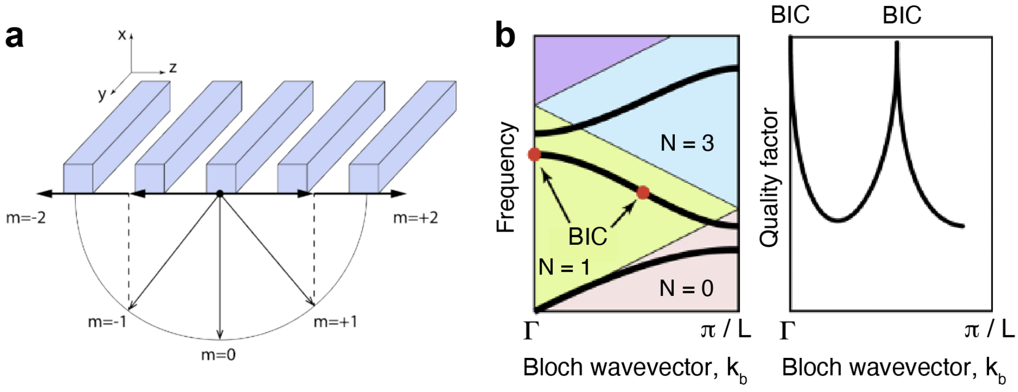

Figure 2.4: (a) Schematic of a dielectric grating with one-dimensional periodicity. The index m labels the diffraction channels. (b) Schematic of typical mode dispersion for the grating structure indicating the numbers of open diffraction channels N and positions of BICs (left); and variation the Q factor along the resonant mode branch with the BICs (right).

modes are degenerate $\omega_A = \omega_B$ and are coupled to the same radiation channel with equal strengths $\gamma_A = \gamma_B$. This, the mode coupling is precisely balanced at such high symmetry points, which allows constructing a symmetric leaky mode via constructive interference, and an antisymmetric bound mode which represents a so-called *symmetry-protected BIC*. The schematic of this interaction is shown in Fig. 2.3.

We explain the mechanism of formation of symmetry-protected and accidental BICs in more detail using the example of a dielectric grating with period L shown in Fig. 2.4(a). Using the Block theorem, the electric field can be written as

$$\mathbf{E}_{k_b}(x,y,z) = e^{ik_b z + ik_y y}\mathbf{u}_{k_b}(x,z). \tag{2.4}$$

Here, k_b is the Bloch k-vector, k_y is the k-vector component along the y-axis, $\mathbf{u}_{k_b}(x,z)$ is the periodic function of z. It can be expanded into the Fourier series

$$\mathbf{u}_{k_b}(x,z) = \sum_m \mathbf{c}_m(x) e^{ik_b z + \frac{2\pi}{L} imz}. \tag{2.5}$$

Here, $m = 0, \pm1, \pm2, \ldots$ Each term in this series corresponds to one diffraction channel. Outside the structure, the expansion coefficients correspond to plane waves

$$\mathbf{c}_m(x) \longrightarrow \mathbf{c}_m e^{\pm iK_m x}, \tag{2.6}$$

$$K_m = \sqrt{\frac{\omega^2}{c^2} - k_y^2 - \left(k_b^2 + \frac{2\pi m}{L}\right)^2}. \tag{2.7}$$

If K_m is real, then the diffraction channel is open and $\mathbf{c}_m$ represents the complex amplitude of the outgoing wave coupled to the m-th diffraction channel. If K_m is imaginary, then the diffraction channel is closed and $\mathbf{c}_m$ is the complex amplitude of the near-field.

To construct a BIC, all coefficients $\mathbf{c}_m$ corresponding to the open diffraction channels should be nullified. However, for a subwavelength structure $L < \lambda$, there is only one open diffraction channel corresponding to $m = 0$. Thus, to construct a BIC we need to nullify $\mathbf{c}_0(x)$. The function $\mathbf{c}_0(x)$ is given by

$$\mathbf{c}_0(x) = \int_{-L/2}^{L/2} \mathbf{u}_{k_b}(x,z) e^{-ik_b z} dz. \tag{2.8}$$

At the origin of the k-space ($k_b = 0$) we have

$$\mathbf{c}_0(x) = \int_{-L/2}^{L/2} \mathbf{u}_{k_b}(x,z) dz = \langle \mathbf{u}_{k_b}(x,z) \rangle_z. \tag{2.9}$$

Thus, the condition of a BIC at the Γ-point requires zero of the z-averaged electric field components. If the unit cell of the grating is symmetric with respect to the in-plane inversion transformation, then the modes at the Γ-point are classified as even or odd functions of z. For odd functions, their z-averaged value is zero and the state represents a symmetry-protected BIC. If $\mathbf{c}_0(x)$ becomes zero via tuning of system parameters, the BIC is accidental, as discussed above.

Figure 2.4(b) shows schematically the characteristic dispersion (ω vs k_b for $k_y = 0$) and mode Q factor of eigenmodes in a dielectric grating with one-dimensional periodicity. The colored areas show the regions, where a certain number of diffraction channels (N) is open. Below the light line $\omega = ck_z$, there is no open channels $N = 0$. Above the light line, but below the diffraction limit $N = 1$ so the Friedrich-Wintgen model can be applied. At the origin of the k-space, the structure posses the in-plane inversion symmetry and the symmetry-protected BIC is formed. Away from the origin, the structure supports an accidental BIC located at the same dispersion branch [92]. The presented dispersion structure is general and can be achieved for various periodic photonic structures, including dielectric metasurfaces.

2.2 Bound states in the continuum in lossless asymmetric metasurfaces.

We analyse the properties of resonant light scattering for a general class of asymmetric metasurfaces with an example shown in Fig. 2.5a. The unit cell of the metasurface can be different, for example, it can consist of two rotated elliptical bars [109, 110], a disk with an asymmetric hole [121], two parallel bars of different length [124, 128], a bar with a pitch [126, 127], split-ring resonators [122, 123, 129, 130], shown in Fig. 2.5b. We focus on one of the examples recently suggested for biosensing [109], a square array of meta-molecules composed of tilted elliptical bars made of Si, and analyze how symmetry-protected BICs emerge in such kind of structures and how they produce sharp resonances in scattering spectrum.

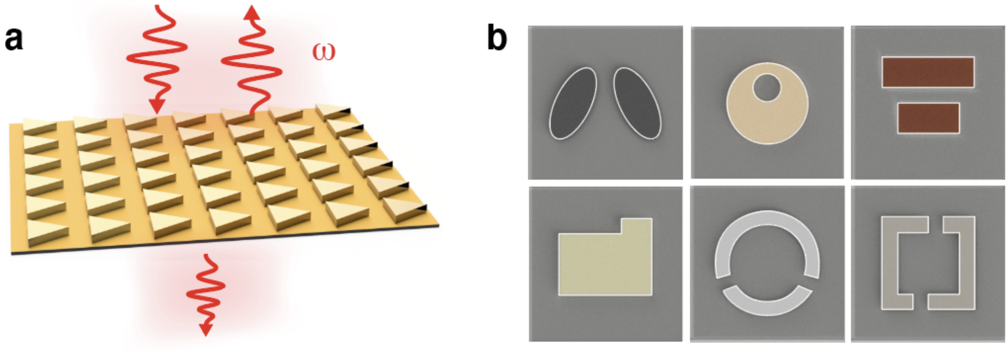

Figure 2.5: (a) Schematic of light scattering from a metasurface. (b) Examples of the meta-atom design of broken-symmetry metasurfaces supporting sharp resonances, discussed in Refs. [109, 121–124, 126–130].

2.2.1 Spectral properties of BICs

In this section we consider an idealized case of lossless silicon metasurface of infinite size, so the resonant losses are purely radiative. For the sake of simplicity, we consider a free-standing metasurface suspended in a homogeneous background with permittivity 1, however, the results can be generalized for a metasurface on a dielectric substrate, shown in Fig. 2.6a. The asymmetry is controlled by the angle θ between bar longest axis and the in-plane y-axis of the lattice, as shown in the inset of Fig. 2.6a. For $\theta = 0^{\circ}$ the structure possesses in-plane inversion symmetry and supports a series of symmetry-protected BICs with at the normal incidence. The radiative Q factor of BICs is infinite, so it cannot be accessed from the far-field. This means that the in-plane symmetry needs to be disturbed in order to observe any resonant features in scattering. The conventional way to break this symmetry is to tilt the incident beam making the incidence oblique, thus the symmetry of the structure with respect to the pump direction is disrupted. For oblique excitation, the BICs are transformed into quasi-BICs with a finite Q factor which decreases with the increase of angle of incidence [64]. In our analysis we aim to keep the normal incidence geometry, therefore, we consider breaking the in-plane symmetry of the metasurface unit cell $(x, y) \to (-x, -y)$ by making $\theta > 0$. Similarly to the case of oblique incidence, we expect that symmetry-protected BICs are converted into high-Q quasi-BIC with the linewidth depending on the asymmetry of the unit cell. We perform the calculation of transmission spectra and eigenmode spectra for different asymmetries for the fixed refractive index of material equal to 3.47 which is a typical value for bulk crystalline Si in the near-IR [141]. The simulation procedure is described in Appendix A.1. For our analysis we put the period equal to 1320 nm, bar semiaxes are 330 nm and 110 nm, thickness is 200 nm, distance between bars is 660 nm. The electric field of the pump wave is directed along the x-axis, as shown in Fig. 2.6a. We focus on a symmetry-protected BIC existing for $\theta = 0^{\circ}$ at the wavelength of about 1570 nm. Dependence of the eigenmode and transmission spectra on θ is shown in Fig. 2.6b, where T is the transmittance. We observe that BIC with infinite Q factor at $\theta = 0^{\circ}$ transforms into high-Q quasi-BIC with radiation loss growing with increase of θ. The asymmetry parameter α can be defined as $\alpha = \sin\theta$. The detailed transmission spec-

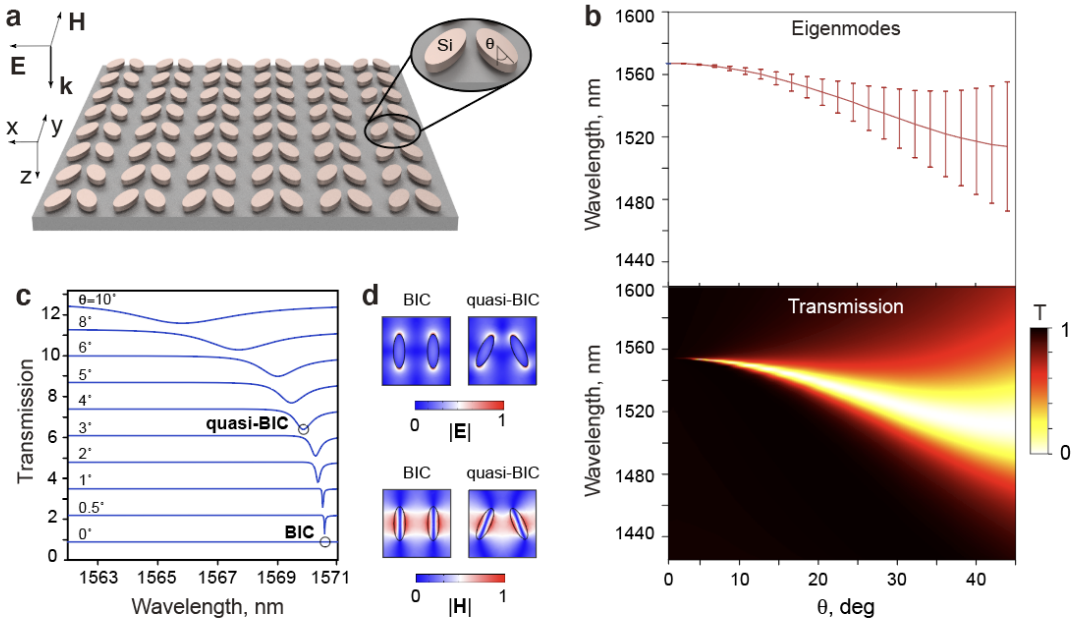

Figure 2.6: (a) Design of the broken-symmetry metasurface: square array of tilted bar meta-molecules. The inset shows the design of the unit cell. (b) Eigenmode and transmission spectra vs. pump wavelength and tilting angle θ. Error bars show the magnitude of the mode inverse radiation lifetime. (c) Evolution of the transmission spectra vs angle θ. Spectra are relatively shifted by 1.5 units. (d) Distribution of the electric and magnetic fields for both BIC and quasi-BIC.

tra shown in Fig. 2.6c exhibit a narrow dip that vanishes when the meta-molecule becomes symmetric, which confirms the results of the eigenmode analysis. Figure 2.6d demonstrates that the BIC mode consists of two electric dipoles, one in each meta-atom, oriented in opposite directions. The field profiles show similarity for the BIC and quasi-BIC modes. For comparison, we investigate quasi-BICs and their response spectrum for a metallic metasurface composed of a square array of aluminium asymmetric split rings of square shape. The metasurface unit cell and its parameters are shown in Fig. 2.7a. For calculations we use finite-element-method built in the CST simulation software. The asymmetry parameter α is defined as $\alpha = \Delta L/L$, where L is the width of the square. One can see in Fig. 2.7c that the reflectance spectrum for $\alpha = 0$ in THz range does not show any resonant features, while a pronounced dip appears at 1.3 THz for $\alpha = 0.33$. The dip is a manifestation of a quasi-BIC in the plasmonic metasurface, mode current distribution is shown in Fig. 2.7b. Another example of a broken-symmetry dielectric metasurface is shown in Fig. 2.8a. The metasurface us composed of bar pairs with permittivity of 13.5 of equal width but different length arranged in the rectangular lattice.The asymmetry parameter α is defined as $\alpha = \Delta L/L$, where L is the length of the longest bar and ΔL is the difference in bar lengths. The reflectance spectrum in Fig. 2.8d shows a sharp quasi-BIC resonance for nonzero asymmetry parameter $\alpha = 0.1$. The eigenmode spectrum and reflectance map shown in Fig. 2.8c demonstrate evolution of quasi-BIC with respect to the asymmetry parameter.

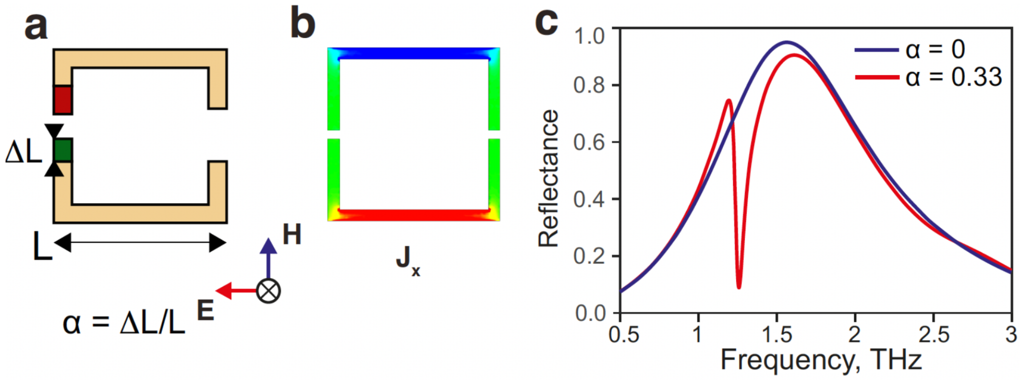

Figure 2.7: (a) Design of the unit cell of a metasurface composed of a square lattice of aluminum square split rings suspended in free-space. Parameters: the period is 75 μm, the large square side is 60 μm, the ring thickness is 4 μm, the height is 0.2 μm, distance between semirings is 3 μm, the aluminium conductance is 3.56×10^7 S/m. (b) Current distribution at the quasi-BIC resonance. (c) Evolution of the reflectance vs. α.

2.2.2 Radiation losses. Multipolar decomposition.

Dielectric metasurfaces represent open electromagnetic resonators and quasi-BIC modes are a part of spectrum of metasurface resonant states (RSs) with complex eigenfrequencies, see Appendix A.3.1. Radiation losses of quasi-BICs can be found as the ratio between the outgoing energy flux and the energy inside the metasurface, see Appendix A.3.3. The outgoing energy flux depends on the field expressions at the structure surface that can be found using expansion over the outgoing radiation modes of the free-space evaluated at the complex eigenfrequency of the quasi-BIC $\Omega_0 = \omega_0 - i\gamma_0$, see Appendix A.2 and A.3.2. In the sub-diffractive limit, we can express the rate of radiative losses of energy $2\gamma_0$ via the coupling coefficient between the quasi-BIC and the outgoing modes of radiation continuum, see Appendix A.3.3. Assuming the radiative Q factor of the quasi-BIC more than 10, we can neglect contribution from high-order diffraction modes to radiation, which are generally leaky because of nonzero imaginary part of the quasi-BIC eigenfrequency

$$\frac{2\gamma_0}{c} = \frac{\sum_{\tilde{N}} \left|\kappa_{\tilde{N}}\right|^2}{W_0}, \tag{2.10}$$

$$\kappa_{0N} = -i \oint_{S_V} d\mathbf{S} \cdot \left(\mathbf{E}_0 \times \mathbf{H}^{\mathrm{i}}_N(k_0) - \mathbf{E}^{\mathrm{i}}_N(k_0) \times \mathbf{H}_0\right), \tag{2.11}$$

$$W_0 = \int\limits_V dV \left(\varepsilon\, |\mathbf{E}_0|^2 + |\mathbf{H}_0|^2\right). \tag{2.12}$$

Here, $k_0 = \Omega_0/c$ is the complex k-vector of quasi-BIC, $\mathbf{E}_0$ and $\mathbf{H}_0$ is the electric and magnetic field of the quasi-BIC, respectively, W_0 is the normalized mode energy inside the resonator, and the summation goes over $\tilde{N}$ which includes the waves normal to the surface plane radiating from the top and bottom, with two possible polarizations, s and p. The integration goes over the volume of one unit cell. The electric and magnetic field of the incoming mode of the radiation continuum $\mathbf{E}^{\mathrm{i}}_{\tilde{N}}$ and $\mathbf{H}^{\mathrm{i}}_{\tilde{N}}$ is given by expressions in Appendix A.2. The coupling

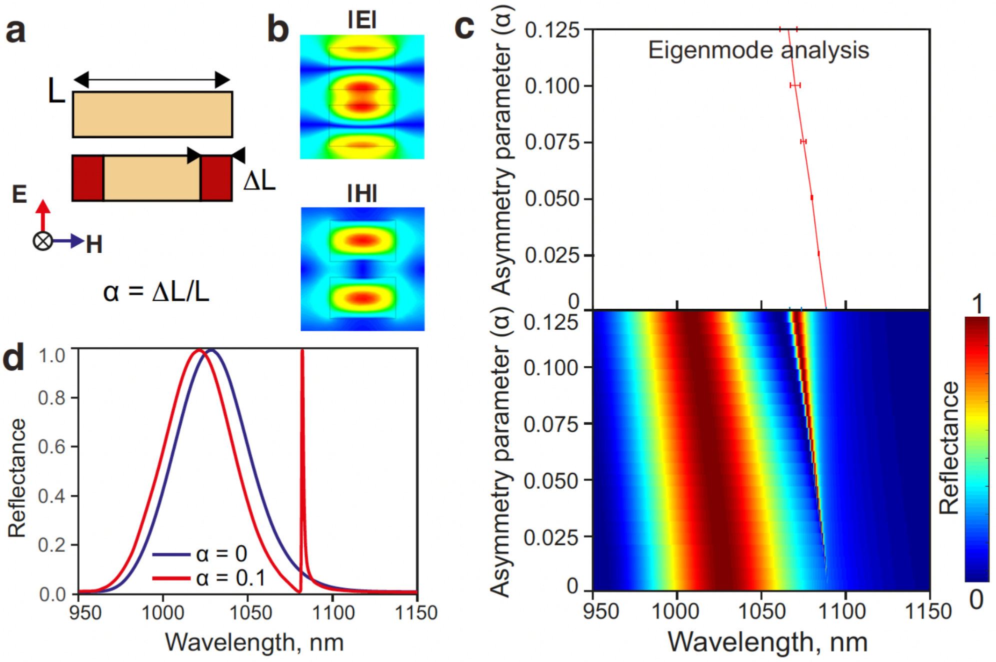

Figure 2.8: (a) Design of the unit cell of a dielectric metasurface composed of bar pairs with permittivity of 13.5 of equal width but different length arranged in the rectangular lattice. Parameters: the metasurface is suspended in free-space, the period in x direction is 725 nm, the period in y direction is 530 nm, large bar size is 200×280 (nm×nm), the height is 250 nm, distance between bars is 75 nm. (b) Distribution of the electric and magnetic fields at the BIC wavelength. (c) Eigenmode spectra and reflectance with respect to the pump wavelength and asymmetry parameter α. Error bars show the magnitude of the mode inverse radiation lifetime. (d) Evolution of the reflectance vs. α.

amplitude can be expressed through the volume integral

$$\kappa_{0N} = -k_0 \int_V dV\,(\varepsilon(\mathbf{r})-1)\mathbf{E}_0 \cdot \mathbf{E}^{\mathrm{i}}_N(k_0), \tag{2.13}$$

where $\varepsilon(\mathbf{r})$ is the permittivity function of the metasurface.

For a free-standing structure with up-down mirror symmetry of the unit cell the modulus of coupling coefficients from top and bottom is equal, so we can double the contribution of the waves incoming from the top. In the sub-diffractive regime the only radiation channels are p- and s-polarized waves propagating normal to the surface plane. Thus, we get

$$\frac{\gamma_0}{c} = \frac{|\kappa_{0,s}|^2 + |\kappa_{0,p}|^2}{W_0}, \tag{2.14}$$

$$\kappa_{0,(s,p)} = g_0 \int_{V_{\mathrm{t}}} dV\ (\varepsilon(\mathbf{r})-1)\mathbf{E}_0 \cdot \hat{\mathbf{e}}_{s,p} e^{ik_0 z}, \tag{2.15}$$

$$g_0 = -e^{i\pi/4} \frac{k_0}{\sqrt{2S_{\mathrm{u}}}}. \tag{2.16}$$

Here, $\hat{\mathbf{e}}_{s,p}$ is the unitary polarization vector of the radiation mode, S_{u} is the area of the unit cell, and V_{t} is the volume of the top part of the meta-atom with $z < 0$.

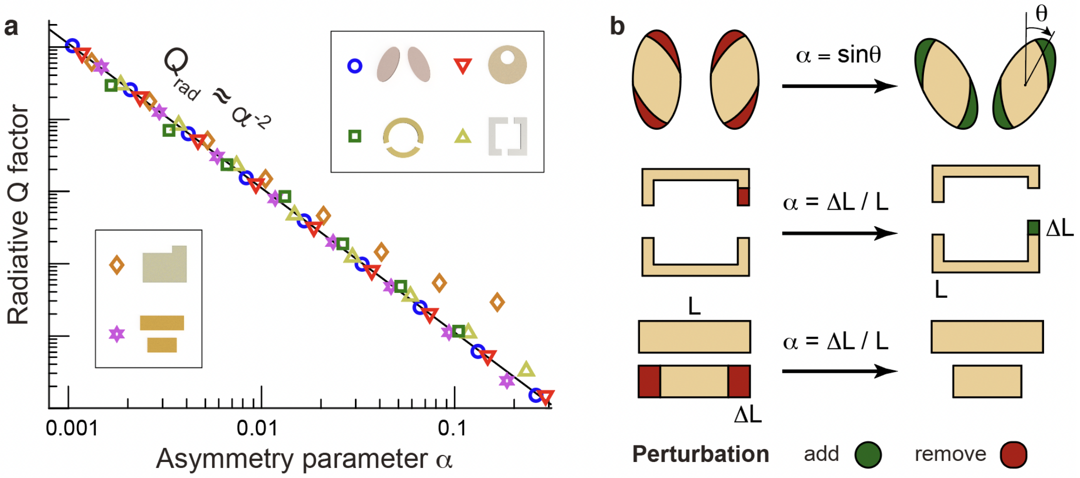

Figure 2.9: (a) Dependence of the Q factor on the asymmetry parameter α for the metasurfaces with meta-atoms shown in Fig. 2.5b (log-log scale). (b) Definition of α for the metasurfaces considered in Figs. 2.6, 2.7 and 2.8.

The function e^{ik_0z} in the integrand can be expanded into the Taylor series since $|k_0z| \ll 1$. The coupling amplitudes $\kappa_{0,(s,p)}$ can be decomposed as

$$\kappa_{0,s} = g_0\left[p_y + \frac{m_x}{c} + \frac{ik_0}{6}Q_{yz} + \ldots\right], \tag{2.17a}$$

$$\kappa_{0,p} = g_0\left[p_x - \frac{m_y}{c} + \frac{ik_0}{6}Q_{zx} + \ldots\right], \tag{2.17b}$$

where $\mathbf{p}$, $\mathbf{m}$ and $\hat{\mathbf{Q}}$ are the Cartesian electric dipole, magnetic dipole and electric quadrupole moments in the long-wavelength approximation expressed in the irreducible representation [142]. Here, we define the multipoles using the vector $(\varepsilon-1)\mathbf{E}_0$ proportional to the polarization and omit $1/4\pi$ factor, e.g. $p_x = \int_{V_t} dV\ (\varepsilon-1)E_{0,x}$. We also note, that the volume integration for multipoles is done only in the top subspace V_t with $z<0$.

Equation 2.16 shows that for a BIC the unit cell inversion symmetry imposes vanishing $\kappa_{0,(s,p)}$ and radiation losses [94]. Small asymmetry of the unit cell (asymmetry parameter $\alpha > 0$) leads to nonzero radiation losses and finite radiative Q factor $Q_{\rm rad} = \omega/2\gamma_0$. Using the perturbation theory for non-Hermitian systems, we can estimate the behavior of $Q_{\rm rad}$ with respect to the asymmetry. In Eq. 2.16 we leave the zero order component of $\mathbf{E}_0$ as for a true BIC because the next order field component depends on the perturbation quadratically. Thus, the integral over total volume of asymmetric structure is a sum of integrals over symmetric unit cell, which vanishes for a BIC, and over the perturbation region, which gives the linear dependence of $\kappa_{0,(s,p)}$ on α. Thus, for small asymmetries

$$Q_{\rm rad} = \tilde{Q}\alpha^{-2}. \tag{2.18}$$

where $\tilde{Q}$ is determined by the metasurface design and is independent on α. We note that Eq. (2.18) is applicable for describing quasi-BICs in metasurfaces on a substrate if the mode frequency is below the diffraction limit of the substrate [105].

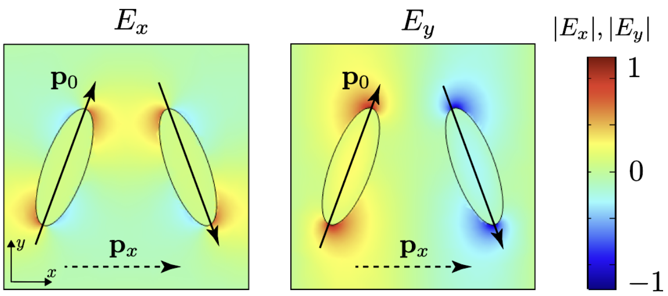

Figure 2.10: Electric field in-plane components for the quasi-BIC analysed in Fig. 2.6. Arrows show the dipole moments of each bar $\mathbf{p}_0$ and the net dipole moment $\mathbf{p}_x$.

Next, we demonstrate numerically that the quadratic dependence on α defined by Eq. (2.18) is a universal law for Q_{rad} of quasi-BICs for various metasurfaces with broken-symmetry meta-atoms. Figure 2.9a shows a direct comparison of the values of Q_{rad} for dielectric and plasmonic metasurfaces shown in the inset (see also Fig. 2.5b). All curves are shifted relatively in the vertical direction to originate from the same point. For metallic metasurfaces possessing absorption losses, Q_{rad} is extracted from the total Q factor and the non-radiative damping rate evaluated at $\alpha = 0$. We use the dimensionless asymmetry parameter α, which has distinct definitions for different structures and takes values between 0 and 1, some examples are shown in Fig. 2.9(b). The simulations in Fig. 2.9(a) show that evolution of Q_{rad} for small α is clearly inverse quadratic. Importantly, for most of the structures the law $Q_{\text{rad}} \propto \alpha^{-2}$ is valid beyond the applicability limits of the perturbation theory. To explain this, we analyse the quasi-BIC field components for the tilted Si bar pairs design, as shown in Fig. 2.10. The mode field has a dipole moment $\mathbf{p}_0$ within each bar and the y-components of $\mathbf{p}_0$ for the bars are opposite. The net dipole moment p_x is

$$p_x = 2p_0 \sin\theta, \tag{2.19a}$$

$$p_0 = \int\limits_{\text{one bar}} dV\,(\varepsilon - 1)E_{0,y}(\theta = 0°, \mathbf{r}). \tag{2.19b}$$

Then, Q_{rad} can be found as

$$Q_{\text{rad}} = \tilde{Q}\,(\sin\theta)^{-2}, \tag{2.20a}$$

$$\tilde{Q} = W_0 \frac{S_{\text{u}}}{4|k_0|}|p_0|^{-2}. \tag{2.20b}$$

Here, the asymmetry parameter is defined in more general way as $\alpha = \sin\theta$ so the inverse quadratic law in Eq. 2.20a is valid not only for small θ.

2.2.3 Generalized Fano formula for transmittance

To explain the connection between the scattered spectra and the eigenmode spectra in Figs. 2.6c, 2.7c and 2.8c, we derive analytical expressions for the transmittance via partial contributions of RSs (quasi-normal modes) [143] and their interference in the far-field. The RSs are the self-standing electromagnetic excitations characterized by a discrete set of complex resonant frequencies $\Omega_n = \omega_n - i\gamma_n$, where γ_n is a half of inverse mode radiative lifetime. The spectrum of RSs of the metasurface also includes the contribution from the Rayleigh anomalies, representing a continuous distribution of modes in the cuts of ω-plane [144]. We introduce the complex wavevector for RSs as $k_n = \Omega_n/c$ and wavevector of free space as $k = \omega/c$ (for more details see Appendix A.3.1).

The scattering matrix of the metasurface operating in the sub-diffraction limit and for fixed incident polarization is a 2×2 matrix . We consider a p-polarized incident plane wave propagating from top to bottom as shown in Fig. 2.6a. The S-matrix can be decomposed into contributions of RSs via pole expansion (see Appendix A.3.4)

$$\hat{S}_{p,p} = \begin{bmatrix} \rho & \tau \\ \tau & \rho \end{bmatrix} + \sum_n \frac{1}{N_n(k-k_n)} \begin{bmatrix} \left(\kappa^{\mathrm{t}}_{n,p}\right)^2 & \kappa^{\mathrm{t}}_{n,p}\kappa^{\mathrm{b}}_{n,p} \\ \kappa^{\mathrm{t}}_{n,p}\kappa^{\mathrm{b}}_{n,p} & \left(\kappa^{\mathrm{b}}_{n,p}\right)^2 \end{bmatrix}. \tag{2.21}$$

Here, ρ and τ are reflection and transmission coefficients of the non-resonant background. The coefficient N_n is the RSs normalization constant, and the coefficients $\kappa^{\mathrm{t,b}}_{n,p}$ are the frequency independent coupling constants between the n-th RS and the incoming p-polarized plane wave from top and bottom side, respectively. The coupling coefficients can be evaluated as the residues of S-matrix at the resonant frequencies k_n [see Eq.(A.29) in Appendix A.3.4]

$$\kappa^{\mathrm{t,b}}_{n,p} = -e^{i\pi/4}\frac{k_n}{\sqrt{2S_{\mathrm{u}}}}\int_{V_{\mathrm{t}}} dV\ (\varepsilon-1)\mathbf{E}_n\cdot\hat{\mathbf{e}}_{\mathrm{p}}e^{\pm ik_n z}. \tag{2.22}$$

Here, the integration is within a top (bottom) half of one unit cell, S_{u} is the area of the unit cell, and $\hat{\mathbf{e}}_{\mathrm{p}}$ is the unitary vector of p-polarized excitation directed along x-axis. One can see that the coupling constants are the same as outcoupling coefficients in Eq. 2.16, which is due to reciprocity theorem. The metasurface possesses up-down reflection symmetry $z \to -z$, thus the coupling constants at the top and bottom surfaces are transformed as

$$\kappa^{\mathrm{b}}_{n,p} = (-1)^{p_n}\kappa^{\mathrm{t}}_{n,p}, \tag{2.23}$$

where $p_n = 0,1$ is the mode parity with respect to the up-down reflection symmetry.

Using Eqs. 2.10 and 2.23 the coefficient $\kappa^{\mathrm{t}}_{n,p}$ can be expressed via the radiative linewidth of the mode

$$\kappa^{\mathrm{t}}_{n,p} = \sqrt{\frac{\gamma_n}{c}W_n}e^{i\varphi^n_\kappa}, \tag{2.24}$$

where φ^n_κ is the coupling phase.

The transmission amplitude t is the non-diagonal element of the S-matrix from Eq. (2.21)

$$t(\omega) = \tau(\omega) + \sum_n \frac{(-1)^{p_n}\left(\kappa^{\mathrm{t}}_{n,p}\right)^2}{N_n(k-k_n)}. \tag{2.25}$$

We study the transmission coefficient in the vicinity of one of the RSs with $n = 0$. In case neighboring resonances do not overlap with the resonant state of interest, the frequency dependence of non-resonant terms is slow in the range from $\omega_0 - \gamma_0$ to $\omega_0 + \gamma_0$. By straightforward but quite cumbersome rearrangements of terms of the transmittance $T = |t|^2$ can be written as a generalized Fano formula

$$T(\omega) = \frac{T_\mathrm{A}}{1+q^2}\frac{(q+\Delta\omega)^2}{1+\Delta\omega^2} + T_\mathrm{nr}. \tag{2.26}$$

Here, q is the Fano asymmetry parameter, T_A is the amplitude of the smooth envelope and T_nr is the contribution from background and non-resonant modes. The analytical expressions for Fano parameters can be found in Appendix A.5.1. The frequency dependence of q, T_A and T_nr for $\omega \simeq \omega_0$ is smooth, and can be neglected. For a true BIC $\Delta\omega \to \infty$, which corresponds to a collapse of the Fano resonance when any features in the transmission spectra disappear, and the resonant mode is transformed into a dark mode.

The description of the scattered signal with the Fano formula is widely used by introducing the asymmetry parameter phenomenologically [81]. Our pole expansion approach for the scattering matrix is an alternative way to describe scattering with the Fano formula, compared to other approaches, e.g. using Feshbach–Fano partitioning scheme [145]. We note that using Eq. (2.21) the reflectance can be also written in the form of the generalized Fano formula.

2.3 Effect of losses. Optimal coupling regime

For lossless metasurfaces of infinite size in the sub-diffractive limit the Q factor of BICs Q_rad is determined solely by radiation normal to the surface plane. In practise, losses limit the total Q factor Q_tot, so it can be decomposed into partial contributions:

$$Q_\mathrm{tot}^{-1} = \underbrace{Q_\mathrm{rad}^{-1} + Q_\mathrm{par}^{-1}}_{\text{radiative}} + \underbrace{Q_\mathrm{abs}^{-1}}_{\text{non-radiative}}, \tag{2.27}$$

$$Q_\mathrm{par}^{-1} = Q_\mathrm{surf}^{-1} + Q_\mathrm{dis}^{-1} + Q_\mathrm{size}^{-1} + Q_\mathrm{sub}^{-1}. \tag{2.28}$$

Strictly speaking, Eqs. 2.27 and 2.28 are valid in case one of the loss mechanisms is strong compared to the others. Equation 2.27 shows that in addition to out-of-plane radiation Q_rad the radiative losses are also contributed by other mechanisms which we call parasitic losses with the Q factor Q_par. They include surface scattering from imperfections (Q_surf), structural disorder (Q_dis), diffraction losses and losses from the sample edges due to finite size of the sample (Q_size), and diffraction into high-index substrate (Q_sub). Moreover, the total Q factor is contributed by non-radiative losses (Q_abs) due to material absorption. From Eq. 2.27 one can see that true BICs can exist for nonzero absorption losses for $Q_\mathrm{rad}^{-1} = Q_\mathrm{par}^{-1} = 0$.

The loss mechanisms for BICs in metasurfaces are shown schematically in Fig. 2.12a. For high-index dielectric materials, such as silicon or gallium arsenide, the non-radiative losses

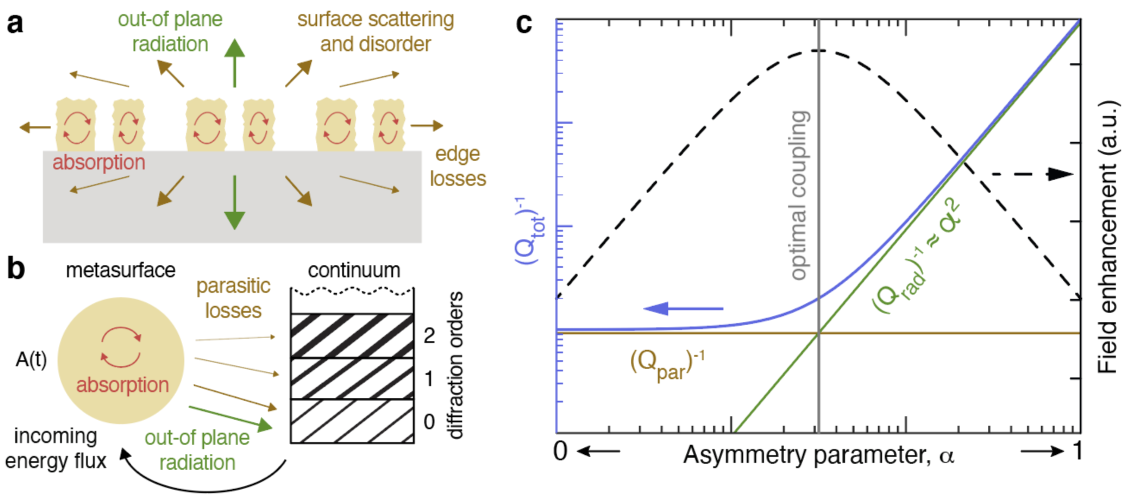

Figure 2.11: (a) Schematic representation of out-of-plane radiation (green) and parasitic losses (brown) of quasi-BICs for a realistic metasurface of finite size with fabrication imperfections and material losses. (b) Schematic of the evolution of the resonant amplitude of the quasi-BIC $A(t)$ coupled to the radiation continuum via radiation to the zeroth diffraction order (green) and scattering to all diffraction orders due to parasitic losses (brown). (c) Dependence of the inverse total Q factor (solid blue) and field enhancement (dashed black) on the asymmetry parameter. The optimal coupling regime is shown with a gray solid line.

are very low ($Q_{\text{abs}} > 10^5$) in the IR and most part of the visible range. The parasitic losses lead to transformation of BICs into quasi-BICs with a finite radiative Q factor. Recently it was shown that Q_{sub} can be increased by making a low-index spacer of specific thickness between the structure and the substrate [105]. For symmetry-protected BICs in finite size structures it was demonstrated that Q_{size} grows with increase of the number of periods N as $Q_{\text{size}} \propto N^2$ [146]. Very recently it was predicted that structural disorder with amplitude σ contributes to Q factor as $Q_{\text{dis}} \propto \sigma^{-2}$ [147]. A few experimental studies considered effects of deviations in meta-atom sizes due to fabrication tolerances on Q_{surf} [105, 148].

To analyse how the interplay of different mechanisms of losses affects the resonant field enhancement for quasi-BICs we apply the temporal coupled-mode theory [149]. Hereinafter, we consider dielectric metasurfaces and neglect the non-radiative losses. We derive the temporal coupled-mode theory from Maxwell's equations using the expansion of the Green's function into resonant states. In the single-mode approximation the resonant amplitude $a(t)$ changes in time due to self-oscillations and pump excitation as shown schematically in Fig. 2.12b

$$\frac{da(t)}{dt} = -i\omega_0 a(t) - \frac{\omega_0}{2}\left(Q_{\text{rad}}^{-1} + Q_{\text{par}}^{-1}\right) a(t) + \kappa_0 E_{\text{inc}}. \tag{2.29}$$

Here, ω_0 is the real part of the quasi-BIC frequency, E_{inc} is the amplitude of the pump electric field, and κ_0 is proportional to the amplitude of coupling between the pump and the quasi-BIC (see Eq. 2.22). The parasitic loss mechanisms couples the mode to higher-order diffraction channels as shown in Fig. 2.12b. Due to the reciprocity theorem we get $\kappa_0 \propto Q_{\text{rad}}^{-1/2}$ (see Eq. 2.24). Importantly, we neglect the contribution of parasitic losses to the zeroth diffraction order. The local field can be expressed via the mode volume V_0 and resonant amplitude as $E_{\text{loc}} \propto a(\omega_0)V_0^{-1/2}$ [150, 151]. The closed-form expressions for κ_0 and V_0 is given in Appendix A.4. The local field enhancement $|u|^2$ at the resonant frequency $\omega = \omega_0$ can be expressed as (for derivation see Appendix A.4)

$$|u|^2 = \frac{|E_{\text{loc}}|^2}{|E_{\text{inc}}|^2} = \frac{\lambda S_{\text{u}}}{\pi} \frac{Q_{\text{tot}}}{V_0} \frac{Q_{\text{tot}}}{Q_{\text{rad}}}. \tag{2.30}$$

Here, S_{u} is the unit cell area, λ is the resonant wavelength. We note that this expression differs from the local field enhancement in Ref. [152] by the factor of 2 because here we account for the losses to the up and down radiation channels and the effective aperture of the metasurface as an antenna is $S_{\text{u}}/2$ (see. Eq. A.51.

For quasi-BICs the radiative Q factor Q_{rad} is highly sensitive to the meta-atom asymmetry, see Eq. 2.18, while the parasitic losses and mode volume depend on α weakly. Analysis of Eq. (2.30) with respect to variation of α shows that the field enhancement is maximized when

$$Q_{\text{rad}} = Q_{\text{par}}, \tag{2.31}$$

which coincides with the so-called optimal (or, critical) coupling condition [152]. The total Q factor can be expressed via asymmetry as

$$Q_{\text{tot}}(\alpha) = \frac{Q_{\text{par}}}{\alpha^2/\alpha_{\text{opt}}^2 + 1}. \tag{2.32}$$

Here, α_{opt} is the optimal asymmetry parameter

$$\alpha_{\text{opt}} = \left(\frac{\tilde{Q}}{Q_{\text{par}}}\right)^{1/2}, \tag{2.33}$$

and $\tilde{Q}$ is defined in Eq. 2.18. The field enhancement can be rewritten in a similar manner

$$|u|^2 = \frac{\lambda S_{\text{u}}}{\pi} \frac{Q_{\text{par}}}{V_0} \frac{\alpha^2/\alpha_{\text{opt}}^2}{\left(\alpha^2/\alpha_{\text{opt}}^2 + 1\right)^2}. \tag{2.34}$$

The typical dependence of the inverse total Q factor and the field enhancement on the asymmetry given by Eqs. 2.32 and 2.34 is shown in Fig. 2.11. We note that at the optimal coupling regime the field enhancement scales as Q_{par}/V_0.

We emphasize that the parasitic losses play a significant role in maximization of the field enhancement which determines the efficiency of many nonlinear processes. We note that our results generalize the results obtained for resonant antennas with non-radiative losses earlier [152].

2.4 Designing a high-Q metasurface on demand

In this section we provide a general framework how to design a high-Q dielectric metasurface providing maximal local field enhancement at the wavelength of interest. The metasurface engineering and optimization procedure can be outlined in the following steps

1. select a metasurface design with in-plane inversion symmetry of the unit cell;
2. search for a low frequency BIC in the spectrum;
3. apply geometrical scaling to adjust the resonant wavelength of BIC to the target wavelength;
4. determine the magnitude of parasitic Q_{par} Q factor experimentally or from the literature;
5. tune the quasi-BIC to the optimal coupling regime $Q_{\mathrm{rad}} = Q_{\mathrm{par}}$ by increasing the asymmetry;
6. adjust the scaling factor to compensate the wavelength shift due to nonzero asymmetry.

As an example, we target the 1550 nm wavelength and consider a Si metasurface composed of a square array of parallel bar pairs with equal length L but slightly different width w_1 and w_2 shown in Fig. 2.12a. First, we consider a structure with symmetric unit cell $w_1 = w_2$, it supports a BIC at 1550 nm for $w_1 = 230$ nm, $p = 720$ nm, $L = 590$ nm, $d = 300$ nm, and $h = 500$ nm. For many common dielectric materials, such as silicon, dispersion of dielectric function is weak so we can apply geometric scaling to adjust the wavelength. We introduce the scaling factor S as a multiplier to change all geometrical parameters simultaneously, as shown in Fig. 2.12a. Figure 2.12b shows the evolution of BIC wavelength in the approximation of refractive index fixed at 1550 nm (solid black) and for realistic dispersion of Si (dashed blue) depending on the scaling factor. The simulation procedure is described in Appendix A.1. One can see that the deviation of the analytical model from the simulated data is less than 20% in the visible and less than 5% in the mid-IR ranges. From Fig. 2.12b follows that the target design can be achieved for the scaling factor $S \simeq 1$.

The second step is to introduce asymmetry and tune the structure into the optimal coupling regime. For this we need to determine the parasitic Q factor Q_{par}. The typical value for Si metasurfaces is of order of a few hundred [109] and depends on the particular design [148]. With better fabrication facilities it is possible to obtain Q_{par} of order of a few thousand [153, 154] and even tens of thousand [155]. In this section we use the intermediate value of $Q_{\mathrm{par}} = 2000$. The asymmetry parameter is proportional to the difference between the bar widths $\alpha = 1 - w_1/w_2$, as shown in Fig. 2.12c, upper panel. For $\alpha > 0$ the BIC transforms into a quasi-BIC which radiation is determined by the uncompensated net magnetic dipole (MD) moment, as shown in Fig. 2.12c, lower panel. Figure 2.12d shows the dependence of quasi-BIC radiative Q factor on the asymmetry. The radiative Q factor drops with increase of α and

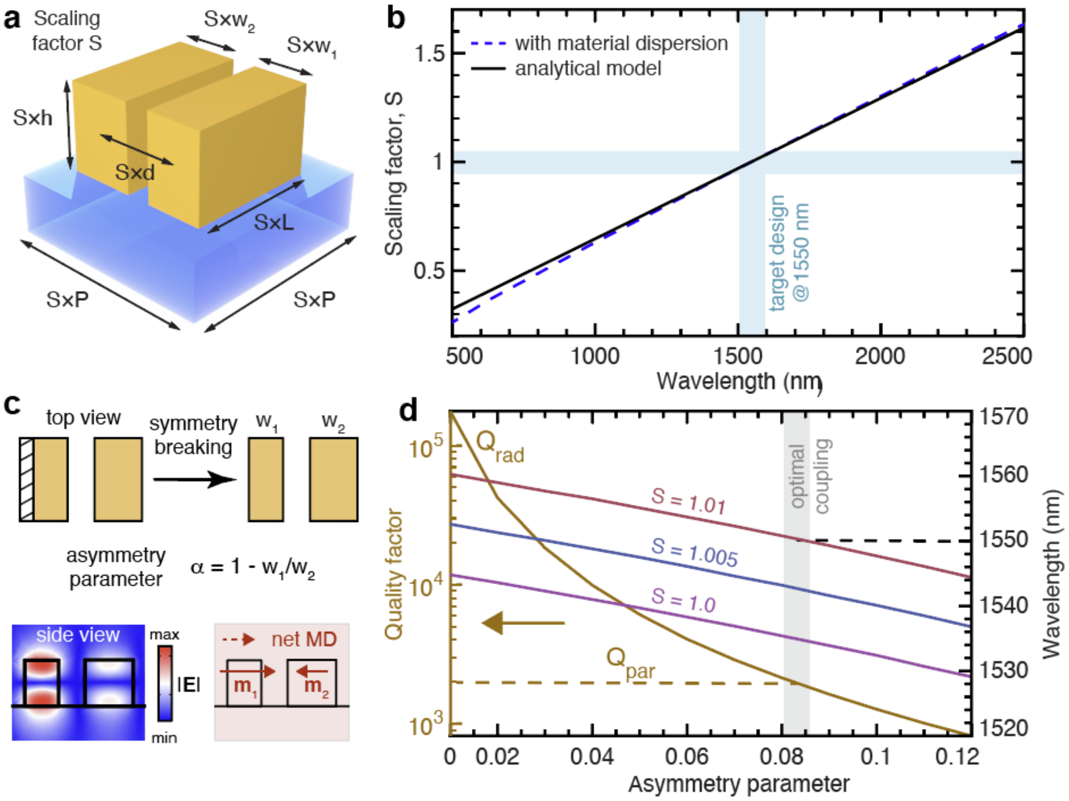

Figure 2.12: Metasurface optimization procedure. (a) Design of the metasurface unit cell with period p composed of parallel Si bars of widths w_1 and w_2, length L, height h, and with distance between bar centers d. Each geometrical parameter is multiplied by the scaling factor S. (b) BIC wavelength dependence on S for fixed refractive index and material with realistic dispersion. (c) Definition of asymmetry parameter α and electric field distribution for the quasi-BIC. (d) Dependence of Q_{rad} (left y-axis) and resonant wavelength (right y-axis) on α. The wavelength dependence is calculated for $S = 1, 1.005, 1.01$. The optimal coupling regime is shown with a gray shaded area. The target wavelength of 1550 nm is shown with a black dashed line.

the optimal coupling regime $Q_{\text{rad}} = Q_{\text{par}}$ is achieved for $\alpha = 0.085$. Figure 2.12d also shows the dependence of resonant wavelength on asymmetry parameter for three different scaling factors in the vicinity of $S \simeq 1$. One can see that the initial design with $S = 1.0$ is close to the target design only for $\alpha \simeq 0$ where the mode is out of the optimal coupling regime. Thus, additional adjustment of S is required and the target design can be achieved for $S = 1.01$. In this case the resonant wavelength is 1550 nm and the optimal coupling condition is satisfied.

2.5 Summary

To summarize this chapter, we generalized the description of broken-symmetry metasurfaces with sharp resonances by presenting a general concept of quasi-BICs and derived the dependence of the radiative Q factor on the asymmetry parameter α. Treating quasi-BICs as quasi-normal modes we derived the general expression for radiative losses via coupling coefficient between the quasi-BIC and modes of the radiation continuum. We showed that the expression for the coupling coefficient can be decomposed into contributions of Cartesian multipoles. Using the perturbation theory for non-Hermitian systems we showed that for small α the Q factor of quasi-BICs follows $Q_{\text{rad}} \propto \alpha^2$. We confirmed the inverse square law for Q_{rad} numerically for six distinct dielectric and plasmonic metasurfaces operating in different frequency ranges and showed that the dependence holds beyond the applicability of the perturbation theory. Next, we associated the high-quality quasi-BICs with the peculiarities in scattering, derived the generalized Fano formula for transmission using the quasi-normal mode expansion of the scattering matrix and obtained analytical expressions for Fano parameters. For dielectric metasurfaces, we studied the effect of parasitic losses on the total Q factor. We found that the local field enhancement can be maximized in the so-called optimal coupling regime, which is satisfied for $Q_{\text{rad}} = Q_{\text{par}}$. We showed that this regime can be achieved by adjusting the asymmetry of the unit cell because of strong dependence of Q_{rad} on α. Finally, we presented a general procedure how to design metasurface with a high-Q quasi-BIC providing maximal local field enhancement and operating at any target wavelength.

3 Nonlinear photonics with asymmetric metasurfaces supporting quasi-BICs

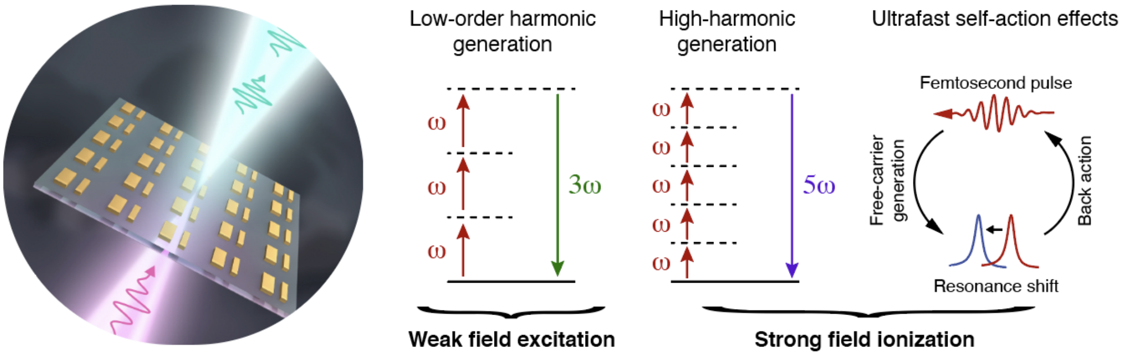

Figure 3.1: Weak and intense nonlinear optical effects in asymmetric Si metasurfaces. Left: schematic of broken-symmetry metasurface for harmonic generation. Right: schematic diagrams of harmonic generation and self-action processes.

For conventional bulk crystals the efficiency of nonlinear frequency conversion can be increased dramatically by using phase-matching or quasi-phase-matching between the pump and harmonic waves [156]. For subwavelength nonlinear metastructures, the phase-matching concept is not applicable because it requires large interaction lengths exceeding the wavelength by many times. For resonant nonlinear metasurfaces, the requirement of phase matching is replaced by the conditions of resonant field enhancement [42, 157]. The induced nonlinear polarization at the n-th harmonic frequency $P^{(n)}$ depends on the local field enhancement as

$$P^{(n)}(\omega) \propto \int_V dV\, \hat{\chi}^{(n)}(\mathbf{r})[E_{\text{loc}}(\mathbf{r},\omega)]^{(n)} \tag{3.1}$$

Assuming that at the harmonic frequency the structure is not resonant, the only parameter that defines the harmonic generation efficiency is E_{loc} which is determined by the mode Q factor and the pump coupling efficiency.

Earlier studies investigated nonlinear response of some broken-symmetry dielectric metasurfaces supporting Fano resonances for enhancement of optical nonlinearities [42, 47, 127, 158]. In Section 2.2.3 we revealed that sharp resonances in asymmetric dielectric metasurfaces originate from quasi-BICs and revealed their close link to the Fano resonances. In this chapter we study nonlinear optical effects, such as harmonic generation and self-action, in resonant dielectric metasurfaces with a broken-symmetry unit cell supporting quasi-BICs in the near-IR and mid-IR, as schematically shown in Fig. 3.1. Using the knowledge on tunability of quasi-BICs resonant properties developed in Chapter 2, we provide a general framework how to design and fabricate efficient nonlinear metasurfaces.

Throughout the chapter we consider a Si metasurface composed of a square array of parallel bar pairs with equal length but slightly different widths analysed in Section 2.4 and shown in Fig. 2.12a. The structure supports a quasi-BIC which radiation is determined by the uncompensated net magnetic dipole moment, as shown in Fig. 2.12c, lower panel. The asymmetry parameter α is defined as

$$\alpha = \frac{w_2 - w_1}{w_2}. \tag{3.2}$$

We apply the geometric scaling procedure described in Section 2.4 to tune the quasi-BIC wavelength from the visible to the near-IR and mid-IR range.

First, we investigate numerically and experimentally harmonic generation from asymmetric Si metasurfaces in the perturbative regime for pump of weak intensity. More specific, we derive general criteria for maximization of resonant nonlinear response and show that they coincide with the optimal coupling condition. We show that third-harmonic (TH) signal is increased in the vicinity of the quasi-BIC at telecom wavelengths and reaches maximum for the metasurface with optimal asymmetry parameter. We further study harmonic generation from a Si metasurface hosting a quasi-BIC in mid-IR and demonstrate fifth-harmonic generation (5HG) for low-power picosecond pulse excitation. Next, we study harmonic generation and self-action effects in resonant asymmetric Si metasurfaces in the non-perturbative regime and strong excitation pulses. We demonstrate experimentally generation of high odd harmonics up to 11-th for ultrashort femtosecond pulse excitation in mid-IR. We show that the intensity of generated harmonic drops for higher input power and explain this by the change of Si material parameters due to free-carrier generation. Using Keldysh theory for strong field ionisation we calculate the change in quasi-BIC resonant properties due to free-carrier absorption and show that the mode exhibits blueshift and strong reduction of Q factor. We apply the same theory to explain self-action effects in asymmetric Si metasurfaces with a quasi-BIC in near-IR that we observe for strong pump intensity. Finally, we study second-harmonic generation (SHG) under weak-field excitation in hybrid photonic structures composed of a two-dimensional flake of transition metal dichalcogenides integrated with an asymmetric Si metasurface. We show that SHG is enhanced by more than three orders of magnitude for the integrated structure at the quasi-BIC wavelength compared to conversion efficiency from a flake on top of an unstructured Si layer of the same thickness.

Results presented in this chapter are partially included in the published References, listed below, where I am a lead author and my contribution is in theoretical aspects, numerical simulations, metasurface design and experimental data analysis

(1) **K. Koshelev**, A. Bogdanov, Yu. Kivshar, "Meta-optics and bound states in the continuum," Science Bulletin (special issue) **64**, 836 (2019). DOI: 10.1016/j.scib.2018.12.003

(2) **K. Koshelev**, Y. Tang, K. Li, D.-Y. Choi, G. Li, Yu. Kivshar, "Nonlinear metasur-

faces governed by bound states in the continuum," ACS Photonics **6**, 1639 (2019). DOI: 10.1021/acsphotonics.9b00700

(3) (Equal first authors) N. Bernhardt*, **K. Koshelev***, S. White, K. W. Ch. M., J. E. Fröch, S. Kim, T. T. Tran, D.-Y. Choi, Yu. Kivshar, A. S. Solntsev, "Quasi-BIC Resonant Enhancement of Second-Harmonic Generation in WS2 Monolayers," Nano Letters **20**, 5309–5314 (2020). DOI: 10.1021/acs.nanolett.0c01603

(4) (Equal first authors) I. Sinev*, **K. Koshelev***, Zh. Liu*, A. Rudenko, K. Ladutenko, A. Shcherbakov, Z. Sadrieva, M. Baranov, T. Itina, J. Liu, A. Bogdanov, Yu. Kivshar, "Observation of Ultrafast Self-Action Effects in Quasi-BIC Resonant Metasurfaces," Nano Letters **21**, 8848–8855 (2021). DOI: 10.1021/acs.nanolett.1c03257

(5) (Equal first authors) G. Zograf*, **K. Koshelev***, A. Zalogina*, V. Korolev*, D.-Y. Choi, M. Zurch, C. Spielmann, B. Luther-Davies, D. Kartashov, S. Makarov, S. Kruk, Yu. Kivshar, "High-harmonic generation from resonant dielectric metasurfaces empowered by bound states in the continuum," ACS Photonics **9**, 567–574 (2022). DOI: 10.1021/acsphotonics.1c01511

3.1 Harmonic generation under weak field excitation

For harmonic generation in macroscopic nonlinear media an undepleted pump approximation is often used. This approximation implies that the nonlinear source term is sufficiently small so the input field remains undepleted on the spatial and temporal scale of nonlinear interaction [156]. For nanostructured media the interaction volume is much smaller, the material nonlinearity is not high enough, and the frequency conversion efficiency is usually far beyond 10^{-2}. Thus, the undepleted pump approximation remains a handy tool for analysis of many nonlinear processes as long as the input intensity does not exceed threshold values of order of dozens of GW·cm^{-2}.

3.1.1 Nonlinear optimal coupling regime

In this subsection we extend the optimal coupling model (see Section 2.3) to description of nonlinear response and determine optimal conditions for enhancement of resonant nonlinearities at the quasi-BIC resonance. From Section 2.3 we recall that the linear field $\mathbf{E}^{(\omega)}$ at the resonant frequency of the quasi-BIC $\omega = \omega_0$ is

$$\mathbf{E}^{(\omega)}(\mathbf{r}) = a(\omega)\mathbf{E}(\mathbf{r}), \tag{3.3}$$

where $a(\omega)$ is the resonant amplitude

$$a(\omega) \propto \frac{Q_{\text{tot}}}{(Q_{\text{rad}})^{1/2}} E_{\text{inc}}. \tag{3.4}$$

---

*Equal contributions

For a metasurface made of material with a third-order nonlinearity $\hat{\chi}^{(3)}$, such as Si, the nonlinear polarization is given by

$$P_i^{(3\omega)}(\mathbf{r}) = \sum_{j,k,l} \chi^{(3)}_{ijkl} E_j^{(\omega)}(\mathbf{r}) E_k^{(\omega)}(\mathbf{r}) E_l^{(\omega)}(\mathbf{r}). \tag{3.5}$$

The induced electric field at the harmonic frequency 3ω can be expanded over resonant states $\mathbf{E}_m$ with eigenfrequencies close to 3ω. The density of states is much higher for the harmonic frequency than that for the fundamental one so we assume that the response cannot be described with a single resonance and leave the summation over m

$$\mathbf{E}^{(3\omega)}(\mathbf{r}) = \sum_m b_m(3\omega)\mathbf{E}_m(\mathbf{r}). \tag{3.6}$$

Here, $b_m(3\omega)$ are the resonant amplitudes at 3ω frequency. They are proportional to the overlap between the mode field and the nonlinear polarization

$$b_m(3\omega) \propto \int dV\, \mathbf{E}_m(\mathbf{r}) \cdot \mathbf{P}^{(3\omega)}(\mathbf{r}) = a^3(\omega) \sum_{i,j,k,l} \int dV\, E_{m,i}(\mathbf{r}) E_j^{(\omega)}(\mathbf{r}) E_k^{(\omega)}(\mathbf{r}) E_l^{(\omega)}(\mathbf{r}). \tag{3.7}$$

The local field enhancement at the harmonic frequency can be calculated as

$$\frac{|E_{\text{loc}}|^2}{|E_{\text{inc}}|^6} \propto \left|\frac{a(\omega)}{E_{\text{inc}}}\right|^6 \propto \left[\frac{Q_{\text{tot}}^2}{Q_{\text{rad}}}\right]^3. \tag{3.8}$$

Finally, for quasi-BIC resonances in broken-symmetry metasurfaces we can write

$$Q_{\text{rad}} = Q_{\text{par}}\alpha_{\text{opt}}^2/\alpha^2, \tag{3.9}$$

so the nonlinear local field enhancement is given by

$$\frac{|E_{\text{loc}}|^2}{|E_{\text{inc}}|^6} \propto Q_{\text{par}}^3 \left[\frac{\alpha^2/\alpha_{\text{opt}}^2}{\left(\alpha^2/\alpha_{\text{opt}}^2+1\right)^2}\right]^3. \tag{3.10}$$

We note that the mode volume V does not appear in the expression because we account for the exact field distribution of $\mathbf{E}^{(\omega)}(\mathbf{r})$ to calculate the overlap integral in Eq. 3.7 and do not approximate it as a local field at the hotspot.

Equation 3.10 shows that the optimal coupling condition for the maximal nonlinear local field enhancement is identical to the expression for the linear response (see Eq. 2.31)

$$Q_{\text{rad}} = Q_{\text{par}}. \tag{3.11}$$

We note that within the perturbative approach we used the condition Eq. 3.11 holds for any harmonic number.

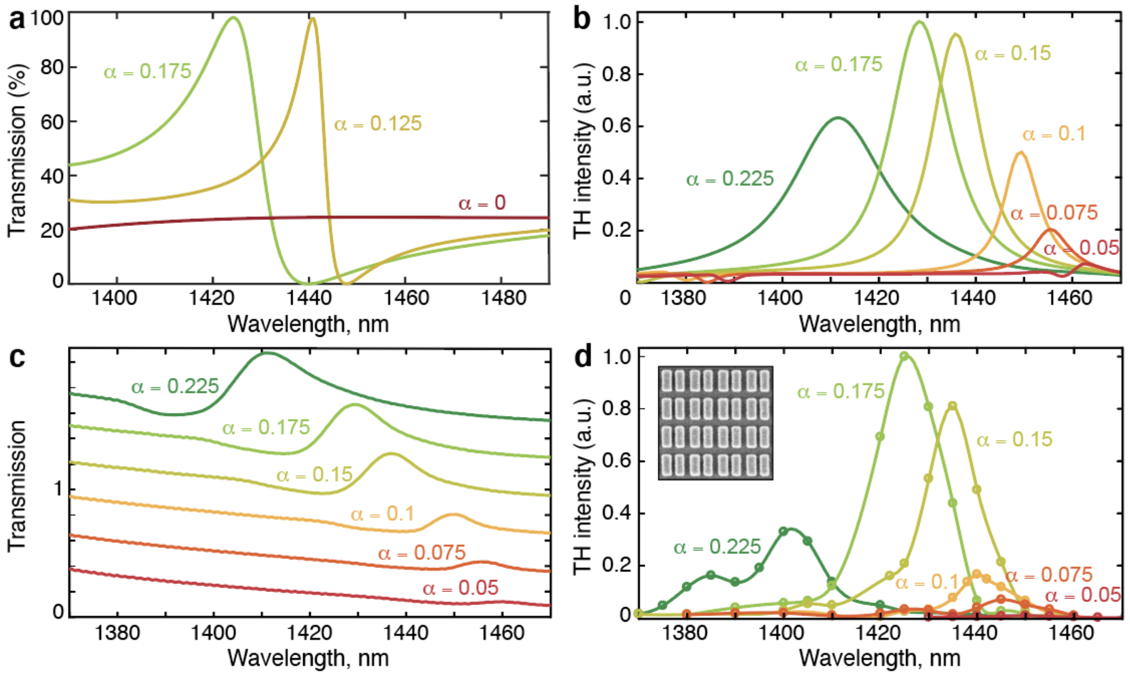

Figure 3.2: (a,b) Simulated dependence of transmission (a) and TH intensity (b) spectra with respect to α. (c,d) Measured dependence of transmission (c) and TH intensity (d) spectra with respect to α. The inset in (d) shows the SEM image of the fabricated metasurface.

3.1.2 Third- and fifth-harmonic generation

Third-harmonic generation in the near-IR. We apply the developed strategy of smart engineering to design a Si metasurface with strong resonant nonlinearity. We use the structure shown in Fig. 2.12a with the parameters $p = 655$ nm, $L = 500$ nm, $d = 320$ nm, $h = 540$ nm, $w_2 = 200$ nm and w_1 changes from 155 to 195 nm. This set of parameters approximately corresponds to the range of scaling factors $S = 0.85 - 0.95$, defined in Section 2.4. We perform linear simulations of transmittance assuming $Q_{\text{par}}^{-1} = Q_{\text{abs}}^{-1} = 0$. The simulation procedure is described in Section A.1. The electric field of the pump wave is directed along the longest side of the bar meta-molecule. Figure 3.2a shows that the transmission spectra evolution with increase of asymmetry parameter α follows the general law as in Fig. 2.6c. For $\alpha = 0$ a true BIC exists at 1465 nm and the radiative linewidth increases with asymmetry. The results of nonlinear simulations of TH signal for different α are shown in Fig. 3.2b. Here, we intentionally put $Q_{\text{par}} = 175$ in the model by adding artificial absorption losses, see Section A.1 for more details. As we show below, this magnitude of parasitic losses is a typical value that can be achieved experimentally. We note that to estimate the TH signal enhancement we can replace the parasitic losses by absorption ones which can be seen from Eq. 3.10. We observe that the simulated TH signal is maximized for an intermediate value of $\alpha = 0.175$ not equal to zero, which is in a good agreement with the theory of optimal coupling developed earlier.

To confirm the simulation results we fabricate a set of six Si metasurfaces on a glass substrate with variable asymmetry by using the electron beam lithography. The footprint of each metasurface is 100 μm $\times$100μm. The sample geometrical parameters are based on the numer-

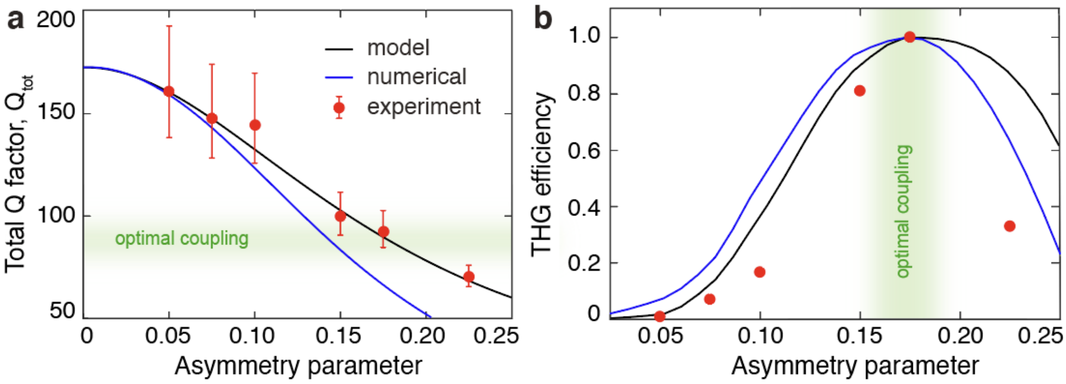

Figure 3.3: (a,b) The dependence of the total Q factor (a) and maximal THG conversion efficiency (b) on α extracted from the measured data (red circles) and calculated numerically (blue line), and analytically (black line). The error bars show the precision of the fitting procedure. The analytical model is based on Eq. 2.32 in panel (a) and Eq. 3.10 in panel (b). The range of parameters satisfying the optimal coupling condition is shown with a green blurred area.

ical design. The scanning electron microscopy (SEM) image for one of the fabricated metasurfaces is shown in the inset of Fig. 3.2d. We pump the metasurfaces from top in the wavelength range from 1370 to 1470 nm with a plane wave linearly polarized along the longest side of the bar. For the linear measurements, the pump wave is generated with a halogen white light passing a Glan-Thompson linear polarizer. The transmitted light in both polarizations is spectrally resolved with a NIR Andor spectrometer. For nonlinear optical measurements, we use a fs laser pulses with forming linearly polarized plane waves generated with a coherent optical parametric amplifier and focused to a spot size of 20 μm. The generated TH signal is collected in the forward direction with a high NA objective. The origin of the TH signal is verified by the direct measurement of its spectrum and its cubic dependence on the pump power.

The measured transmittance and TH intensity spectra for the samples with $\alpha = 0.05, 0.075, 0.1, 0.15, 0.175, 0.225$ is shown in Figs. 3.2c and d, respectively. The mode positions in the experimental linear spectra agree well with the simulation results in Fig. 3.2a, while the linewidths are broadened due to parasitic losses. As outlined before, we introduced artificial absorption to include the effect of parasitic losses. Such model is suitable for quantitative estimation of the field and nonlinear signal enhancement but leads to strong difference in peak shapes in experimental and numerical results because of principal difference is loss mechanisms of absorption and scattering. The experimental nonlinear spectra show remarkably good agreement with numerical results in Fig. 3.2b. The optimal sample is characterized by asymmetry parameter $\alpha = 0.175$. We collect experimental and numerical data to analyse the range of validity of optimal coupling theory developed earlier. A comparison of the dependence of the total Q factor on α for measured, simulated, and calculated analytically data is shown in Fig. 3.3a. The experimental Q factor is extracted from the measured data by the fitting procedure described in Appendix A.1. The value of the parasitic Q factor $Q_{\text{par}} = 175 \pm 30$ is extrapolated as $Q_{\text{par}} = Q_{\text{tot}}(0)$. We estimate the optimal asymmetry parameter $\alpha_{\mathrm{opt}} = 0.18$ using Eq. 2.33 and calculating $\tilde{Q} = 5.67$ from Eq. 2.18 for small α. The black solid line in Fig. 3.3a shows the calculations using the model in Eq. 2.32 with $Q_{\mathrm{par}} = 175$ and $\alpha_{\mathrm{opt}} = 0.18$. The green blurred area shows the range of $0.16 \leq \alpha_{\mathrm{opt}} \leq 0.2$ when the optimal coupling condition $Q_{\mathrm{rad}} = Q_{\mathrm{par}}$ is satisfied. In experiments, the optimal coupling regime is achieved for $\alpha = 0.175$ which is in a good agreement with α_{opt}. Figure 3.3b shows the dependence of the maximal values of the THG conversion efficiency on α based on the measured data, simulations, and analytical model in Eq. 3.10. The data shown in the figure is normalized independently. From nonlinear measurements, the metasurface with $\alpha = 0.175$ gives the best nonlinear performance in perfect agreement with the predictions of the optimal coupling model and the data extracted in Fig. 3.3a.

Third- and fifth-harmonic generation in the mid-IR. We design a metasurface supporting magnetic dipole quasi-BIC in the mid-IR using the same approach as before. The metasurface parameters are $p = 2040$ nm, $h = 1150$ nm, $L = 1445$ nm, $w_2 = 595$ nm, and distance between bars is 510 nm. The width of the smaller bar w_1 is varied in the range 595 nm to 400 nm, which corresponds to $\alpha = 0 - 0.33$, respectively. This set of parameters approximately corresponds to the range of scaling factors $S = 2.5 - 2.8$, defined in Section 2.4. The calculated transmission spectra are shown in Fig. 3.4a. A symmetric metasurface with $\alpha = 0$ supports a BIC at 3978 nm, while for $\alpha = 0.19$ and $\alpha = 0.1$, the transmission curves reveal a sharp resonance with a Fano lineshape. As before, we expect that the parasitic losses affect the fabrication quality so the realistic Q_{par} is estimated as of about few hundred. The numerical estimations based on Eq. 2.33 give $\alpha_{\mathrm{opt}} = 0.2$.

We fabricate a set of α-Si metasurfaces on optically thick sapphire substrate with α in the range from 0.05 to 0.33. The sample geometrical parameters are based on the design above, the sample footprint is 300×300 μm^2. The SEM image of metasurface is shown in Fig. 3.4b. In nonlinear experiments, we pump the samples with a focused pulses of $\tau = 2$ ps duration generated by the mid-IR optical parametric generator. We detect the harmonic signal with cooled near-IR detectors in spectrometers. We determine the optimal sample tuned to the nonlinear optimal coupling regime with asymmetry parameter $\alpha \simeq 0.2$ performing THG spectroscopy. This value is in perfect agreement with the theoretical prediction. We use the optimized sample for high-harmonic measurements. Figure 3.4c shows the measured harmonic spectra for pump wavelength of 3805 nm. They reveal two distinct peaks, one corresponds to THG at the wavelength of 1270 nm, another corresponds to 5HG at 760 nm. The last peak overlaps with broad emission signal due to photoluminescence. Figure 3.4c shows the power-to-power dependence of the harmonic signals on the pump intensity. We observe clear 3-rd and 5-th power scaling confirming that the measurements are done in the perturbative regime.

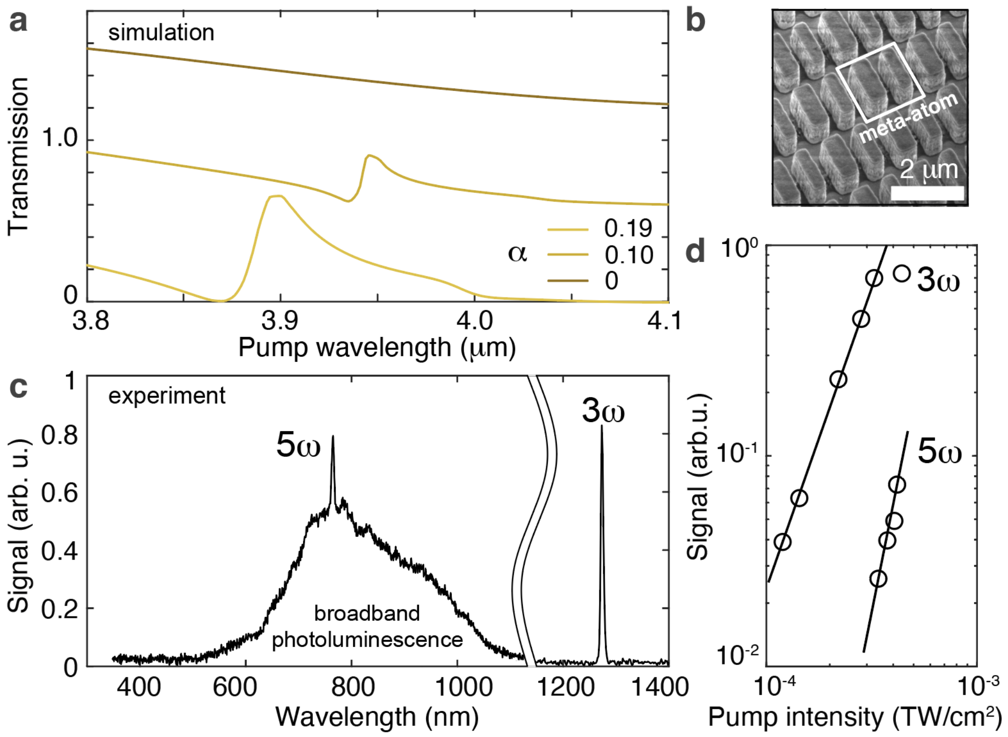

Figure 3.4: (a) Simulated dependence of transmission spectra with respect to α. For clarity the spectra are shifted relatively by 0.6 units along the vertical axis. (b) SEM image of the fabricated metasurface. (c) Measured spectrum of the 3rd and 5th optical harmonics generated by 2 ps laser pulses for the sample with $\alpha = 0.2$. Broad emission signal corresponds to photoluminescence. (d) Measured power-to-power dependence of 3rd and 5th harmonics for 2 ps pump pulses for the sample with $\alpha = 0.2$.

3.2 Harmonic generation and self-action effects under strong field excitation

For intense ultrafast pulse excitation material parameters of solids with strong nonlinear response, such as silicon, are modified substantially [159]. More specific, the generation of harmonics with photon energies below the band gap in Si metasurfaces is affected by free carrier generation [160] due to dominating mechanism of the intraband nonlinear Bloch oscillations over the interband electron-hole recombination. Increase of free-carrier plasma density modifies the dielectric function of Si which affects the resonant properties of the metasurface and leads to self-action effects and non-perturbative character of harmonic generation. More specific, carrier ionization and refractive index changes results in a spectral shift of the resonant wavelength with respect to the central frequency of the pulse [49, 161]. Recently, the blueshift of the TH wavelength associated with the photon acceleration effect and self-action was observed in Mie-resonant Si metasurfaces in the infrared range [162]. As demonstrated in the recent experiments with time-varying asymmetric metasurfaces, the self-action effects allow to control the dynamics of linear and nonlinear signals on the time scales comparable with the pulse duration [163–165].

In this Section we analyse the self-action effects for optical harmonic signals in broken-symmetry Si metasurfaces in the regime of ultrafast intense pulse excitation. We develop a theoretical approach to describe temporal dynamics of free-carrier generation in resonant metasurfaces using the Keldysh theory of strong field ionization and temporal coupled-mode theory. We use the developed method to calculate the change of material properties of Si metasurfaces supporting the quasi-BIC resonance in the mid-IR and near-IR and explain the experimentally observed blueshift and resonance broadening for third-harmonic (near-IR) and high-harmonic (mid-IR) signals.

3.2.1 Theory of strong field ionization

To explain how the material properties of Si metasurfaces are modified under strong intensity excitation, we calculate the spatiotemporal population dynamics of free-carriers driven by the resonant field. We first derive the expression for the total electric field inside the metasurface for the resonant conditions re-writing Maxwell's equations in the form of the temporal coupled-mode theory. Using the resulting field we evaluate the rate of free-carrier generation via tunneling and multi-photon absorption processes using the quantitative model, originally proposed by Keldysh [166] and generalized later [167]. Finally, we use the Drude model to estimate the changes in the refractive index and extinction coefficient due to increased free-carrier density.

Temporal dynamics of the resonant field We first analyse the temporal evolution of the total field inside the metasurface at the resonance conditions. The total electric field $\mathbf{E}(\mathbf{r}, t)$ can be expanded in contributions of the background field $\mathbf{E}_{\text{bg}}(\mathbf{r}, t)$ and the scattered field $\mathbf{E}_{\text{sc}}(\mathbf{r}, t)$. The field $\mathbf{E}_{\text{bg}}(\mathbf{r}, t)$ satisfies the Helmholtz's equation for the free space, here, we do not take substrate into account. The scattered field can be expressed through $\mathbf{E}_{\text{bg}}(\mathbf{r}, t)$ and full dyadic Green's function of the resonant system using the Lippmann–Schwinger integral equation. By expanding the Green's function into contributions of RSs (for more details see Appendix A.3.1) we get

$$\begin{aligned}
\mathbf{E}_{\text{sc}}(\mathbf{r}, t) &= \sum_n a_n(t)\frac{\mathbf{E}_n(\mathbf{r})}{N_n}, \\
a_n(t) &= e^{-i(\omega_n - i\gamma_n)t}\int_{-\infty}^{t} dt' e^{i(\omega_n - i\gamma_n)t'} s_n\left(t'\right), \\
s_n(t) &= -\int d^3r'\left(\varepsilon\left(\mathbf{r}'\right)-1\right)\mathbf{E}_n\left(\mathbf{r}'\right)\cdot\frac{\partial}{\partial t}\mathbf{E}_{\text{bg}}\left(\mathbf{r}', t\right).
\end{aligned} \tag{3.12}$$

Here, the scattered field is directly expanded into the RS contributions (with frequencies $\Omega_n = \omega_n - i\gamma_n$) with amplitudes a_n inside the metasurface because it satisfies the boundary conditions of outgoing waves. The constant N_n is the RS normalization.

By these substitutions we re-wrote the Maxwell's equations to the form of the temporal coupled mode theory

$$\frac{d}{dt}a_n(t) = -i\left(\omega_n - i\gamma_n\right)a_n(t) + s_n(t). \tag{3.13}$$

We consider that the pump frequency ω is close to the quasi-BIC frequency ω_0, so we leave only the term with $n = 0$ in the expansion of the scattered field. We consider a pulse with a full-width-at-half-maximum τ_{FWHM} of few hundred of femtoseconds. We introduce the characteristic temporal length $\tau_{\text{sp}} = d/c$, where d is the characteristic size scale of the metasurface unit cell. The quasi-BIC radiative lifetime can be calculated as $\tau_0 = 1/(2\gamma_0)$. The estimations for the realistic conditions give $d \sim 1$ μm, $\gamma_0 \sim 5$ THz, which gives $\tau_{\text{sp}} \sim 3$ fs, $\tau_0 \sim 100$ fs. Thus, inside the metasurface volume we can neglect spatial evolution of the pulse compared on the time scale of one oscillation and the pulse duration $|\mathbf{r}|/c \sim \tau_{\text{sp}} \ll (\tau_{\text{FWHM}}, \tau_0)$. In this approximation we can separate $\mathbf{r}$ and t for the background field when we calculate $s_0(t)$

$$\mathbf{E}_{\text{bg}}(\mathbf{r}, t) = \mathbf{E}_{\text{bg}}(\mathbf{r}, \omega_0)u(t). \tag{3.14}$$

Since $\omega \sim \omega_0 \gg 1/\tau_{\text{FWHM}}$

$$\dot{u}(t) = -i\omega u(t). \tag{3.15}$$

We consider the metasurface is pumped by an x-polarized non-chirped pulse with Gaussian profile centered at $\omega \sim \omega_0$. The spatial dependence of the background field is given by a monochromatic p-polarized plane wave propagating along the positive z-direction

$$\begin{aligned} &\mathbf{E}_{\text{bg}}(\mathbf{r}, \omega_0) = \hat{\mathbf{e}}_p E_{\text{inc}} e^{ik_0 z}, \\ &u(t) = e^{-t^2/\tau^2} e^{-i\omega t}, \\ &\tau = \tau_{\text{FWHM}}/\sqrt{2\ln(2)}. \end{aligned} \tag{3.16}$$

Then the resonant amplitude is

$$a_0(t) = \frac{c\tau\sqrt{2\pi i S_{\text{u}}}}{2}\kappa_{0,p} e^{\gamma_0^2\tau^2/4} e^{-i(\omega_0 - i\gamma_0)t}\, \text{Erfc}\left[\frac{\gamma_0\tau}{2} - \frac{t}{\tau}\right] E_{\text{inc}}, \tag{3.17}$$

where $\kappa_{0,p}$ is the coupling amplitude defined in the previous sections (see Eq. 2.11), and S_{u} is the unit cell area.

Dynamics of free-carriers Next we study the temporal dynamics of free-carrier generation in Si metasurfaces under the applied field. We can calculate the free-carrier density as [160]

$$\frac{\partial n_p(\mathbf{r})}{\partial t} = R(t, \omega, |\mathbf{E}(\mathbf{r}, t)|) \tag{3.18}$$

Here, the generation rate R is calculated using the Keldysh expression, see Appendix. A.6.

The Keldysh parameter is the main parameter that defines the generation rate. It is defined as

$$\gamma_K(\mathbf{r}) = \frac{\omega\sqrt{m^*\Delta}}{\mathrm{e}|\mathbf{E}(\mathbf{r}, t)|}. \tag{3.19}$$

Here, Δ is the intrinsic Si band gap, m^* is the reduced mass of the effective electron and hole masses. The resonant field is inhomogeneous, so the Keldysh parameter depends on the spatial coordinate inside the metasurface. For our estimations, we evaluate γ_K at the hotspot of the quasi-BIC ($\mathbf{r} = \mathbf{r}_h$). The MD mode has the hotspot in the x component of E-field, so

$$|\mathbf{E}(\mathbf{r}_h, t)| = \left| E_{\mathrm{bg},x}(\mathbf{r}_h)\, e^{-t^2/\tau^2} + \frac{E_{0,x}(\mathbf{r}_h)}{N_0} a_0(t) \right| \tag{3.20}$$

The change of Si permittivity can be estimated using the Drude model

$$\begin{aligned}
\Delta\varepsilon_{\mathrm{D}} &= \mathrm{Re}[\Delta\varepsilon] + i\,\mathrm{Im}[\Delta\varepsilon] \\
\mathrm{Re}[\Delta\varepsilon] &= -\frac{\omega_p^2}{\omega^2 + \tau_{\mathrm{D}}^{-2}} \\
\mathrm{Im}[\Delta\varepsilon] &= \frac{\omega_p^2 \tau_{\mathrm{D}}}{\omega\left(1 + \omega^2 \tau_{\mathrm{D}}^2\right)} \\
\omega_p^2 &= \frac{4\pi n_p e^2}{m*},
\end{aligned} \tag{3.21}$$

where τ_{D} is the Drude relaxation time. For $n_p \leq 10^{-19}$ cm^{-3}, τ_{D} is determined by the electron-phonon scattering process (τ_{D} = 100 fs), while for much higher densities the electron-electron scattering gives the main contribution ($\tau_{\mathrm{D}} = 1$ fs).

3.2.2 High-harmonic generation and self-action in the mid-IR

We use the fabricated broken-symmetry Si metasurfaces supporting a quasi-BIC in the mid-IR discussed in Sec. 3.1.2 to show the transition to the non-perturbative regime. In optical experiments, the metasurfaces are pumped by intense ultrashort pulses with duration of $\tau =$ 100 ps and peak intensity of 0.8 TW/cm^2. Figure 3.5a shows the measured harmonic spectra for pump wavelength of 3805 nm for the sample with asymmetry parameter $\alpha = 0.2$ which is the optimal asymmetry for low intensity excitation. The spectrum reveals four distinct peaks, corresponding to the fifth, seventh, ninth and eleventh harmonics, respectively. Additional measurements show that the dependence of the generated signal power on the pump power deviates from the perturbative power law significantly and exhibit saturation at the higher intensities, pointing to the non-perturbative character of the HHG mechanism for intense ultrashort pulses.

We next analyse how the optimal coupling condition is modified in the non-perturbative regime. In Fig. 3.5b we compare the harmonic signal from samples with different asymmetries for 100 fs high intensity pulses (5-th harmonic signal data) and for 2 ps low intensity pulses (3-rd harmonic signal data discussed in Sec. 3.1.2). For the comparison we use the enhancement factor defined independently for each set of measurements as the harmonic signal from the metasurface with specific asymmetry normalized on the signal from the metasurface giving the lowest signal. Figure 3.5b shows that for low intensity excitation the enhancement factor for the sample with $\alpha \simeq 0.2$ is much higher than for other samples which confirms that the theory of optimal coupling is valid for this set of measurements. For high intensity pulses the

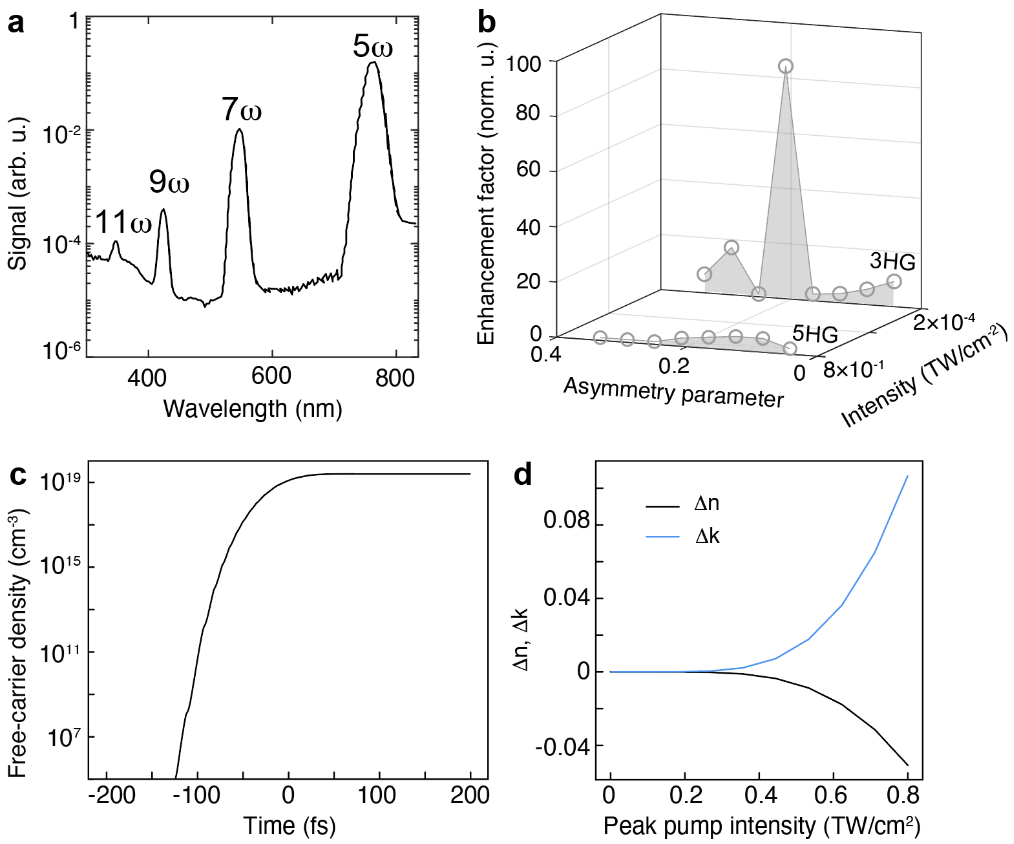

Figure 3.5: (a) Measured spectrum of HHG generated by 100 fs laser pulses. (b) Measured harmonic signal vs asymmetry parameter at different pump pulse intensities. For intensity of 0.8 TW/cm^2 the data is for 5th harmonic at $\tau = 100$ fs. For intensity 2×10^{-4} TW/cm^2 the data is for 3rd harmonic at $\tau = 2$ ps. (c) Free-carrier density temporal dynamics for 0.8 TW/cm^2 pump intensity. (d) Calculated refractive index and extinction coefficient change with respect to peak pump intensity for $\tau = 100$ fs pulses.

enhancement factor is qualitatively similar for the samples with asymmetry parameters from 0.05 to 0.2. We can conclude that there is no optimal sample in the non-perturbative regime and the optimal coupling approach is not applicable to the non-perturbative regime.

To explain this, we estimate the modification of quasi-BIC resonant properties due to free-carrier generation in Si under strong field intensity excitation. Our calculations are based on the model derived in Sec. 3.2.1. In our amorphous silicon film, one can still observe the influence of indirect bandgap edge in the absorption spectrum around 1.1 eV and broadband photoluminescent background in Fig. 3.4c, as well as the absence of harmonics below the wavelength of 380 nm (3.3 eV), that suggests that the direct transition 3.4 eV is involved for coherent HHG process. Thus, for our calculations we take $\Delta = 3.4$ eV and $m^* = 0.18 m_e$. Numerical simulations using the explicit Keldysh model show that after excitation of the quasi-BIC resonance with a Gaussian pulse at intensity 0.8 TW/cm^2 and $\tau_{\mathrm{FWHM}} = 100$ fs, the electron-hole plasma density in the field hotspots reaches $n_p = 2.5\times10^{19}$ cm^{-3} as shown in Fig. 3.5c. At the moment of the highest local field intensity the Keldysh parameter (see Eq. A.91) decreases up to $\gamma_K = 0.4$ which means the strong field ionization is dominated by the tunneling effect [167].

The electron-hole plasma induces a local change of the dielectric permittivity by the Drude correction. The change of the refractive index Δn and extinction coefficient Δk with respect to the peak pump intensity is shown in Fig. 3.5d. For the highest intensity of 0.8 TW/cm^2 the plasma frequency (see Eq. 3.21) reaches 0.67×10^{15} rad/s, which becomes comparable with that of incident light ($\omega = 0.495 \times 10^{15}$ rad/s). Such large changes of the refractive index induce a shift of the quasi-BIC resonant wavelength and decrease of its Q factor. We estimate the wavelength change $\Delta\lambda$ as $\Delta\lambda/\lambda \simeq \Delta n/n$. This gives blueshift of the quasi-BIC wavelength by 55 nm. The drop in the Q factor can be estimated by evaluating the non-radiative Q factor of Si with free-carriers as $Q_{\mathrm{abs}} = (n+\Delta n)/(2\Delta k)$. The estimation gives $Q_{\mathrm{abs}} = 16$ while the Q factor of the unperturbed mode was of order of 200. Due to smearing out of the resonant mode properties the structure cannot be described by the simple model used in Sec. 3.1.1, thus, the optimal coupling model is not applicable in the current form.

3.2.3 Self-action in the near-IR

We further extend our study of strong nonlinear effects to the near-IR. We use the metasurface design shown in Fig. 2.12a with the parameters $p = 720$ nm, $L = 550$ nm, $d = 300$ nm, $h = 500$ nm, $w_2 = 230$ nm and w_1 changes from 170 to 230 nm. This set of parameters approximately corresponds to the range of scaling factors $S = 0.95-1.0$, defined in Section 2.4. We perform simulations and measurements of transmittance and extract the resonant wavelength and the Q factor of the quasi-BIC. The Q factor dependence of α is shown in Fig. 3.6a. For very small α the Q factor saturates at the value of about 1500 which corresponds to Q_{par}. Figure 3.6b shows the measured transmittance for the sample with $w_2 = 205$ nm ($\alpha = 0.11$). The inset shows the SEM image of the fabricated metasurface. The quasi-BIC wavelength for this sample is of about 1510 nm and the Q factor reaches 900 so the mode is close the optimal coupling regime. We use this sample for the further nonlinear studies.

For THG experiments we use ultrashort pulses with $\tau_{\mathrm{FWHM}} = 290$ fs. We use optical parametric amplifier to tune the pump wavelength to the spectral range of the quasi-BIC. We measure the generated TH signal in the transmission geometry. The pump is a pulse excitation with repetition rate of 1 MHz; the pulses are focused on the sample surface in the focal spot with diameter of 6 μm. The measured nonlinear spectra are contributed by a broad background component from the probe pulse and a sharp resonant feature associated with the quasi-BIC. For higher pump intensities, the resonant peak in the harmonic signal is blueshifted and broadened. Figure 3.6c shows the extracted dependence of the spectral position of the THG peak and its linewidth on the pump intensity. The TH peak blue-shifts by 0.6 nm with the change of pump power from 20 to 200 GW/cm^2. The measured mode linewidth increases to two and a half times with a growth of the pump power.

We attribute the resonance blueshift, and its broadening to the strong field intensity generation of free carriers that modifies the Si properties on ultrashort time scales less than the pulse duration. We analyse how the resonant properties of Si metasurface are changed using the numerical approach based on the resonant photoionization model (see Sec. 3.2.1).

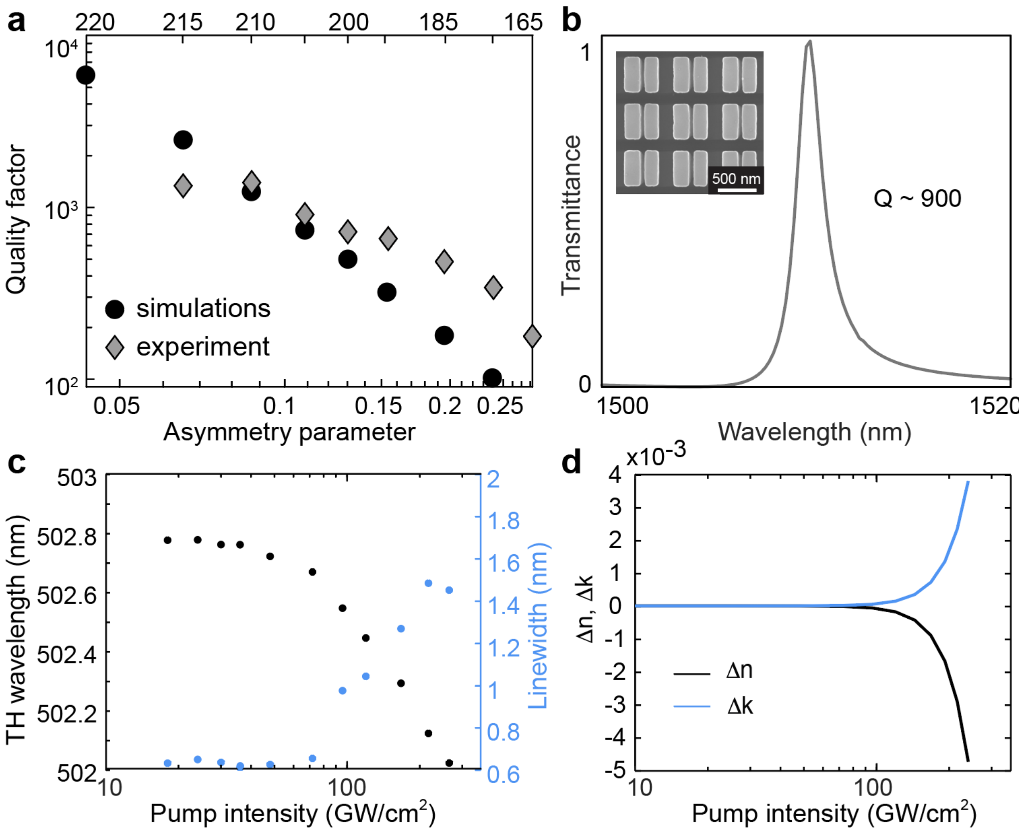

Figure 3.6: (a) Calculated (black) and measured (gray) Q factors of quasi-BIC for different α. (b) Measured transmittance for the sample with $\alpha = 0.11$. (c) Extracted dependence of the spectral position (black) of the THG peak and its linewidth (light blue) on the pump intensity. (d) Calculated refractive index and extinction coefficient change with respect to peak pump intensity.

In the model we use the direct bandgap of Si $\Delta = 3.4$ eV. Numerical simulations using the model show that after excitation of the quasi-BIC resonance with a Gaussian pulse at intensity 240 GW/cm^2 and $\tau_{\text{FWHM}} = 290$ fs, the electron-hole plasma density in the field hotspots reaches $n_p = 4.7 \times 10^{18}$ cm^{-3}. At the moment of the highest local field intensity the Keldysh parameter (see Eq. A.91) decreases up to $\gamma_K = 1.6$ which means the strong field ionization is induced by the interplay between multiphoton absorption and the tunneling effect [167]. The electron-hole plasma induces a local change of the dielectric permittivity by the Drude correction. The change of the refractive index Δn and extinction coefficient Δk with respect to the peak pump intensity is shown in Fig. 3.6d. For the highest intensity of 240 TW/cm^2 the plasma frequency (see Eq. 3.21) reaches 0.3×10^{15} rad/s. In the model, we assume that the induced change of refractive index Δn and extinction Δk is homogeneous within the unit cell. The model results are in good quantitative agreement with the experimental data for the line width and peak blueshift. The wavelength change in Fig. 3.6c follows the trend of the refractive index change Δn in Fig. 3.6d, and the same holds for the change of the linewidth with respect to the change of Δk. We estimate the resonant wavelength change $\Delta\lambda$ as $\Delta\lambda/\lambda \simeq \Delta n/n$. This gives blueshift of the quasi-BIC wavelength by 2.2 nm so the associated TH wavelength blueshift is 0.7 nm. This value is in the good qualitatively agreement with the measured blueshift of 0.6 nm shown in Fig. 3.6c. The drop in the Q factor can be estimated by evaluating the non-radiative Q factor of Si with free-carriers as $Q_{\text{abs}} = (n+\Delta n)/(2\Delta k)$. The estimation gives $Q_{\text{abs}} = 470$ which means the linewidth is increased in about two times. This is also in the good qualitatively agreement with the experiment results.

3.3 Harmonic generation in metasurfaces hybridized with two-dimensional Van der Waals materials

One of the frontiers at the intersection of nonlinear optics and quantum photonics is hybrid metasurfaces integrated with two-dimensional Van der Waals materials such as transition metal dichalcogenides (TMDs) [108, 168, 169]. Monolayers of TMDs with atomic thickness provide advanced optical properties including large exciton binding energy and strong excitonic emission. Another promising property of TMD monolayers is their strong optical nonlinearities of second-order enabling enhanced generation of even harmonics [170, 171]. However, compared to bulk crystals, the intrinsic nonlinear susceptibility of TMD monolayers is weak. For enhancing the optical nonlinearities it was suggested to hybridize the TMD monolayers with resonant photonic structures [172, 173].

In this section we analyse how the resonant asymmetric metasurface modify the nonlinear response of a TMD monolayer positioned on top of it in the regime of weak intensity pump. We use the design of the Si metasurface composed of square lattice of parallel bar pairs on top of glass substrate discussed in Sec. 2.4. The metasurface parameters are $p = 500$ nm, $h = 160$ nm, $L = 245$ nm, $w_2 = 180$ nm, and distance between bars is 100 nm. The width of the smaller bar w_1 is varied in the range 120 nm to 140 nm, which corresponds to $\alpha = 0.22-0.33$, respectively. This set of parameters approximately corresponds to the range of scaling factors $S = 0.3-0.7$, defined in Section 2.4. The metasurface is integrated with a WS_2 monolayer placed on the top of the metasurface as schematically shown in Fig. 3.7a.

The designed metasurface supports the MD quasi-BIC at 830 nm. We fabricate a set of metasurfaces with a range of asymmetry parameters using the target design. The structures are composed of hydrogenated α-Si on a transparent substrate. The metasurface footprint is 30 µm × 30 µm. For references for nonlinear experiments, we fabricate a 50 µm × 50 µm bulk Si film with the same thickness. We perform linear reflectance measurements and extract the total Q factor $Q = 35 \pm 5$. We select the optimal sample among the metasurfaces doing SH spectroscopy of bare Si metasurfaces shown in Fig. 3.7b. The observed SH signal is nonzero due to asymmetry of the unit cell that breaks the inversion symmetry of the sample. The optimal sample is with $w_1 = 140$ nm ($\alpha = 0.22$) exhibits the highest SH intensity with the peak value at the quasi-BIC wavelength. The sample SEM image is shown in Fig. 3.7c, top panel.

For nonlinear measurements of integrated structures, we transfer mechanically exfoliated monolayer WS_2 flakes on the optimal sample and the reference Si film. Figure 3.7c (bottom panel) shows optical microscope image of the metasurface after the flake transfer. Both the

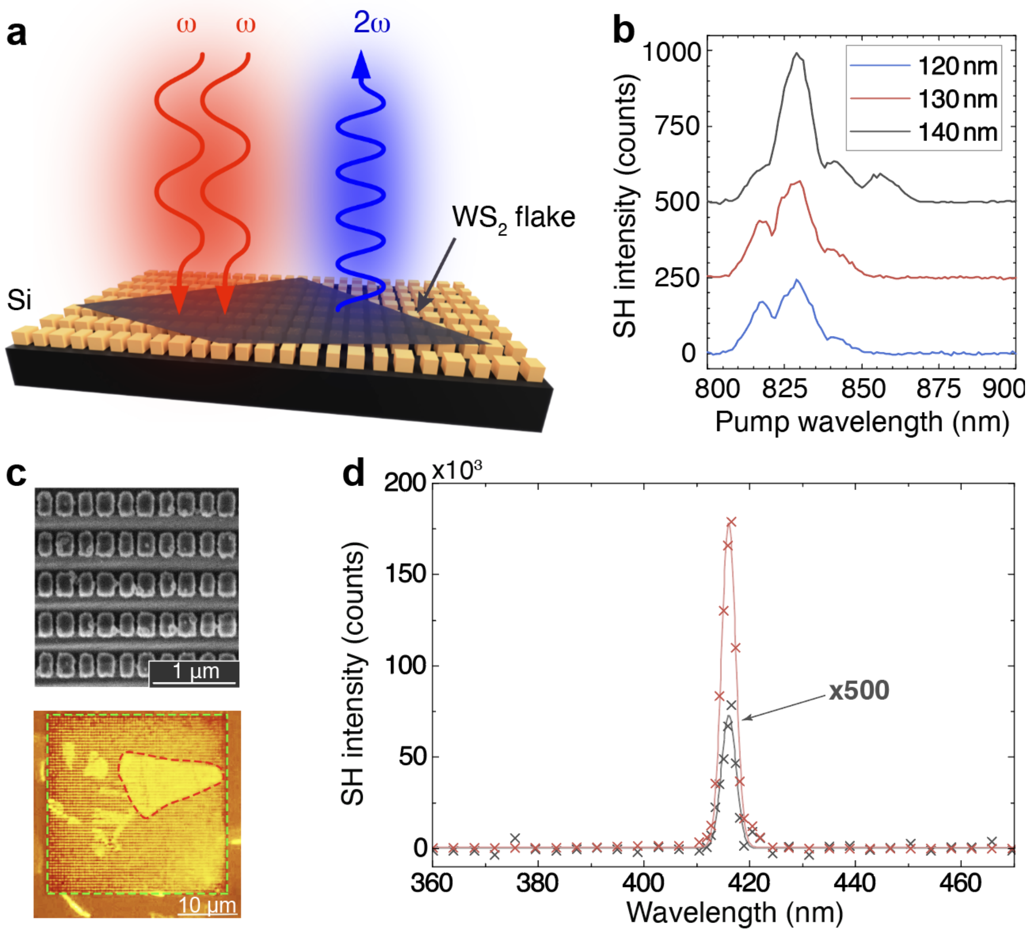

Figure 3.7: (a) Schematic of SHG from a WS_2 monolayer placed on top of a Si metasurface composed of a square array of bar pairs. (b) Measured SH intensity spectra for bare metasurfaces with the width of the smaller bar of 120, 130, and 140 nm, respectively. The spectra are shifted by 250 counts. (c) The SEM image (top) and optical microscopy image (bottom) of one of the fabricated metasurfaces. The bottom image shows the metasurface with a WS_2 flake on top of it. (d) Measured SH intensity spectra from WS_2 monolayers on top of the optimized metasurface (red) and on top of the reference bulk Si film (gray, magnified 500×) with a pump wavelength of 832 nm.

reference Si film and metasurface are partially covered by large uniform flakes of about 40 µm × 16 µm and 17 µm × 11 µm size, respectively. The advanced transfer method ensures the quality and the number of layers in the flakes, which is additionally verified with PL measurements.

In nonlinear measurements of SH signal from the WS_2 monolayers on top of Si metasurfaces, we pump the structures at the wavelength of 832 nm with 80 fs laser pulses and the average pump power of 22 mW. The spot diameter is 12 µm, which is comparable to the flake size and allows for more efficient excitation of the resonant quasi-BIC in the metasurface. We collect the backward-emitted SH signal spectra for WS_2 monolayer flakes on top of the optimal metasurface and the reference film, the results are shown in Fig. 3.7d. The measured SHG enhancement is more than 1100 higher for the flake on the resonant Si metasurface compared to a flake on top of the reference Si film of the same thickness. To confirm the SH origin of the emitted nonlinear signal, we measure power-to-power dependence of the average collected SH power on the average pump intensity which shows clear quadratic behaviour.

3.4 Summary

To summarize this chapter, we investigated nonlinear response of broken-symmetry metasurfaces supporting quasi-BICs with large radiative Q factor. We showed analytically that the nonlinear response of resonant metasurfaces in the regime of weak field excitation is maximized in the nonlinear optimal coupling regime. We showed analytically that the nonlinear optimal coupling regime is achieved for the same optimal asymmetry parameter as the linear optimal coupling regime with equal rates of radiative and parasitic losses. Using the design of Si metasurface composed of a square lattice of parallel bar pairs, we have shown numerically and experimentally that the THG and HHG in the perturbative regime is maximised at the quasi-BIC resonance for weak pump intensities. We studied experimentally nonlinear response of two different quasi-BIC metasurfaces for strong field excitation in the near-IR and mid-IR, respectively. For the mid-IR excitation with sub-ps focused pulses we observed generation of odd harmonics up to eleventh order with non-perturbative dependence of harmonic signal on the pump power. For the near-IR excitation we observed THG with signal intensity depending on the pump intensity in the non-perturbative way. We observed blueshift and linewidth broadening for the high-harmonic signal (for the mid-IR metasurface) and third-harmonic signal (for the near-IR metasurface) and attributed them to the self-action effects. We explained the observed self-action effects by modification of Si material properties due to free-carrier generation. We developed a theoretical model of strong field ionization in resonant metasurfaces using the Keldysh theory of free-carrier generation due to multiphoton absorption and tunneling effect. We used the developed approach to calculate the density of free carriers and change of material parameters for the experimental conditions. We estimated the modification of resonant properties of the quasi-BIC and showed that the estimations agree well with the experimental results. Finally, we investigated nonlinear response of hybrid dielectric structures composed of resonant broken-symmetry Si metasurfaces and WS_2 monolayers in the regime of weak field excitation. We studied SHG from WS_2 flakes positioned on top of Si metasurfaces supporting quasi-BICs in the near-IR range. Using the optimal coupling approach we selected the optimal sample by comparing SH signal from bare Si metasurfaces with different asymmetries. For the optimal sample we showed that the SH signal from the TMD flake on top of resonant metasurface is more than three orders of magnitude stronger that for the flake on top of bare Si film of the same thickness.

4 Engineering high-quality resonances in individual subwavelength resonators

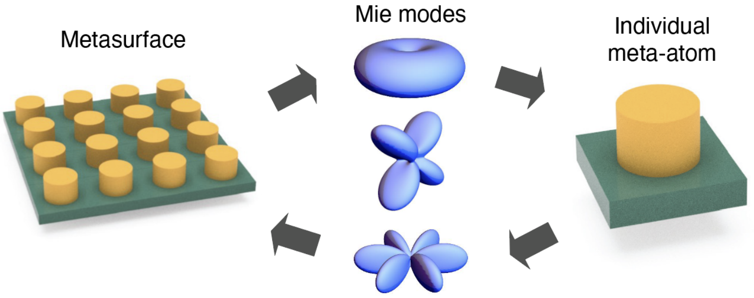

Figure 4.1: Schematic of correspondence between optical properties of metasurfaces and individual meta-atoms they are composed of. The far-field profiles of fundamental Mie modes are schematically shown in the center.

Resonant dielectric metasurfaces represent ordered ensembles of resonant subwavelength resonators, or meta-atoms, which collective response determines optical properties of the whole array [22], as schematically shown in Fig. 4.1. Below the diffraction threshold, the peculiarities of the collective lattice response are not determined by the diffractive modes of the lattice and can be directly reconstructed from the resonant response of meta-atoms by considering mutual inference of modes of individual structures [23, 174]. Engineering of optical properties of individual resonators requires analysis of resonator eigenmodes, or Mie resonances, which are determined by geometrical and material parameters of the structure.

In this chapter, we present a new mechanism of light localization in subwavelength individual dielectric resonators associated with formation of quasi-BICs. First, we make an introduction into the physics and main properties of Mie resonances and their interferences in individual dielectric meta-atoms. Next, we show that the conditions of formation of quasi-BICs in accord to the Friedrich-Wintgen mechanism can be achieved for subwavelength dielectric resonators by their deformation and shape tuning. More specific, for a dielectric disk with a variable aspect ratio we show numerically and experimentally that quasi-BICs are manifested as high-Q resonances formed at avoided resonance crossing of radially and axially oscillating Mie modes. We explain the physics of quasi-BIC formation in terms of strong coupling of interacting Mie modes which leads to their destructive interference in the far-field. We study the near- and far-field properties of quasi-BICs and show that the cancellation of radiative losses is related to the suppression of the dominant multipolar component of the field. We show numerically and experimentally that in the scattering spectra the quasi-BIC is manifested as a Lorentzian-shape Fano resonance with a diverging asymmetry parameter. We derive analytical expressions for the extinction cross section and explain the connection between peculiarities of the far-field spectra and the maximization of Q factor in terms of coupling coefficients between the pump and the quasi-BIC.

Results presented in this chapter are partially included in the published References, listed below, where I am a lead or co-lead author and my contribution is in the theoretical and conceptual aspects, eigenmode numerical simulations, resonator design and experimental data analysis

(1) M.V. Rybin, **K. Koshelev**, Z. F. Sadrieva, K. B. Samusev, A. A. Bogdanov, M. F. Limonov, Yu. S. Kivshar, "High-Q supercavity modes in subwavelength dielectric resonators," Physical Review Letters **119**, 243901 (2017). DOI: 10.1103/PhysRevLett.119.243901

(2) A. A. Bogdanov, **K. Koshelev**, P. V. Kapitanova, M. V. Rybin, S. S. Gladyshev, Z. F. Sadrieva, K. B. Samusev, Yu. S. Kivshar, and M. F. Limonov, "Bound states in the continuum and Fano resonances in the strong mode coupling regime," Advanced Photonics **1**, 016001 (2019). DOI: 10.1117/1.AP.1.1.016001

(3) **K. Koshelev**, S. Kruk, E. V. Melik-Gaykazyan, J.-H. Choi, A. Bogdanov, H.-G. Park, Yu. Kivshar, "Subwavelength dielectric resonators for nonlinear nanophotonics", Science **367**, 288-292 (2020). DOI: 10.1126/science.aaz3985

(4) (Equal first authors) M. Odit*, **K. Koshelev***, S. Gladyshev, K. Ladutenko, Yu. Kivshar, A. Bogdanov, "Observation of supercavity modes in subwavelength dielectric resonators," Advanced Materials **33**, 2003804 (2021). DOI: 10.1002/adma.202003804

(5) E. Melik-Gaykazyan, **K. Koshelev**, J.-H. Choi, S. Kruk, A. Bogdanov, H.-G. Park, Yu. Kivshar, "From Fano to quasi-BIC resonances in individual dielectric nanoantennas," Nano Letters **21**, 1765–1771 (2021). DOI: 10.1021/acs.nanolett.0c04660

(6) **K. Koshelev**, Yu. Kivshar, "Dielectric resonant metaphotonics," ACS Photonics (special issue) **8**, 102–112 (2021). DOI: 10.1021/acsphotonics.0c01315

4.1 Introduction to Mie resonances and Mie mode interferences

In this section, we overview the physical origin and fundamental properties of Mie resonances and their interferences in individual dielectric meta-atoms. In first experiments on observation of strong resonant response of dielectric nanoresonators, particles with spherical shape were used [11]. Spherical Mie particles have a number of advantages in description of their resonant properties with analytical models, such as Mie theory. From the point of view of technological feasibility in fabrication, spheres can be produced with well-developed techniques including laser printing [175] and direct laser ablation [20].

---

*Equal contributions

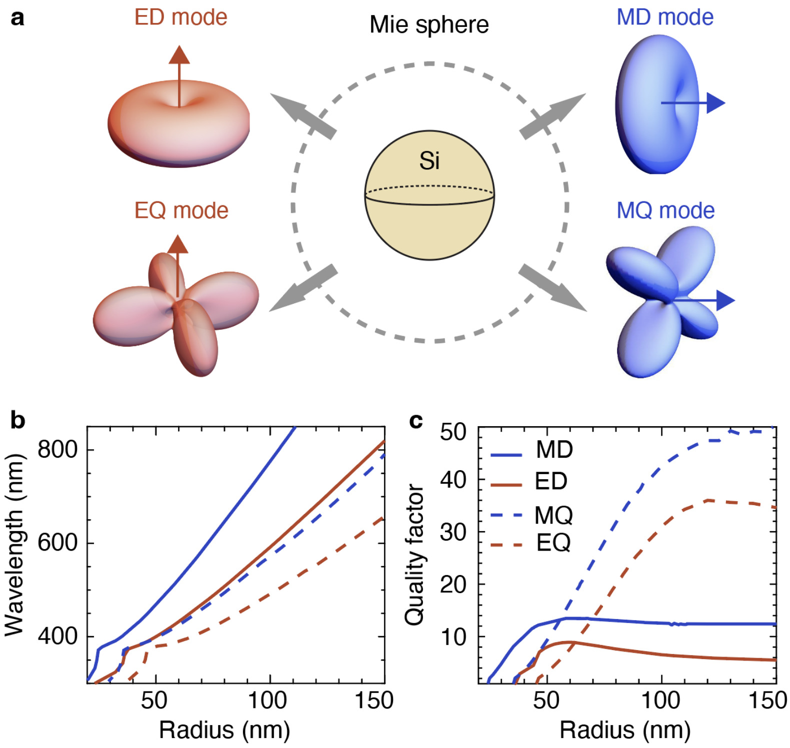

Figure 4.2: (a) Schematic of a Si nanosphere and far-field radiation patterns of its fundamental Mie modes: electric dipole and quadrupole (ED and EQ, red), and magnetic dipole and quadrupole (MD and MQ, blue). (b,c) Mode dispersion in a Si sphere for ED, MD, EQ and MQ modes. The resonant wavelength (b) and the mode Q factor (c). The calculations are for Si with realistic dispersion.

The Mie resonances are identified as self-sustained excitations of individual meta-atoms. For a non-magnetic dielectric sphere with radius R and refractive index $n=\sqrt{\varepsilon}$ the complex frequencies of Mie modes can be found from the eigenvalue equations

$$\frac{\psi_l'(nk_lR)}{\psi_l(nk_lR)} = n\frac{\xi_l'(k_lR)}{\xi_l(k_lR)}, \quad \text{electric (TM)} \tag{4.1}$$

$$\frac{\psi_l'(nk_lR)}{\psi_l(nk_lR)} = \frac{1}{n}\frac{\xi_l'(k_lR)}{\xi_l(k_lR)}, \quad \text{magnetic (TE).} \tag{4.2}$$

The prime denotes derivatives with respect to the argument, $k_l=(\omega_l-i\gamma_l)/c$ is the complex k-vector of the Mie resonance, $\psi_l(x)=x\,j_l(x)$ and $\xi_l(x)=x\,h_l^{(1)}(x)$ are the Riccati-Bessel functions of order l, and $j_l(x)$ and $h_l^{(1)}(x)$ are the spherical Bessel and outgoing spherical Hankel functions, respectively. For the spherical geometry the modes are inherently separated into electric (TM) and magnetic (TE) modes. For large refractive index the equations can be solved approximately assuming large argument $kR\gg 1$, $nkR\gg 1$ giving the resonant wavelengths of Mie modes $\lambda_{s,l}$

$$2R=\frac{\lambda_{s,l}}{2n}(2s+l), \quad \text{electric (TM)} \tag{4.3}$$

$$2R=\frac{\lambda_{s,l}}{2n}(2s+l-1), \quad \text{magnetic (TE).} \tag{4.4}$$

Here, $s = 1, 2, ..$ is the radial mode index and $l = 1, 2, ..$ is the orbital mode index. One can see that the resonant wavelengths of Mie modes are comparable with the particle characteristic size and a high refractive index is essential to engineer them in nanoparticles in the visible and near-IR spectral ranges. We note that Eqs. 4.4 show that the fundamental mode of the Mie sphere is has the magnetic nature.

To illustrate the characteristics of Mie resonances, we consider a Si sphere, schematically shown in Fig. 4.2a. For spherical particles, the mode radiation pattern represents an electric or magnetic multipole (vector spherical harmonic). Figure 4.2a shows the far-field profiles of the first four modes of a Mie sphere: electric dipole (ED), magnetic dipole (MD), electric quadrupole (EQ), and magnetic quadrupole (MQ) modes. Figures 4.2b,c show the calculated resonant wavelength and mode Q factor dependence on the sphere radius. In calculations we consider dispersive Si with absorption losses in the blue part of visible spectrum and the UV range. The dispersion relation of the modes is almost linear with the radius R and the nonlinear behaviour for small radii is explained by the absorption losses. For $R = 100$ nm sphere, the fundamental mode is the MD Mie resonance with wavelength of about 785 nm, and the second mode is the ED resonance with the wavelength of 595 nm, which is in good agreement with 800 nm and 534 nm obtained from Eq. 4.2 for $n = 4$. The calculated Q factors of modes are large for $R > 100$ nm and decrease for lower radii due to material losses of Si. The Q factor of the MD and ED modes are of order of 12 and 6, respectively, in the most part of the visible and near-IR range.

Light scattering from the dielectric sphere can be calculated by the use of the Mie theory [176]. The scattering cross-section of a linearly polarized plane wave is given by

$$\sigma_{\text{sc}} = \lambda^2 \sum_{l=1}^{\infty} \frac{2l+1}{2\pi} \left(|a_l|^2 + |b_l|^2 \right). \tag{4.5}$$

Here, a_l and b_l are the electric and magnetic Mie coefficients, respectively, defined as

$$a_l(k) = \frac{\frac{1}{n}\psi_l'(nkR)\psi_l(kR) - \psi_l'(kR)\psi_l(nkR)}{\frac{1}{n}\psi_l'(nkR)\xi_l(kR) - \xi_l'(kR)\psi_l(nkR)}, \quad \text{electric (TM)} \tag{4.6}$$

$$b_l(k) = \frac{\psi_l'(nkR)\psi_l(kR) - \frac{1}{n}\psi_l'(kR)\psi_l(nkR)}{\psi_l'(nkR)\xi_l(kR) - \frac{1}{n}\xi_l'(kR)\psi_l(nkR)}, \quad \text{magnetic (TE).} \tag{4.7}$$

One can see that the poles of Mie coefficients correspond to the dispersion equations for the Mie resonances, see Eq. 4.2. Thus, the scattering response is determined by the strength of excitation of Mie resonances. In the vicinity of each Mie resonance, the maximal scattering cross-section is limited [177]

$$\sigma_{\text{sc},l}^{\max} = \lambda^2 \frac{2l+1}{2\pi}. \tag{4.8}$$

This means, that the strength of scattering is determined by the resonant wavelength and can be comparable for electric and magnetic resonances. Moreover, since the MD resonance is fundamental, its scattering response is stronger than that of other Mie modes. We note that Eq. 4.8 and Eq. 4.4 show that the scattering efficiency at the resonance increases with the re-

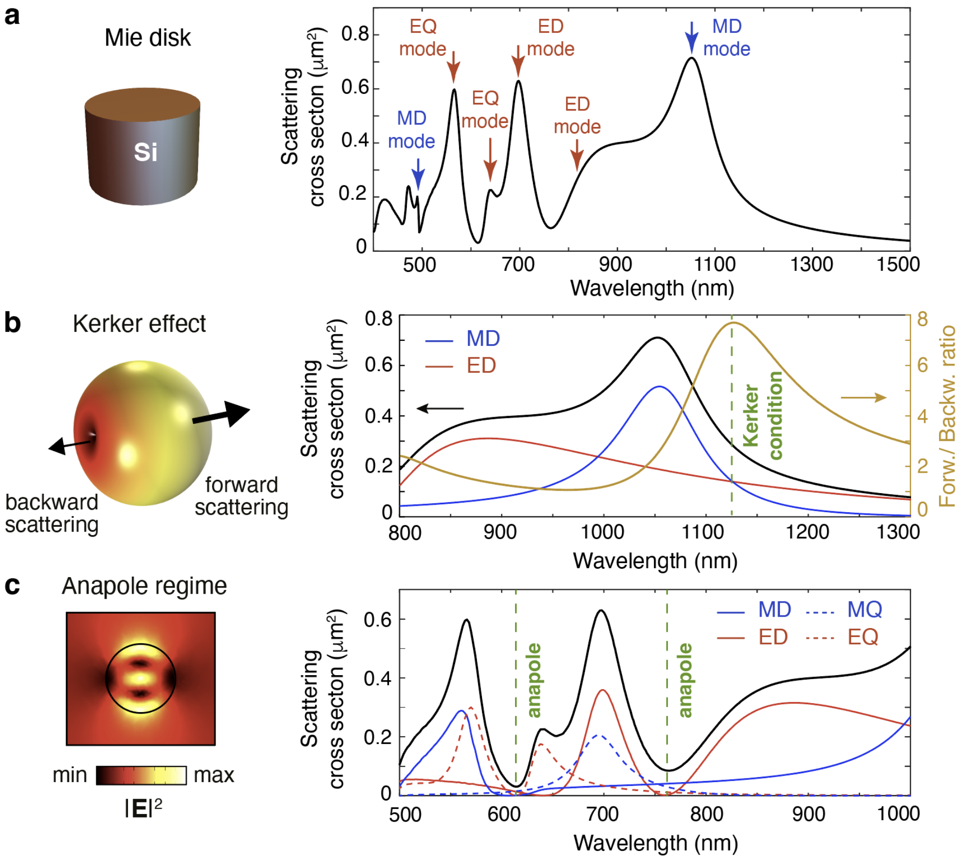

Figure 4.3: (a) Scattering cross-section of a Si nanodisk pumped by linearly-polarized plane wave propagating along its axis. In the calculations, the Si refractive index of 3.5, the disk is suspended in air and its height and diameter is 220 nm and 290 nm, respectively. The resonant wavelengths of Mie resonances are shown with arrows. (b,c) Non-resonant mode interference effects. (b) the Kerker effect - equality of magnetic and electric dipole components of the scattering field. (c) The dynamic anapole regime leading to suppression of the total scattered signal and strong near-field localisation.

fractive index as $\sigma_{\mathrm{sc},l}^{\max} \propto n^2$ which highlights the benefits of using high-index dielectrics [19].

In practice, production of ideal spherical nanoparticles is complicated, thus dielectric resonators with non-spherical geometry attracted widespread interest as meta-atoms of potential functional metastructures [178]. The fabrication of non-spherical meta-atoms of high-quality can be achieved with chemical synthesis and electron beam lithography with nanoscale resolution. Moreover, the shape and form of meta-atoms provide additional degrees of freedom than can be used to engineer the resonant response. Recent studies considered cube-shaped, prism-shaped and disk-shaped nanoparticles for advanced engineering of the scattering characteristics [179, 180]. Contrary to spherical meta-atoms, for non-spherical particles there is no explicit one-to-one correspondence between their Mie resonances and spherical harmonics, or multipoles, used to decompose the resonant far-field pattern as well as the scattered fields within the Mie theory [142, 181]. However, for subwavelength dielectric particles, especially, with highly symmetric shape, such as cylinder or cube, one multipolar component of the radiation dominates the response. Thus, effectively, we can treat each Mie mode in the approximation of one dominant multipolar radiation channel, and assign the magnetic or electric nature to the each mode. To explore the mode interferences we further focus on the resonant properties of dielectric disk.

To show how the Mie mode interferences can be used to achieve strong effects in the near- and far-field, we consider a Si disk with refractive index of 3.5 suspended in air with height and diameter of 220 nm and 290 nm, respectively. The disk is excited with a linearly-polarized plane wave propagating along the disk axis. Figure 4.3a shows the disk scattering cross-section spectrum. As was predicted from the Mie theory for the sphere, the MD mode scattering is stronger than that of the ED, EQ and MQ modes. We note that below 800 nm the nanodisk supports multipolar modes of a higher radial order, $s = 2, ..$, e.g. the second-order ED mode at 695 nm, see Eq. 4.4.

Non-resonant response of produced by interference of several Mie modes can be used to control the amplitude and directionality of the scattered field [12]. As shown in Fig. 4.3b, at 1125 nm the MD and ED components of the scattered field, arising due to MD and ED resonances at 1040 nm and 815 nm, respectively, have equal strengths and synchronized phases so the first Kerker condition is fulfilled [25, 182]

$$|a_1| = |b_1|, \tag{4.9}$$

$$\arg(a_1) = \arg(b_1). \tag{4.10}$$

In this regime the dipole destructive interference is balanced in the backward direction so the forward scattering directionality is increased [183]. In our examples the forward-to-backward ratio of scattered signal is 8 at 1125 nm. The suppression of the forward scattering can be achieved at the second Kerker condition [25]

$$|a_1| = |b_1|, \tag{4.11}$$

$$\arg(a_1) = -\arg(b_1). \tag{4.12}$$

In our example it is realised at 990 nm, but the effect is weak. To control the directionality of the scattered signal beyond forward and backward directions, the generalized Kerker effect can be used [184].

One more prominent non-resonant effect of Mie mode interference can be achieved by forming nonradiating configurations of polarization currents, called optical anapoles [82, 185, 186]. From the mathematical point of view, the anapole condition is achieved when one of the multipolar components of the scattered field is completely suppressed

$$a_l = 0, \quad \text{electric anapoles,} \tag{4.13}$$

$$b_l = 0, \quad \text{magnetic anapoles.} \tag{4.14}$$

This leads to dramatic suppression of the total scattered field (see Eq. 4.5) and strong enhancement of the near field. Figure 4.3c, shows the near-field distribution of the anapole configuration at 760 nm achieved for with suppressed ED contribution $a_1 = 0$. Another anapole configuration is achieved at 615 nm with suppressed EQ contribution $a_2 = 0$. By expanding the multipolar contributions into series, one can explain the nature of anapoles as destructive interference of the Cartesian electric and toroidal dipoles of comparable strength which oscillate out-of-phase [82].

4.2 Quasi-BICs: physical origin and main properties

Strong local field enhancement in dielectric nanostructures requires highly localized polarization currents. The straightforward way to localize them is excitation of high-Q resonances. As we show in this section, engineering of high-Q resonances in individual dielectric subwavelength resonators can be achieved by the resonant coupling of Mie modes which goes beyond the non-resonant interference effects (Kerker effect and dynamic anapoles) discussed in Sec. 4.1.

Individual dielectric resonators represent open electromagnetic systems with modes inherently leaking in the outer space due to finite dielectric contrast between the resonator material and the exterior. As it was shown in Sec. 2.1, in the open electromagnetic resonators BICs with infinite Q factor and zero radiative losses can be achieved by coupling of several modes in accord to the Friedrich-Wintgen mechanism. The BIC formation in such way is possible only if the number of the adjusting parameters is more than the number of the scattering channels. For compact subwavelength resonators, the number of scattering channels is infinite, and the existence of BICs in such systems is prohibited by non-existence theorem [78]. The only exception is the structures surrounded by a completely opaque shell providing decoupling of the internal resonances from the outside radiation continuum, which corresponds to perfect conducting walls or epsilon-near-zero barriers [187, 188].

As was discussed in Sec. 4.1, radiation of low-order Mie resonances of subwavelength dielectric particles is generally characterised by one dominant multipolar contribution. Presence of point symmetries of the meta-atoms allows to divide the Mie modes into groups, and within one group the modes are coupled to the same set of radiation channels. Thus, two Mie modes from the same group with complex frequencies $\omega_{A,B} - i\gamma_{A,B}$ are characterised with the same dominant radiation channel if the frequencies $\omega_{A,B}$ are close. Their interaction can be described within the two-mode approximation discussed in Sec. 2.1. We can outline the condition of suppression of of the radiation to the dominant radiation channel $\gamma^{(0)}_{A,B}$

$$\kappa(\gamma_A^{(0)} - \gamma_B^{(0)}) = \pm\sqrt{\gamma_A^{(0)}\gamma_B^{(0)}}(\omega_A - \omega_B). \tag{4.15}$$

Here, κ is the internal (near-field) interaction between the modes. Fulfilling this condition, we can achieve substantial suppression of the total radiative losses of one of the modes. The resulting mode is a quasi-BIC because it is formed in accordance with the Friedrich-Wintgen mechanism but some amount of radiation was not suppressed due to coupling to multiple radiation channels.

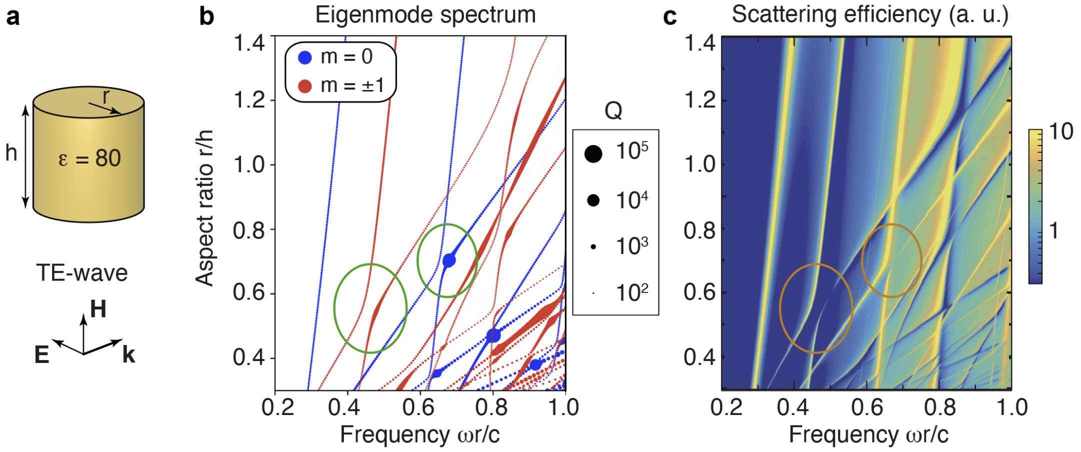

Figure 4.4: (a) Dielectric cylindrical resonator with permittivity $\varepsilon = 80$, radius r, and height h suspended in air. Schematic of the TE-polarised incident plane wave used for excitation in scattering simulations in (c). (b) The eigenmode spectrum for the modes with the azimuthal index $m = 0$ (blue dotted lines) and $m = \pm 1$ (red dotted lines), which are even with respect to up-down reflection symmetry. Dot sizes are proportional to the Q factor, the characteristic sizes are shown in the legend. (c) Dependence of the scattering efficiency on the aspect ratio of the cylinder and frequency $\omega r/c$ for the TE-polarized incident wave. The calculations are done with the step of $r/h = 0.003$. In panels (b, c), the regions of two ARCs of interest are marked by circles.

4.2.1 Eigenmode and scattering spectra. Strong coupling regime

Next, we show that formation of quasi-BICs with very high Q factors within the Friedrich–Wintgen mechanism (see Eq. 4.15) can be achieved in individual subwavelength resonators made of high-index dielectrics with simple geometries. Throughout the chapter we focus on resonators with cylindrical geometry. The cylindrical geometry combines several crucial features required for support of high-Q resonances and possible experimental realization of such resonators. In more detail, (i) cylinders possess the highest possible point symmetry except for the sphere, (ii) vertical walls make the cylindrical resonator design CMOS-compatible, (iii) mixing of radial and axial degrees of freedom makes the stationary Maxwell's equations non-integrable which allows for Mie mode mixing and interaction.

We calculate the evolution of the eigenmode spectrum of a dielectric disk resonator with respect to its aspect ratio. For calculations we consider a dielectric disk suspended in air, with radius r, height h, and permittivity of 80, as shown schematically in Fig. 4.4a. We select such high permittivity, which typically corresponds to high-index dielectric materials in microwaves, to show the pronounced peculiarities of mode spectrum. In further sections the results are generalized for wide range of dielectrics operating from visible to infrared, terahertz and gigahertz frequencies. The Mie modes of the disk form a discrete set of resonant states (see Sec. A.3.1) and are characterized by complex eigenfrequencies Ω_n. For numerical calculations we use the resonant-state expansion [189, 190], which is based on expansion of the fields of the resonant states of the cylindrical resonator $\mathbf{E}_n$ over the resonant states of a homogeneous dielectric sphere $\mathbf{E}_\alpha^{(0)}$ with the same value of permittivity, describing the cylinder.

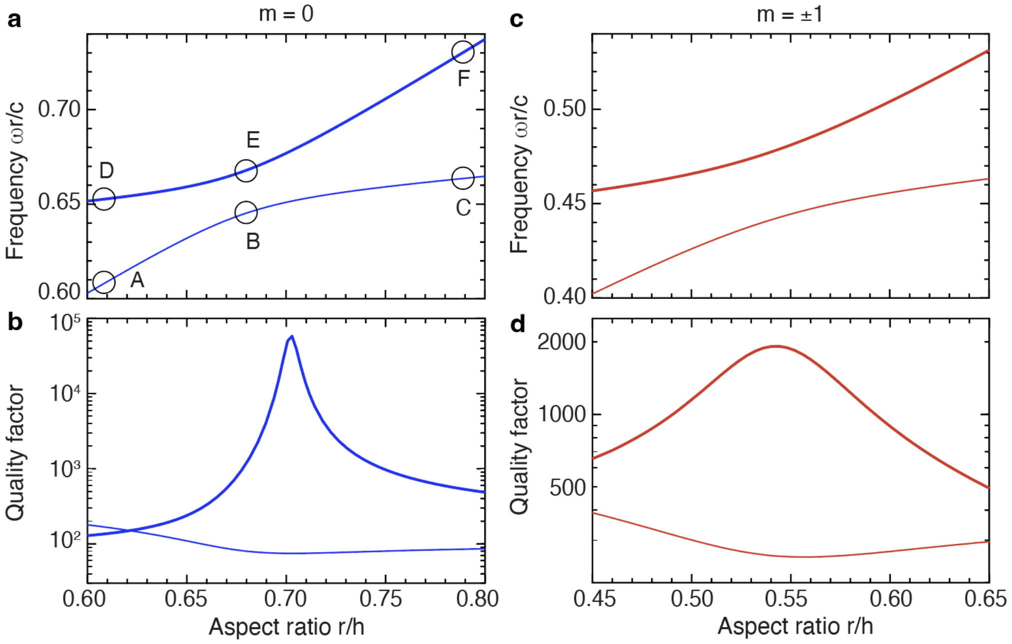

Figure 4.5: (a,b) Evolution of the resonant frequency (a) and Q factor (b) in the vicinity of ARC for coupled modes with azimuthal index $m = 0$. The labels A-F show the point where the near-field profiles are calculated (see Fig. 4.6a). (c,d) Evolution of the resonant frequency (c) and Q factor (d) in the vicinity of ARC for coupled modes with azimuthal index $m = \pm 1$.

The mode interaction in this model is described by the interaction potential $\hat{W}$ with elements

$$W_{\alpha\beta} = \frac{1}{2}\int dV\ \delta\varepsilon(\mathbf{r})\mathbf{E}_{\alpha}^{(0)} \cdot \mathbf{E}_{\beta}^{(0)}, \tag{4.16}$$

where $\delta\varepsilon(\mathbf{r})$ is a perturbation that transforms a sphere into an inscribed cylinder. The procedure is described in more detail in Sec. A.3.5. We choose the basis of resonant states of a sphere of size N in such a way that for a given orbital number l, azimuthal number m and parity we select all resonant states with frequencies Ω_n lying inside the circle $|\Omega_n R/c| < 10$, where R is the radius of the sphere that describes the cylinder. We consider $l < 80$ which results in $N = 1035$ that is enough to achieve 99.9% accuracy for calculation of real part of frequencies. Since the interaction potential $\hat{W}$ conserves the axial symmetry and up-down mirror reflection symmetry, we study problem for each azimuthal index m and each parity independently.

The dependence of the spectrum of eigenmodes with azimuthal indices $m = 0, \pm 1$, which are even with respect to up-down reflection symmetry, vs. the cylinder aspect ratio r/h is shown in Fig. 4.4b. The real part of frequencies is shown with dotted lines and dot sizes are proportional to the mode Q factor. We can clearly observe multiple ARCs between modes with the same azimuthal number. We can see that in the vicinity of each ARC point the Q factor of one of coupled modes dramatically increases. We confirm the eigenmode calculations by simulations of the scattering efficiency of the TE-polarized plane wave, propagating as shown in Fig. 4.4a. The map of the scattering efficiency for disks with different aspect ratio r/h calculated by the T-matrix method [191] is shown in Fig. 4.4c. The scattering efficiency is

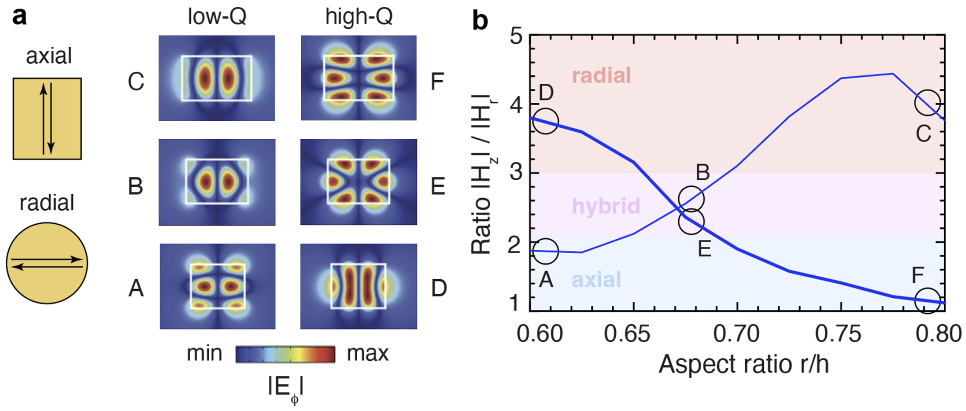

Figure 4.6: Analysis of near-field evolution for the interacting modes with $m = 0$ discussed in Fig. 4.5a,b. (a) Left: schematic of axially and radially oscillating modes of a disk resonator. Right: electric field profiles in the disk vertical cross section for high-Q and low-Q modes for r/h at point labeled with A-F in Fig. 4.5a. (b) Dependence of the ratio of the maximal value of $|H_z|$ to the maximal value of $|H_r|$ showing the transition from the radial to the axial regime of oscillations.

defined as the scattering cross section normalized on the projected geometrical cross-section of the resonator $2rh$. The scattering simulations show pronounced ARCs with narrowing of linewidth of one of the interacting modes, which confirms the results of the eigenmode simulations.

We analyse the evolution of mode resonant properties of two of the ARCs marked with open circles in Fig. 4.4b,c. Figure 4.5 shows the dependence of the resonant frequency and Q factor in the vicinity of the ARCs for modes with $m = 0$ [panels (a,b)] and with $m = \pm 1$ [panels (c,d)]. In both cases the Q factor of the high-frequency mode increases by several orders of magnitude in the vicinity of the ARC while the Q factor of the low-frequency mode drops substantially. At the point of maximal Q factor the mode is almost decoupled from the continuum of radiation waves. The observed evolution of radiation losses is in good qualitative agreement with the phenomenological results (see Fig. 2.2b). Thus, it confirms that a quasi-BIC is formed for each pair of interacting modes within the the Friedrich-Wintgen model. We note that for the $m = \pm 1$ the maximal Q factor is three orders of magnitude lower than for $m = 0$ which is due to higher order symmetry of azimuthally symmetric modes. Also, we note that the position of quasi-BIC differs slightly from the point where the strong coupling is maximal. This can be explained by finite dielectric contrast between the resonator and the surroundings - in the limit of $\varepsilon \to \infty$ these points merge, as explained below in Sec. 4.6.

4.2.2 Mode hybridization. Near-field profiles

The modes of a disk resonator can be approximately divided in two groups: radially oscillating modes, formed mainly due to reflection from a side wall, and axially oscillating modes, formed due to reflection from the faces of the cylinder, as schematically shown in the left panel of Fig. 4.6a. As can be seen from Fig. 4.4b,c modes from distinct groups demonstrate different slope of dependence of frequency on the aspect ratio. This leads to the formation of ARCs for specific values of aspect ratio in the spectrum where the modes are hybridized. We analyse the evolution of the near-field profiles of interacting modes with $m = 0$ and even parity with respect to up-down symmetry, discussed above, to explain the nature of their interaction. These modes are pure TE-modes and have three nonzero field components E_ϕ, H_z, H_r in the cylindrical reference frame [192]. Figure 4.6a shows the electric field profiles $|E_\phi|$ for high-Q and low-Q modes with $m = 0$ for the disks with $r/h = 0.61, 0.79$ away from the interaction regime and with $r/h = 0.68$ at the point of minimal distance between mode frequencies. Figure 4.6b shows the ratio of the maximal value of $|H_z|$ to the maximal value of $|H_r|$ with respect to change of r/h. From both near-field profiles and $|H_z|/|H_r|$ evolution we can see that the modes represent quasi-radially and axially oscillating resonances away from the ARC point and are hybridized strongly around $r/h = 0.68$. We note the $|E_\varphi|$ is almost constant in the vicinity of the ARC. We also note that for resonant states with $m \neq 0$ there is no exact separation into TE and TM polarized modes. The analysis shows that the interacting modes are quasi-TE and quasi-TM polarized and the degree of coupling can be calculated by evaluating the degree of pure TE (or, TM) polarization in each mode.

4.2.3 Two-mode interaction model

We describe the mode hybridization within the two-mode interaction model. We start from the resonant states of a disk with given aspect ratio with eigenfunctions $|A\rangle$ and $|B\rangle$ and study their mixing through a small change of resonator shape $\delta\varepsilon(\mathbf{r})$ playing a role of the interaction potential $\hat{V}$. The diagram of such interaction is shown schematically in Fig. 4.7a. Generally, this perturbation mixes all resonant states of the disk resonator, but as we show below in the vicinity of the ARCs it is possible to reduce the interaction to the two-mode model.

The basis modes of a disk are the eigenfunctions $|A\rangle$ and $|B\rangle$ of the Hamiltionian without interaction $\hat{H}_0$. The perturbed eigenfunction with eigenfrequency $\overline{\omega}$ represents their linear combination $|\varphi\rangle = c_\mathrm{A}|A\rangle + c_\mathrm{B}|B\rangle$, where coefficients $c_\mathrm{A,B}$ are complex. Using the eigenmode equation derived from the resonant state expansion [see Eq. (A.36)], we derive the eigenvalue equation

$$\left(\hat{H}_0 + \hat{V}\right)\begin{bmatrix} c_\mathrm{A} \\ c_\mathrm{B} \end{bmatrix} = \overline{\omega}\begin{bmatrix} c_\mathrm{A} \\ c_\mathrm{B} \end{bmatrix}, \tag{4.17}$$

with the two-mode interaction potential $\hat{V}$ given by

$$\hat{V} = \left(\begin{bmatrix} 1+W_\mathrm{AA} & W_\mathrm{AB} \\ W_\mathrm{AB} & 1+W_\mathrm{BB} \end{bmatrix}^{-1} - \begin{bmatrix} 1 & 0 \\ 0 & 1 \end{bmatrix}\right) \cdot \hat{H}_0. \tag{4.18}$$

Here, the perturbation potential $\hat{W}$ is defined as in Eq. (4.16), but instead of using the modes of a dielectric sphere as basis modes, we use the modes of the disk with given aspect ratio. Withing this model, for $|c_A| \ll |c_B|$ or $|c_A| \gg |c_B|$ the mode can be considered as dominantly radial or axial, otherwise, for $|c_A| \simeq |c_B|$ the mode becomes hybrid.

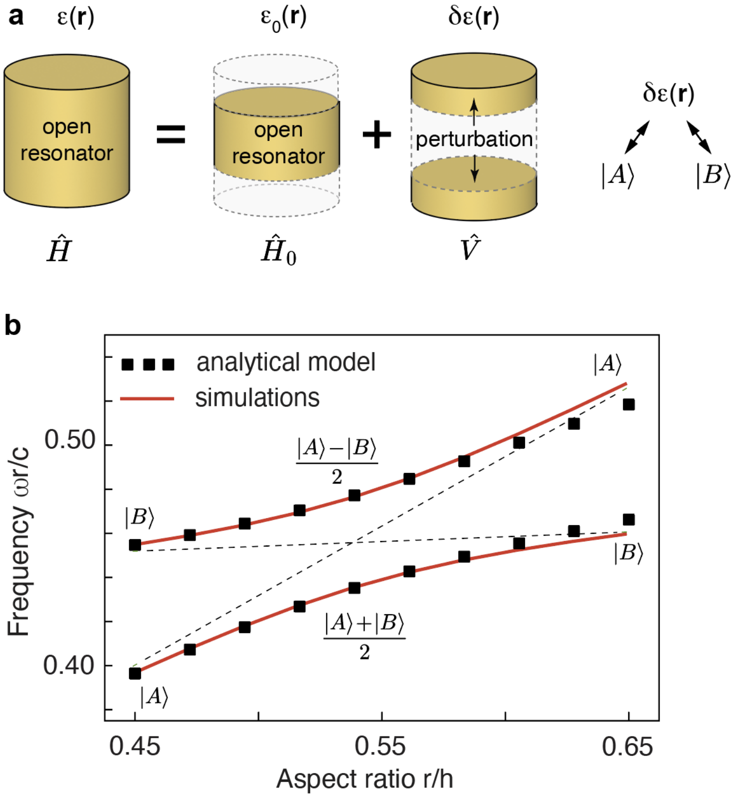

Figure 4.7: Two-mode interaction model. (a) Schematic of interaction of resonant states of the disk resonator via the perturbation $\delta\varepsilon(\mathbf{r})$ responsible for change of resonator aspect ratio. (b) Comparison of frequency dependence on r/h for the numerical model (red) and analytical two-mode interaction model (black squares) for strong coupling of modes with $m=\pm1$ analysed in Fig. 4.5c,d. The dashed lines are guide for eyes.

Figure 4.7b shows the numerical calculations of frequency spectra using the derived two-mode interaction model compared to the simulation results using the complete resonant state expansion for the modes with $m=\pm1$ and even parity with respect to up-down mirror symmetry, analysed in Fig. 4.5c,d. The model shows very good agreement with the simulation results.

4.3 Experimental observation

In this section we provide experimental results on observation of quasi-BICs in individual subwavelength disk-shaped resonators made of high-index dielectric materials in different frequency ranges.

4.3.1 Radio-frequency measurements for ceramic resonators

In the radio frequency range many ceramics possess very high permittivity and low absorption losses. For measurements, we fabricated a subwavelength ceramic disk resonator using $LaAlO_3$–$CaTiO_3$ microwave ceramics with the permittivity $\varepsilon = 44.8$ and loss tangent of

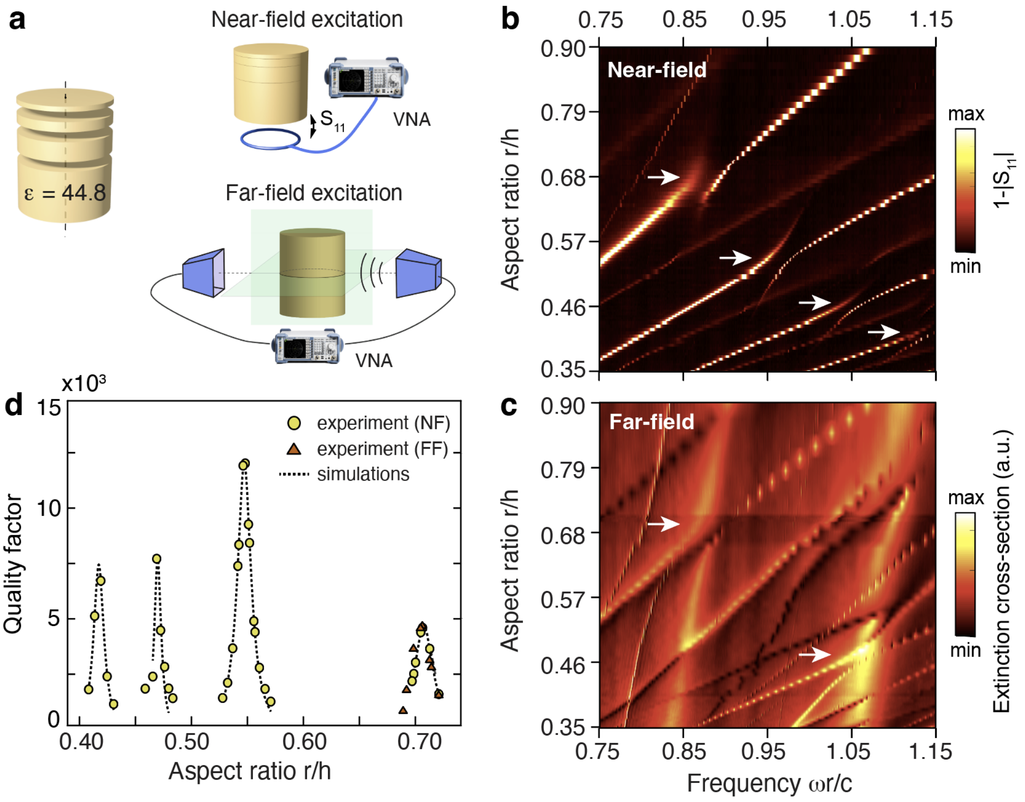

Figure 4.8: Microwave measurements of quasi-BICs in ceramic resonators. (a) The resonator consists of several ceramic disks of different height stacked in a single disk. Schematic of experimental setup for the near-field and far-fields measurements. (b) Measured map of the coefficient $1-|S_{11}|$ vs. frequency $\omega r/c$ and aspect ratio r/h. The quasi-BICs marked with white arrows correspond to $r/h = 0.71, 0.55, 0.47, 0.42$, respectively. (c) Measured map of the extinction cross-section vs. frequency $\omega r/c$ and aspect ratio r/h for TE-polarized incident wave, see excitation geometry in Fig. 4.4a. The quasi-BICs marked with white arrows correspond to $r/h = 0.71, 0.47$, respectively. (d) Dependence of unloaded Q factor on r/h for the quasi-BICs marked with arrows in panels (b,c). The data is extracted from measurements in the near-field (yellow circles) and far-field (red triangles) and calculated numerically using the RSE (dashed line).

about 10^{-4} [193]. The dielectric function of the ceramic was provided by the manufacturer and confirmed with measurements of the structure resonance frequencies. The resonator is composed of stack of the disks of different heights and the same radii $r = 15.7$ mm, shown schematically in Fig. 4.8a. By changing the number and order of disks in the sequence, we gradually change the height of the resonator and its aspect ratio. The thickness of the thinnest disk defining the height change step is 0.2 mm and the thickest disk is 15 mm. The resonator was placed on a holder made of dielectric foam with the permittivity approximately $\varepsilon = 1.1$ and low material losses at GHz frequencies.

We perform two independent set of measurements in the near-field and far-field, respectively, with excitation frequencies in the range of $1-3$ GHz. In the near-field measurements we use a loop antenna placed beneath the resonator concentrically with its axis, as shown in Fig. 4.8a. The loop antenna excites only the modes with $m = 0$. To study the scattering properties, we use the vector network analyzer (VNA) and measure the complex reflectivity via S_{11} coefficient of the scattering matrix. Figure 4.8b shows the measured dependence of $1-|S_{11}|$ on the frequency and disk aspect ratio. The map demonstrates a range of ARCs with a characteristic linewidth narrowing and quasi-BIC formation for the high-frequency mode. In the far-field measurements the resonator is positioned between two horn antennas connected to the ports of the VNA, see schematic in Fig. 4.8a. The excitation antenna radiates a TE-polarized plane wave (see Fig. 4.4a) and the collection antenna collects the field scattered in the front direction which is used to evaluate the total extinction cross-section using the optical theorem. Figure 4.8c demonstrates the measured dependence of total extinction cross-section on the frequency and disk aspect ratio. Similar to the near-field measurements, the map demonstrates a range of ARCs and quasi-BICs. From comparison of the near- and far-field maps, it can be seen that different resonances are excited for each excitation geometry. The loop antenna in the near-field excites modes with all parities but does not excite the modes with $m \neq 0$. The TE-polarized plane wave excites modes with all azimuthal numbers but it does not excite the modes with odd parity with respect to up-down mirror symmetry of the disk. In both measurements, the quasi-BICs $r/h = 0.71, 0.47$, and corresponding ARC branches can be seen.

Using the fitting procedure, the experimental unloaded Q factors of quasi-BICs at $r/h = 0.71, 0.55, 0.47, 0.42$ are extracted from data of the near- and far-field measurements. Figure 4.8d shows the extracted Q factor dependence on the aspect ratio and the comparison to the simulations done with the RSE method for $\varepsilon = 44.8$ and loss tangent of 10^{-4} (see also Fig. 4.4b). The experimental and numerical results show perfect agreement. The quasi-BIC at $r/h = 0.47$ possesses the highest Q factor of 12500 which matches perfectly with the numerical simulations. The simulations for lossless ceramics predict the maximal value of the radiative Q factor for this quasi-BIC of 1.8×10^5, but in experiment it is limited by material losses [see Eq. (2.27)].

4.3.2 Near-IR measurements for AlGaAs resonators

In the visible and near-IR ranges, many common dielectric materials, such as Si, Ge, GaAs, possess high refractive index. In the visible range the absorption losses are high towards the blue part of the spectrum, so we focus on the near-IR measurements. For the experimental observation of quasi-BICs in nanoresonators in the near-IR, we fabricated individual AlGaAs (20% Al) disks of 635 nm height placed on an engineered three-layer substrate (SiO_2/ITO/SiO_2), shown schematically in Fig. 4.9a. The structured substrate is used to increase the mode Q factor by decreasing the energy leakage into the substrate, as discussed in the next chapter in Sec. 5.2.3. The SEM image of one of the samples is shown in Fig. 4.9b. To ensure high Q factor we studied modes with azimuthal index $m = 0$ and even parity with respect to up-down mirror symmetry. We calculate the resonant wavelengths and Q factors for disks with diameters ranging from 800 to 1030 nm for the interacting radial and axial modes studied in Figs. 4.5a,b and Fig. 4.6. The structure is designed to support these modes in the near-IR range, as shown in Figs. 4.9c,d. The Q factor of the high-frequency mode reaches 190

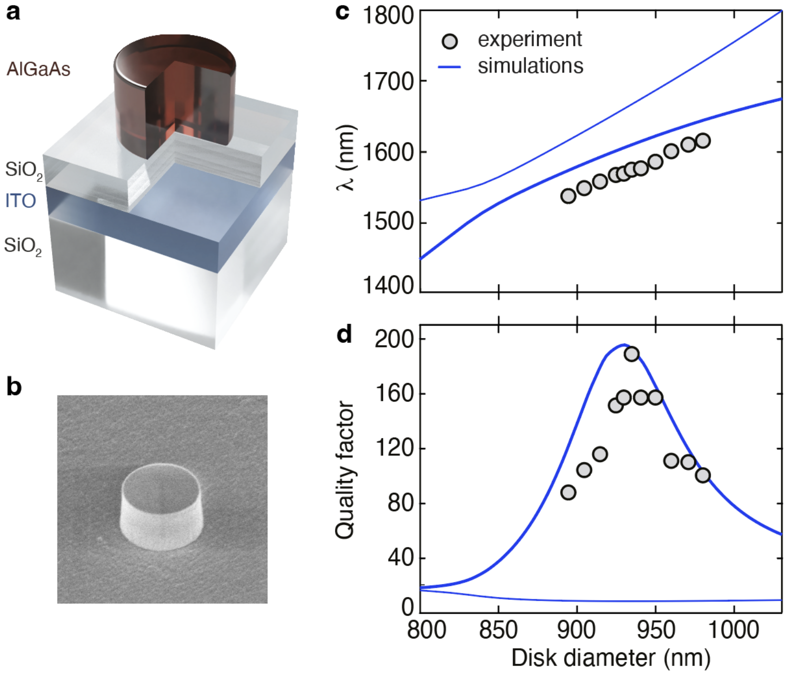

Figure 4.9: Near-IR measurements of quasi-BICs in AlGaAs resonators. (a) Schematic of an individual AlGaAs nanoresonator on top of structured substrate. (b) SEM micrograph of the fabricated sample. (c) Calculated (solid line) and measured (gray dots) wavelengths vs. resonator diameter for modes with $m = 0$, see Fig. 4.5a. (d) Calculated (solid line) and measured (gray dots) resonant wavelengths vs. resonator diameter for modes with $m = 0$, see Fig. 4.5b. The measurements are done for the high-frequency mode only.

for the disk with diameter of 930 nm and a quasi-BIC is formed.

Next, we measure the scattering spectra from the fabricated individual nanodisks with a laser tunable within 1500 − 1700 nm wavelength range. To maximize light coupling to the quasi-BIC mode, we illuminate each nanoresonator with a tightly-focused azimuthally polarized beam. The scattering spectra are evaluated as the difference between the bare substrate reflectivity and the normalized measured backward scattering of the nanoresonator. We extract the resonant mode wavelength and Q factor for the high-frequency mode using the fitting procedure and compare the measured data to the simulation results in Figs. 4.9c,d. The agreement between the experimental and numerical results is great. The measured wavelengths are blue shifted with respect to the simulated by 20 − 30 nm which can be explained by difference in AlGaAs refractive index of the sample and the one used in the model.

4.4 Multipolar behavior. Far-field evolution

In order to gain deeper insight into the physics of quasi-BICs in individual resonators, we analyse the cancellation of its radiative losses using the multipolar decomposition method [142, 181]. In this section we show that the formation of quasi-BICs in subwavelength individual resonators can be explained by suppression of the dominant multipolar contribution to the radiated power due to interaction of modes with similar far-field pattern.

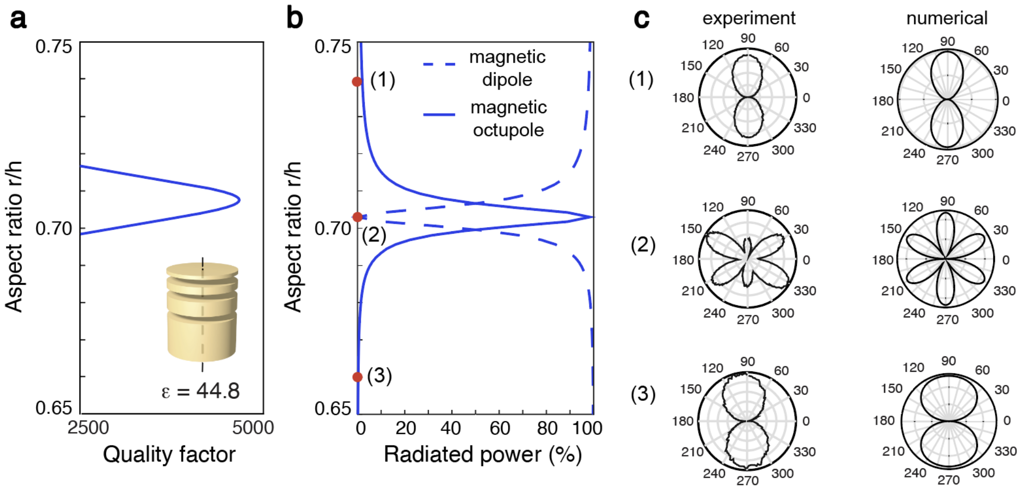

Figure 4.10: Multipolar decomposition of quasi-BIC and radiation pattern measurements. (a) The calculated Q factor dependence on the aspect ratio in the vicinity of the quasi-BIC regime for the ceramic subwavelength disk, shown in the inset. The data is taken from Fig. 4.8d. (b) Contribution of the magnetic dipole and magnetic octupole to the radiated power of the quasi-BIC depending on r/h. (c) Normalized measured and calculated far-field radiation patterns for $r/h = 0.66, 0.7025, 0.74$.

The far-field of a resonant mode could be expanded into a multipole series of vector spherical harmonics. Each harmonic plays a role of an independent radiation channel. One-to-one correspondence between eigenmodes and spherical multipoles can be established only for spherical resonators. Any mode of other resonators is always contributed by the infinite number of multipoles. However, in this infinite series it is possible to distinguish the dominant term (dominant channel) making the main contribution to the radiated power. We focus on the quasi-BIC with $m = 0$ and even parity with respect to up-down mirror symmetry observed for the ceramic disk resonator with $\varepsilon = 44.8$ at $r/h = 0.71$ in Sec. 4.3, see Fig. 4.8d. It is possible to show using the group symmetry analysis that for modes with such symmetry the main contribution to the radiation energy is given by magnetic dipole moment and the rest part of energy is radiated through higher order magnetic multipoles of odd order. The evolution of resonant properties and near-field profile for this quasi-BIC was studied in detail in Sec. 4.2, see Figs. 4.5a,b and Fig. 4.6. The Q factor dependence on the aspect ratio in the vicinity of this quasi-BIC is repeated in Fig. 4.10a. We calculate the multipolar expansion of the radiated power in the vicinity of the quasi-BIC, shown in Fig.4.10b. One can see that the magnetic dipolar contribution is suppressed strongly at the quasi-BIC regime, which can be explained by destructive interference of two magnetic dipoles with opposite directions. Due to this interaction, the high-Q mode becomes dominated by the next multipolar term which is the magnetic octupolar contribution.

Experimental verification. We perform the experimental study to demonstrate cancellation of quasi-BIC losses through the dominant radiation channel in the far-field. In the experiment, we excited the cylindrical resonator with the loop antenna placed concentrically to the axis of the cylinder. The resonator together with the loop antenna rotated around

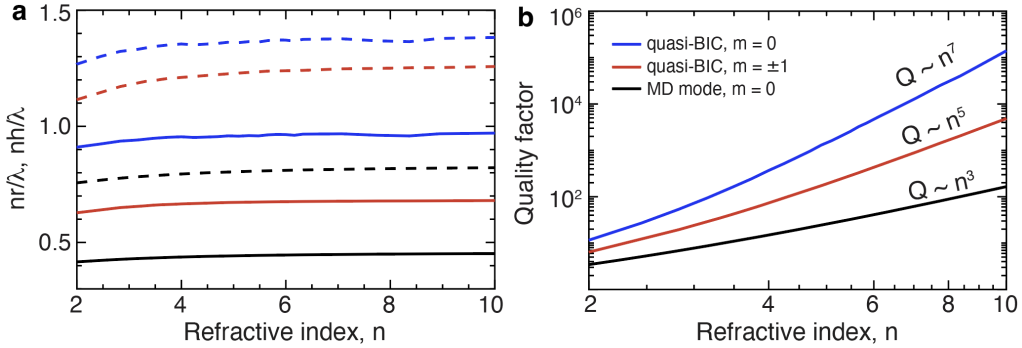

Figure 4.11: Material engineering. (a) Radius (solid line) and height (dashed line) of dielectric disk resonators with various values of refractive index n supporting magnetic dipole (MD) mode (black) with $m = 0$, quasi-BIC with $m = 0$ (blue) and quasi-BIC with $m = \pm 1$ (red). The radius and height are normalized to the resonant mode wavelength inside the material (λ/n) for each mode independently. (b) Q factor dependence on the disk resonator refractive index for MD mode and two quasi-BICs.

the transverse axis. The scattered field in the orbital plane was measured by the distantly positioned horn antenna. We measure the radiation pattern of modes for disks with $r/h = 0.66, 0.703, 0.74$ marked with numbers Fig. 4.10b. We observe that the appearance of a quasi-BIC is accompanied by a drastic change in the far-field radiation pattern from the magnetic dipolar to the magnetic octupolar one, as shown in Fig. 4.10c. The simulated far-field profiles shown in the right panel Fig. 4.10c are in perfect agreement with the experimental data. We note that numerical analysis shows that other quasi-BICs with different m and parities demonstrate similar multipolar behaviour with cancellation of the dominant multipolar term in the far-field.

4.5 Material engineering

In this section, we discuss the conditions of formation of quasi-BIC states in disk resonators made of various lossless dielectrics. For the values of refractive index from 2 to 10, we calculate the resonant wavelength and Q factor of several resonant modes using the resonant-state expansion method and evaluate the optimal aspect ratio for each mode. We focus on two quasi-BICs marked by circles in Fig. 4.4b,c for $m = 0$ and $m = 1$, respectively, which were discussed in detail for $\varepsilon = 80$ in Fig. 4.5. For comparison, we also analyse the resonant properties of the vertical magnetic dipole (MD) mode evaluated for $r/h = 0.55$; the MD mode is the lowest frequency mode in the spectra for $m = 0$ in Fig. 4.4b. Figure 4.11a demonstrates the geometrical sizes r and h of a disk resonator (normalized by the resonant wavelength inside the material λ/n) as functions of the material refractive index n for three modes of interest. One can see that the ratio nr/λ and nh/λ tends to the constant value for all three modes for $n \geq 5$. This happens because for large n the resonator becomes equivalent to a closed system. We note that for the whole range of refractive index value the resonator dimensions remain subwavelength $r < \lambda, h < \lambda$ for each of the modes. The calculated mode Q factor dependence

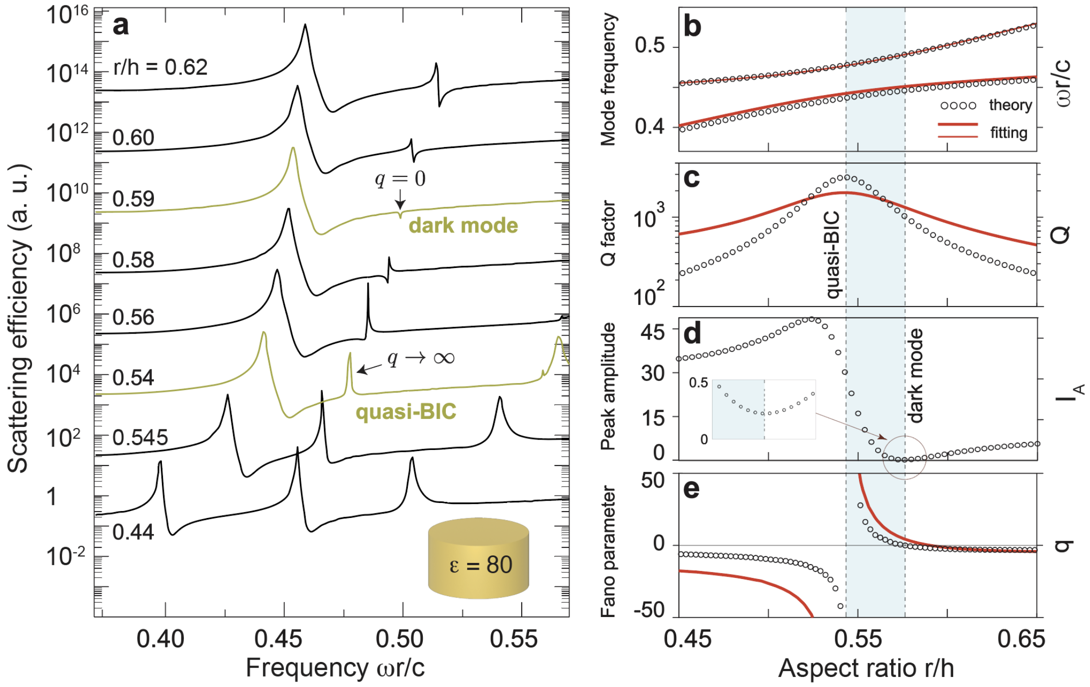

Figure 4.12: Spectral features of quasi-BIC in scattering. (a) Calculated spectra of the normalized total scattering cross-section of the cylinder resonator as a function of r/h in the region of the ARC of the modes with $m = \pm 1$ analysed in Figs. 4.5c,d. The spectra are relatively shifted by 2 orders of magnitude for clarity. (b) Peak positions $\omega r/c$ for the low- and high-frequency modes in the spectra. (c-e) Evolution of the Q factor, the peak amplitude A, and the Fano asymmetry parameter q for the high-frequency mode. In (b,c,e) the data extracted by fitting procedure is shown with red solid lines, and in (b-e) the data calculated by analytical expressions is shown with open circles.

on n is shown in Fig. 4.11b. One can see that the quasi-BICs outperform the MD mode significantly. For $n \geq 4$ the Q factor of the $m = \pm 1$ quasi-BIC becomes higher than the MD mode Q factor by more than one order of magnitude, and the Q factor of the $m = 0$ quasi-BIC - by more than two orders of magnitude. For conventional high-index dielectrics, such as Si, Ge, GaAs, used for applications in the visible and near-IR the quasi-BIC Q factor can reach more than a few hundred. For very high n the Q factor of each mode scales to the fixed power order of n, i.e. $Q \propto n^3$, $Q \propto n^5$ and $Q \propto n^7$ for the MD mode and quasi-BICs, respectively. Similar scaling of Q factor with increase of n is well-known for high-index dielectric spherical resonators [194]. From comparison to sphere modes, we conclude that the quasi-BIC with scaling $Q \propto n^5$ is a quadrupolar mode and the quasi-BIC described by $Q \propto n^7$ is the octupolar mode. This conclusion is in the good agreement with multipolar analysis of quasi-BICs and experimental results, presented in Sec. 4.4.

4.6 Spectral features in scattering

In this section we analyse the peculiarities of spectral features of quasi-BICs in scattering spectra. First, we calculate the scattering cross section for the disk with $\varepsilon = 80$ illuminated by a TE-polarized plane wave from its side for excitation frequencies in the vicinity of the ARC between two modes with $m = \pm 1$ studied in Fig. 4.4 and Figs. 4.5c,d. The excitation geometry is shown in Fig. 4.4a. The scattering cross section is normalized on the geometrical cross section $2rh$. The calculated spectra are shown in Fig. 4.12a. The low- and high-frequency modes are manifested in scattering as asymmetric features with Fano lineshape. One can see that the formation of a quasi-BIC at $r/h = 0.545$ is associated to the transformation of the lineshape to a symmetric Lorentzian. We note that for $r/h = 0.59$ a dark mode with small amplitude is formed. We fit the scattering spectra to the Fano lineshape and extract the resonant frequency and Q factor of interacting modes shown in Figs. 4.12b,c, the values coincide with the data shown in Figs. 4.5c,d. The extracted value of the Fano asymmetry parameter q is shown in Fig. 4.12e. One can see that in very close vicinity to the quasi-BIC q diverges and passes through zero at $r/h = 0.59$ which explain the formation of the dark mode.

4.6.1 Generalized Fano formula for scattering cross-section

To explain connection between peculiarities of Fano parameters and maximization of mode Q factor we derive an analytical closed-form expression for the scattering and extinction cross-section for a lossless dielectric disk resonator using the expansion into resonant states. We assume the incident field in the form of a linearly polarized plane wave with harmonic time dependence $\mathbf{E}_{\rm bg}(\omega, \mathbf{r})e^{-i\omega t}$ satisfying the Maxwell's equations of the free-space. The scattering cross-section is equal to the extinction cross-section which for the lossless case can be calculated using the optical theorem [142]. We note that the expression is simplified significantly for the case of plane wave excitation. We expand the scattered field amplitude into the sum of frequency dependent terms describing contributions of RSs of the disk resonator. Straightforward but cumbersome calculations (see Sec. A.5.2) show that $\sigma_{\rm sc}(\omega)$ can be rewritten in the form of generalized Fano formula and the Fano parameters could be expressed analytically through the material and geometrical parameters of the resonator. We note that the formula is derived from the Maxwell's equations explicitly unlike many phenomenological models used in the literature. For $\omega \simeq \omega_0$ in the vicinity of the resonant state with $\Omega_0 = \omega_0 - i\gamma_0$ we have

$$\sigma_{\rm sc}(\omega) = \frac{c^2}{\omega^2}\left[\frac{I_{\rm A}}{1+q^2}\frac{(q+\Delta\omega)^2}{1+\Delta\omega^2} + I_{\rm nr}(\omega)\right], \tag{4.19a}$$

$$I_{\rm A} = \frac{c|D_0|^2}{W_0\gamma_0}, \tag{4.19b}$$

$$q = -\cot\phi, \tag{4.19c}$$

$$\phi = \arg[D_0] + \pi(p_0 - 1)/2. \tag{4.19d}$$

Here $\Delta\omega = (\omega - \omega_0)/\gamma_0$ is the normalized relative frequency detuning, $p_0 = 0, 1$ is the mode electric field parity with respect to the inversion symmetry, q is the Fano asymmetry parameter, ϕ is the resonant phase, and $I_{\rm A}$ is the smooth amplitude of the peak and $I_{\rm nr}$ is the contribution of non-resonant scattering terms to the background offset, respectively. The key parameter of the model which determines both q and $I_{\rm A}$ is the coupling coefficient D_0 between the fields of the resonant state $\mathbf{E}_0$,$\mathbf{H}_0$ and fields of the background field

$$D_0 = -\frac{i\omega_0}{c|\mathbf{E}_{\text{bg}}|}\oint_{S_V} d\mathbf{S}\cdot\left(\mathbf{E}_0\times\mathbf{H}_{\text{bg}}(\omega_0) - \mathbf{E}_{\text{bg}}(\omega_0)\times\mathbf{H}_0\right). \tag{4.20}$$

The integration here goes over the surface S_V is the minimal convex volume including the disk resonator. In our case, it is the spherical surface describing the cylinder.

Figures 4.12b-e show the mode resonant parameters and Fano parameters calculated by using Eq. 4.19b and Eq. 4.19c. The Fano asymmetry parameter diverges at the quasi-BIC frequency which is in perfect agreement with the data extracted from full-wave simulations. We also note that the peak amplitude I_{A} reaches minimum in the dark mode regime $q = 0$. The quantitative difference between model and full-wave simulation results is due to the fundamental limitations of the resonant-state expansion method (see Appendix A.3.5) used to calculate the eigenmodes of the disk resonator for Eq. 4.19b and Eq. 4.19c, related to the contribution of the static modes to the decomposition [190].

4.6.2 Divergence of Fano asymmetry parameter

We explain the divergence of q in the vicinity of the quasi-BIC by analysing the properties of the coupling coefficient D_0. The coupling coefficient D_0 can be expanded into coupling coefficients κ_{0N} of the RS with the incoming basis modes of the free-space (see Eq. 2.11 and Eq. A.18)

$$D_0 = \sum_N d_{0N}\kappa_{0N}, \tag{4.21}$$

$$d_{0N} = \frac{\omega_0}{c|\mathbf{E}_{\text{bg}}|}s^{\text{i}}_N(\omega_0), \tag{4.22}$$

$$\kappa_{0N} = -i\oint_{S_V} d\mathbf{S}\cdot\left(\mathbf{E}_0\times\mathbf{H}^{\text{i}}_N(\omega_0) - \mathbf{E}^{\text{i}}_N(\omega_0)\times\mathbf{H}_0\right). \tag{4.23}$$

Here, s^{i}_N are the expansion coefficients of the incoming part of the background field into incoming radiation waves $\mathbf{E}^{\text{i}}_{\text{bg}} = \sum_N s^{\text{i}}_N(\omega_0)\mathbf{E}^{\text{i}}_N(\omega_0)$, $\mathbf{H}^{\text{i}}_{\text{bg}} = \sum_N s^{\text{i}}_N(\omega_0)\mathbf{H}^{\text{i}}_N(\omega_0)$. We note that the outgoing component of the background field does not contribute to the surface integral in D_0 because the resonant state has radiative nature. The electric and magnetic fields of the incoming modes of the radiation continuum $\mathbf{E}^{\text{i}}_N$, $\mathbf{H}^{\text{i}}_N$ is given by expressions in Sec. A.2.

The continuum modes can be associated with multipoles and each mode of the resonator has the dominant multipolar contribution as discussed in Sec. 4.4. Thus, we separate the contribution to the dominant radiation channel $N = 0$ and to other channels

$$D_0 = d_{00}\kappa_{00} + \sum_{N\neq 0} d_{0N}\kappa_{0N}. \tag{4.24}$$

The mode radiative losses of the quasi-BIC are low so γ_0 can be expanded over κ_{0N} and its

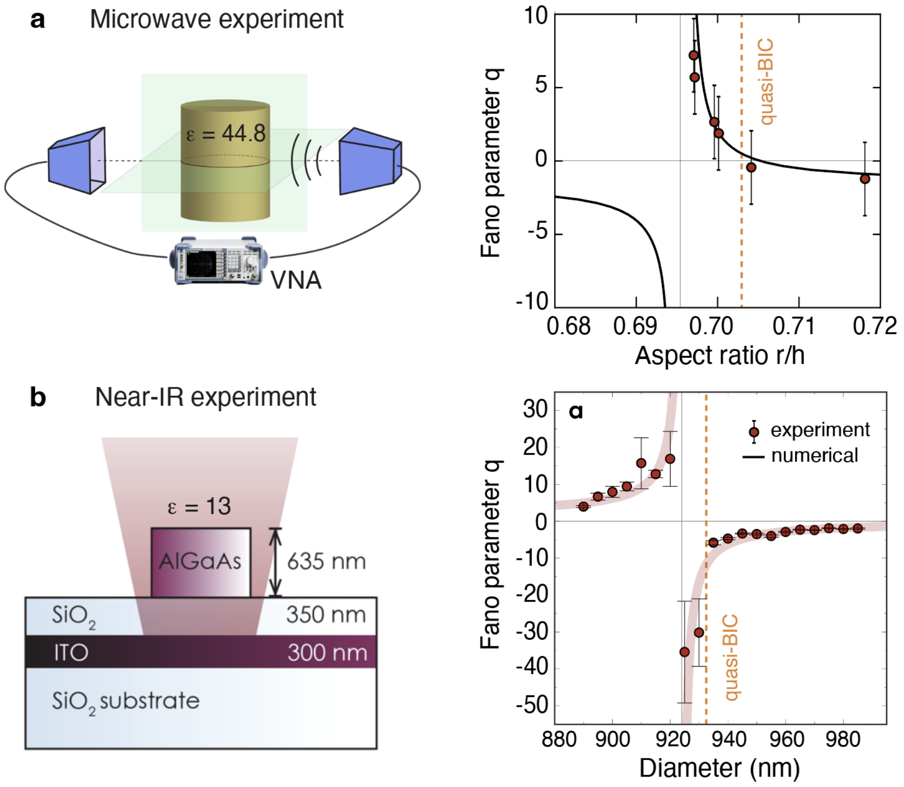

Figure 4.13: Divergence of Fano parameter in experiments. (a) Radio-frequency experiment. Left: Schematic of setup. Right: Dependence of the asymmetry parameter q on the aspect ratio for the high-Q mode. (b) Near-IR experiment. Left: Schematic of the setup. Right: Dependence of the asymmetry parameter q on the aspect ratio for the high-Q mode. The solid red line is the guide to eye. The orange dashed line in (a) and (b) is the quasi-BIC regime determined from experiment.

time-reversal transformation $\overline{\kappa}_{0N}$ as (see Sec. A.3.3)

$$\frac{2\gamma_0}{c} = \frac{\kappa^*_{00}\overline{\kappa_{00}} + \sum\limits_{N\neq 0} \kappa^*_{0N}\overline{\kappa_{0N}}}{W_0}. \tag{4.25}$$

The divergence of asymmetry parameter $q \to \infty$ for the quasi-BIC is achieved for $\mathrm{Im}(D_0) = 0$. The formation of the dark mode in spectrum $q = 0$ is achieved for $\mathrm{Re}(D_0) = 0$. This means that

$$|\kappa_{00}| = -\sum_{N\neq 0} \frac{\mathrm{Im}\left(d_{0N}\kappa_{0N}\right)}{\mathrm{Im}\left(d_{00}\exp\left(i\arg[\kappa_{00}]\right)\right)}, \qquad q \to \infty, \tag{4.26}$$

$$|\kappa_{00}| = -\sum_{N\neq 0} \frac{\mathrm{Re}\left(d_{0N}\kappa_{0N}\right)}{\mathrm{Re}\left(d_{00}\exp\left(i\arg[\kappa_{00}]\right)\right)}, \qquad q = 0. \tag{4.27}$$

At the quasi-BIC the radiation to the dominant channel is suppressed $\kappa_{00} = \overline{\kappa}_{00} = 0$, it can be also seen from Eq. 4.25. Thus, in the vicinity of the quasi-BIC, Eq. 4.26 and Eq. 4.27 is realized, because the quantity on the right part is generally small. We note that with increase of ε the regimes of quasi-BIC formation, $q \to \infty$, and $q = 0$ move closer in the parameter space because all κ_{0N} decrease but for higher-order multipole channels the decrease is faster. Ultimately, for $\varepsilon \to \infty$ the asymmetry parameter becomes undefined which corresponds to formation of the dark mode $\gamma_0 = 0$ and the so-called collapse of Fano resonance.

One can also express the resonant amplitude via the coupling coefficients

$$I_{\mathrm{A}} = 2\frac{|\sum_N d_{0N}\kappa_{0N}|^2}{\sum\limits_N \kappa^*_{0N}\overline{\kappa_{0N}}} = 4\frac{\omega_0^2}{c^2}S_0^{\mathrm{eff}}, \tag{4.28}$$

Here, S_0^{eff} is the effective aperture of the resonator, see Eq. A.51.

4.6.3 Experimental verification

We present experimental verification of divergence of Fano parameter in the vicinity of the quasi-BIC in radio-frequency and near-IR measurements. The experimental setup and resonator parameters are discussed in Sec. 4.3. Figure 4.13a shows how the Fano asymmetry parameter q depends on the aspect ratio for the high-Q mode with $m = 0$ analysed in Fig. 4.5a,b and Fig. 4.10. The data extracted from measurements confirms that $q \to \infty$ close to the quasi-BIC at $r/h = 0.7025$. Figure 4.13b demonstrates that q diverges near the quasi-BIC in the near-IR experiments. Two sets of experiments show very good agreement. Moreover, the near-IR experiment is realized for a disk on a multi-layered substrate excited with a structured beam but it still confirms the predictions of the theoretical approach developed in this section despite it assumed a free-standing disk resonator excited with a linearly polarized plane wave. This property of quasi-BIC can be used to recognize it by naked eye in the spectrum without fitting.

4.7 Summary

In summary, in this section we analysed the physics of quasi-BICs in individual subwavelength resonators made of dielectric materials. We explained formation of quasi-BICs within the Friedrich-Wintgen model which describes interaction of two modes of open resonators via the radiation continuum which leads to suppression of mode losses of one of them. We showed numerically and experimentally that conditions of the Friedrich-Wintgen model and formation of quasi-BICs can be achieved for subwavelength dielectric disks made of various dielectric materials such as AlGaAs in the visible and near-IR, and microwave ceramics with $\varepsilon > 40$ in the radio-frequency range. We showed that for microwave ceramics the experimentally measured Q factor of quasi-BIC can exceed 12500 and for AlGaAs nanodisks it is about 190. We showed that in dielectric disk resonators the quasi-BICs are realized at the avoided resonance crossing of dispersion curves of radially and axially oscillating Mie modes in the parameter space of disk aspect ratio. We showed that the mode mixing is achieved in the strong coupling regime and can be described in the two-mode interaction model. We showed numerically and experimentally that formation of the quasi-BIC is associated with suppression of losses to the dominant multipolar channel of radiation. We showed that such quasi-BICs can be realized for resonators made of dielectrics within the wide range of values of the refractive index from 2 to 10 and more. We showed that for this range of permittivities the resonator sizes remain subwavelength. We showed numerically and experimentally that formation of quasi-BICs is associated with formation of symmetric Lorentzian peak in scattering spectra. We derived an analytical closed-form expression for the scattering and extinction cross-section for a lossless dielectric disk resonator using the expansion into resonant states and showed it can be written in the form of generalized Fano formula. Using the developed theoretical approach, we showed that divergence of the Fano parameter describing the transition from an asymmetric Fano to symmetric Lorentz profile is realized in the vicinity of the quasi-BIC with the maximal Q factor.

5 Harmonic generation in individual nanoresonators supporting quasi-BICs

In Chapter 3 we analysed harmonic generation and strong nonlinear effects in resonant dielectric metasurfaces. As it was outlined, the phase matching concept widely used for bulk nonlinear crystals is not applicable for nanostructured nonlinear metasurfaces because of their subwavelength scales. For individual nanoresonators, all three dimensions are much less than the wavelength, thus the treatment of nonlinear optical processes requires development of new approaches beyond the phase matching, which are based on the expansion of the linear and nonlinear fields into contributions of resonant Mie modes. Recent studies of harmonic generation in nonlinear nanoantennas revealed that the generated signal can be enhanced in multi-resonant structures supporting a mode in the vicinity of the second-harmonic wavelength [195]. As we show in this chapter, AlGaAs disk nanoresonators are of high interest in this field because they can be engineered to support resonant modes both at the pump and harmonic wavelength. To further boost the resonant nonlinear response, we tune the pump mode to the quasi-BIC regime employing the concepts and ideas developed in Chapter 4.

In this Chapter, we investigate harmonic generation from individual dielectric nanoresonators supporting quasi-BICs and outline the criteria for maximization of conversion efficiency by optimizing the mode structure, the pump spatial and temporal profile and the environment. We focus on the second-harmonic generation process in double-resonant individual nanoresonators supporting high-Q quasi-BICs at the pump frequency and other Mie mode in the vicinity of the SH frequency. We propose a theoretical model of SHG for double-resonant nanosctructures in the regime of weak-field excitation beyond the phase matching. In the model we express the emitted SH power in the closed-form analytical expression composed of product of independent terms, describing spectral and spatial coupling efficiency of the pump to the quasi-BIC, spectral and spatial cross-coupling between the quasi-BIC and SH Mie mode, resonant enhancement at the pump and SH frequencies and outcoupling efficiency. Using the derived formula we outline a general framework of optimization of SHG efficiency by optimizing the mode structure, structuring the pump and the substrate. We prove experimentally the theoretical and numerical results and show that the measured conversion efficiency of the optimized nonlinear nanoantenna at the quasi-BIC exceeds the efficiencies of SHG reported earlier for non-BIC plasmonic and dielectric nanoantennas by more than two orders of magnitude.

Results presented in this chapter are partially included in the published References, listed below, where I am a lead author and my contribution is in theoretical aspects, eigenmode simulations, harmonic generation simulations, resonator design and experimental data analysis

(1) L. Carletti, **K. Koshelev**, C. De Angelis, and Yu. Kivshar, "Giant nonlinear response at the nanoscale driven by bound states in the continuum," Phys. Rev. Lett. **121**, 033903 (2018). DOI: 10.1103/PhysRevLett.121.033903

(2) **K. Koshelev**, A. Bogdanov, Yu. Kivshar, "Meta-optics and bound states in the continuum," Science Bulletin (special issue) **64**, 836 (2019). DOI: 10.1016/j.scib.2018.12.003

(3) **K. Koshelev**, S. Kruk, E. V. Melik-Gaykazyan, J.-H. Choi, A. Bogdanov, H.-G. Park, Yu. Kivshar, "Subwavelength dielectric resonators for nonlinear nanophotonics", Science **367**, 288-292 (2020). DOI: 10.1126/science.aaz3985

5.1 Theory of harmonic generation for double resonant nanostructures

In this section we derive the closed-form analytical expression for the power emitted from an individual nanoresonator at the SH frequency in the limit of weak-field excitation. We neglect the non-radiative and parasitic losses. The nanoresonator is subwavelength which means that the phase matching is not applicable for description of the nonlinear response. We assume that the resonator is double resonant, i.e. it supports a mode at the fundamental frequency $\omega_1 \simeq \omega$ and a mode at SH frequency $\omega_2 \simeq 2\omega$. We note that the resulting formula is derived directly from the Maxwell's equations contrary to commonly used phenomenological approaches.

For simplicity, in the derivation we consider a free-standing resonator, while the further comparison with the experimental results shows that the theory can be used to analyse the SH response of resonators on substrate. The resonator is excited by the pump with a given distribution of electric field $\mathbf{E}_{\mathrm{bg}}$. The scattered field can be rigorously expanded into contributions of RSs with $\Omega_n = \omega_n - i\gamma_n$. We consider the case when only one mode $\mathbf{E}_1$ is resonantly excited in the vicinity of the pump frequency

$$\mathbf{E}_{\mathrm{sc}}(\omega, \mathbf{r}) = a_1(\omega)\frac{\mathbf{E}_1(\mathbf{r})}{N_1}. \tag{5.1}$$

The normalization constant N_1 is close to the mode energy W_1 (see Eq. A.23) for high-Q modes. The resonant amplitude a_1 for $\omega \simeq \omega_1$ is given by (see Appendix A.4 and Eq. A.41)

$$a_1(\omega) = (-i)\frac{c}{\left(\omega - \omega_1 + i\gamma_1\right)}\oint_{S_V} d\mathbf{S}\cdot\left(\mathbf{E}_1 \times \mathbf{H}_{\mathrm{bg}}(\omega_1) - \mathbf{E}_{\mathrm{bg}}(\omega_1)\times \mathbf{H}_1\right). \tag{5.2}$$

Here, the surface integration goes over the sphere describing the resonator S_V.

The SH polarization $\mathbf{P}^{\mathrm{NL}}$ is given by

$$P_i^{\mathrm{NL}}(2\omega,\mathbf{r}) = \sum_{j,k} \chi^{(2)}_{ijk} E_j(\omega,\mathbf{r}) E_k(\omega,\mathbf{r}), \tag{5.3}$$

where $\chi^{(2)}_{ijk}$ is the second-order susceptibility tensor. The total field at the fundamental frequency $\mathbf{E}(\omega)$ is dominated by the resonant term $\omega \simeq \omega_1$

$$P_i^{\mathrm{NL}}(2\omega) = [a_1(\omega)]^2 \sum_{j,k} \chi^{(2)}_{ijk} E_{1,j}(\mathbf{r}) E_{1,k}(\mathbf{r}). \tag{5.4}$$

The induced field $\mathbf{E}(2\omega)$ at the SH frequency can be found via the Lippmann-Schwinger equation using the resonator Green's function $\hat{\mathbf{G}}$

$$\mathbf{E}(2\omega,\mathbf{r}) = -\frac{(2\omega)^2}{c^2} \int d\mathbf{r}' \hat{\mathbf{G}}(2\omega,\mathbf{r},\mathbf{r}') \cdot \mathbf{P}^{\mathrm{NL}}(2\omega,\mathbf{r}'). \tag{5.5}$$

We assume that $\mathbf{E}(2\omega)$ is dominated by a single resonant state $\mathbf{E}_2$ with frequency ω_2 lying in the vicinity of 2ω

$$\mathbf{E}(2\omega,\mathbf{r}) = a_2(2\omega)\frac{\mathbf{E}_2(\mathbf{r})}{W_2}. \tag{5.6}$$

Here, we assume that the SH mode is high-Q, so $W_2 = |N_2|$. The amplitude a_2 can be found as

$$a_2(2\omega) = -\frac{2\omega[a_1(\omega)]^2}{(2\omega-\omega_2+i\gamma_2)} \sum_{i,j,k} \chi^{(2)}_{ijk} \int d\mathbf{r}\, E_{2,i}(\mathbf{r}) E_{1,j}(\mathbf{r}) E_{1,k}(\mathbf{r}). \tag{5.7}$$

The total SH power $P(2\omega)$ is

$$P(2\omega) = \frac{c}{8\pi} \oint_{S_V} d\mathbf{S} \cdot \mathrm{Re}[\mathbf{E}(2\omega) \times \mathbf{H}^*(2\omega)]. \tag{5.8}$$

Here, the integral is evaluated at the surface of sphere describing the resonator.

Combining the expressions for a_1 and a_2, we get the expression for the total SH power

$$P(2\omega) = \alpha(\omega)\varkappa_2 Q_2 L_2(2\omega)\varkappa_{12}[Q_1 L_1(\omega)\varkappa_1 P(\omega)]^2. \tag{5.9}$$

Here, the spectral overlap factor $L_j(\omega)$ function is defined as

$$L_j(\omega) = \frac{\gamma_j^2}{(\omega-\omega_j)^2+\gamma_j^2}, \tag{5.10}$$

the spatial coupling coefficient $\varkappa_1$ is (see Appendix A.3.3)

$$\varkappa_1 = \frac{\left|\oint_{S_V} d\mathbf{S} \cdot \left(\mathbf{E}_1 \times \mathbf{H}_{\mathrm{bg}}(\omega_1) - \mathbf{E}_{\mathrm{bg}}(\omega_1) \times \mathbf{H}_1\right)\right|^2}{\oint\limits_{S_V} d\mathbf{S} \cdot \left(\mathbf{E}_1 \times \mathbf{H}_1^* + \mathbf{E}_1^* \times \mathbf{H}_1\right) \int d\mathbf{S} \cdot \mathrm{Re}[\mathbf{E}_{\mathrm{bg}} \times \mathbf{H}_{\mathrm{bg}}^*]}, \tag{5.11}$$

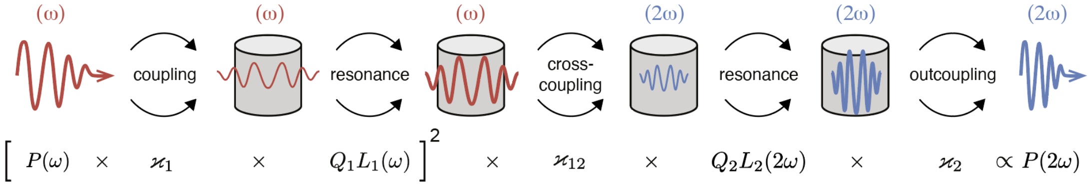

Figure 5.1: Schematic of resonant SHG process in a double-resonant dielectric nanoantenna. Each term of the formula describes one step of the process.

the spatial cross-coupling coefficient $\varkappa_{12}$ is

$$\varkappa_{12} = \frac{\left|\sum_{i,j,k} \chi^{(2)}_{ijk} \int d\mathbf{r}\, E_{2,i}(\mathbf{r}) E_{1,j}(\mathbf{r}) E_{1,k}(\mathbf{r})\right|^2}{(W_2\omega_2/c)(W_1\omega_1/c)^2}, \tag{5.12}$$

the outoupling coefficient $\varkappa_2 = W_2/|N_2|$ tends to the unity for $Q_2 \gg 1$,

$$\varkappa_2 = 1, \tag{5.13}$$

the smooth envelope coefficient α is

$$\alpha(\omega) = 256\frac{8\pi}{c}\left[\frac{\omega}{c}\right]^2, \tag{5.14}$$

and the total incident power $P(\omega)$ is

$$P(\omega) = \frac{c}{8\pi}\int d\mathbf{S}\cdot \mathrm{Re}[\mathbf{E}_{\mathrm{bg}}(\omega) \times \mathbf{H}^*_{\mathrm{bg}}(\omega)]. \tag{5.15}$$

Here, the integration goes over the plane perpendicular to the beam propagation direction.

We note, that the effective mode volume does not appear in Eq. (5.9). The reason is that the effective mode volume approach is used to approximate a mode with some nontrivial spatial distribution as a mode with uniform pattern which takes the effective mode volume. Here, we use the explicit expressions for the mode overlap integrals [see Eq. (5.12)], which take into account the actual spatial distribution of the mode electric fields.

Figure 5.1a illustrates SH generation process for double resonant nanostructures described with Eq. 5.8 with a step-by-step schematic. A part of the incident power $\varkappa_1 P(\omega)$ is coupled to the mode at the pump frequency, and the coupling efficiency is determined by the spatial overlap between the pump and the mode fields. The coupled power is resonantly enhanced by the factor determined by the Q factor Q_1 of the mode at the pump frequency and damped by the spectral mismatch factor $L_1(\omega)$. The efficiency of up-conversion of the total accumulated power is determined by the cross-coupling coefficient $\varkappa_{12}$ which depends on the symmetry of the nonlinear susceptibility tensor of AlGaAs and the spatial overlap between the generated nonlinear polarization current and SH mode. The converted SH power is increased to the extent of Q factor of the second-harmonic mode Q_2 but at the same time is decreased due to the spectral mismatch factor $L_2(2\omega)$. The outcoupling factor $\varkappa_2$ determines the efficiency of radiation of the SH mode and tends to unity for high-Q modes $Q_2 \gg 1$.

5.2 Optimization of second-harmonic generation efficiency

In this section we provide a general framework describing how to achieve maximal second-harmonic generation efficiency for individual dielectric nanostructures in the resonant regime. We describe optimization of the SH response via engineering of the mode structure, structuring of the pump and substrate. As an example, we focus on AlGaAs (20% Al) nanodisks supporting the quasi-BIC with azimuthally symmetric field distribution in the near-IR discussed in Sec. 4.3. The height of nanodisks is 635 nm and diameter varies in the range from 890 nm to 990 nm. The structure is placed on an engineered three-layer substrate (SiO_2/ITO/SiO_2). The quasi-BIC is realized for the disk diameter of 930 nm with the resonant wavelength $2\pi c/\omega_1 = 1600$ nm and Q factor $Q_1 = 190$. The quasi-BIC lifetime is $\tau_1 = 1/(2\gamma_1) = 160$ fs. As we discuss below the designed structure supports a high-order Mie mode with complex frequency $\omega_2 - i\gamma_2$ at the SH wavelengths $750-850$ nm. The mode Q factor is about $Q_2 = 60$ and the spatial symmetry of the fields is characterized by the azimuthal index $|m| = 2$.

We consider excitation of the nanodisk with focused non-chirped pulse with FWHM duration of τ_p centered at the excitation frequency ω_p. We assume the pulse is a cylindrical vector beam with non-trivial spatial distribution of electric and magnetic fields. The time-averaged SH power $P(2\omega_p)$ depends on the dynamics of the resonant amplitude at the excitation frequency

$$P(2\omega_p) \propto \int dt |a_1(t)|^4 = \iiint d\overline{\omega} d\omega' d\tilde{\omega} a_1^*(\overline{\omega}) a_1^*(\omega') a_1(\tilde{\omega}) a_1(\overline{\omega} + \omega' - \tilde{\omega}). \tag{5.16}$$

Here, we assumed that $\tau_2 \ll \tau_1$ and $\tau_2 \ll \tau_p$ so only the time dependence of a_1 determines the SH power. Due to the effect of finite pulse duration, the expression for the SH power in Eq. (5.9) transforms in the following form at $\omega_p = \omega_1$

$$\frac{P(2\omega_1)}{P^2(\omega_1)} \propto \overbrace{\underbrace{\varkappa_p \varkappa_1^2}_{\text{coupling}}}^{\text{pump engineering}} \times \overbrace{\underbrace{\varkappa_2}_{\text{outcoupling}} \times \underbrace{L_2(2\omega_1)\varkappa_{12}}_{\text{cross-coupling}} \times \underbrace{Q_2 Q_1^2}_{\text{enhancement}}}^{\text{mode engineering}}. \tag{5.17}$$

Here, $\varkappa_p$ is the nonlinear spectral coupling coefficient that depends on the ratio of τ_p and τ_1 and is analysed below.

One can see that the harmonic generation efficiency in Eq. 5.17 depends on efficiency of pump coupling, resonant enhancement, mode cross-coupling and outcoupling. Below we discuss how to increase each of these coefficients by engineering the mode structure and pump spatial and spectral properties.

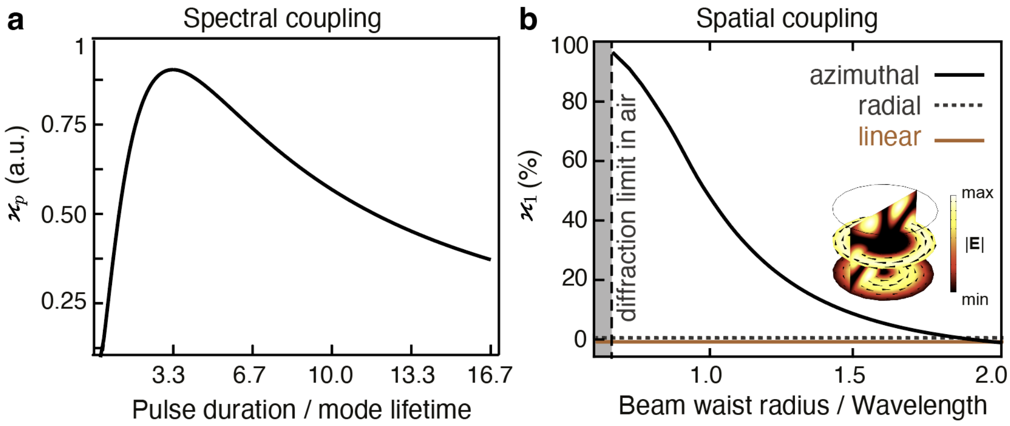

Figure 5.2: Pump engineering. (a) Dependence of the nonlinear spectral coupling coefficient $\varkappa_p$ on the ratio τ_p/τ_1. (b) Percentage of the pump power coupled to the quasi-BIC for different polarizations of pump depending on the ratio between the beam waist radius and the pump wavelength. The calculation is done for a free-standing nanoresonator in air. The diffraction limit is 0.61. The inset shows the near-field profile of the quasi-BIC.

5.2.1 Pump engineering

Spectral coupling. Equation 5.16 shows that the time-averaged second-harmonic power is determined by nonlinear spectral coupling coefficient $\varkappa_p$ which can be evaluated as

$$\varkappa_p(\tau_p,\tau_1)=\iiint d(\Delta\overline{\omega})d(\Delta\omega')d(\Delta\tilde{\omega})\ \xi^*(\Delta\overline{\omega})\xi^*(\Delta\omega')\xi(\Delta\tilde{\omega})\xi(\Delta\overline{\omega}+\Delta\omega'-\Delta\tilde{\omega}), \tag{5.18}$$

$$\xi(\Delta\omega)=s_p(\Delta\omega)l_1(\Delta\omega), \tag{5.19}$$

$$s_p(\Delta\omega)=\sqrt{\tau_p}e^{-\Delta\omega^2\tau_p^2/(8\ln 2)}, \tag{5.20}$$

$$l_1(\Delta\omega)=\frac{\gamma_1}{\Delta\omega+i\gamma_1}. \tag{5.21}$$

Here, $|s_p|^2$ determines the spectral density of the pump intensity and the Lorentzian term $|l_1|^2=L_1$ accounts for the resonant response of the quasi-BIC. Here, we assume that the pulse is characterized with the Gaussian spectral shape.

Figure 5.2a shows calculated dependence of $\varkappa_p$ on the pulse duration, normalized on τ_1, for the fixed pump power. The coupling coefficient is maximized for the specific ratio between pulse duration and mode lifetime is

$$\tau_p=3.3\tau_1. \tag{5.22}$$

This results coincides with the results predicted for time-varying cavities excited with chirped pulses [196]. For the quasi-BIC of interest this estimation gives $\tau_p=0.5$ ps.

Spatial coupling. The spatial coupling between the pump and the quasi-BIC is determined by $\varkappa_1$ which depends in the overlap of their electric and magnetic fields. One can see that to maximize $\varkappa_1$ the pump spatial structure needs to match the symmetry of the quasi-BIC fields. The quasi-BIC is characterized by azimuthal symmetry $m=0$ (see inset in Fig. 5.2b), thus the pump needs to be structured with azimuthal symmetry. By expanding the pump fields into the basis of radiation waves of the free-space, we re-write the coupling coefficient as (see Appendix A.4)

$$\varkappa_1 = \frac{|\sum_N \kappa_{1N} s_N^{\mathrm{i}}|^2}{\sum_N |\kappa_{1N}|^2 \int d\mathbf{S} \cdot \mathrm{Re}[\mathbf{E}_{\mathrm{bg}} \times \mathbf{H}^*_{\mathrm{bg}}]}. \tag{5.23}$$

Here, κ_{1N} is the coupling coefficient between the mode and the incoming radiation wave N, and s_N^{i} are the expansion coefficients of the incoming component of the background field into the incoming radiation waves. We assume N includes only the modes with $m = 0$, so $\overline{\kappa_{1N}} = \kappa_{1N}$. Considering the mode radiation is dominated by channel $N = 0$, we can write

$$\varkappa_1 \propto \left(\sum_{N,N'} \delta_{N,N'} \left(s_N^{\mathrm{i}}\right)^* s_{N'}^{\mathrm{i}} \right), \tag{5.24}$$

$$\delta_{N,N'} = \frac{\kappa^*_{1N} \kappa_{1N'}}{|\kappa^2_{1,0}|}. \tag{5.25}$$

The function $\delta_{N,N'}$ has a very pronounced maximum at $N = N' = 0$, thus $\varkappa_1$ is maximized if the pump is coupled mostly to the same radiation channel as the mode, i.e. $|s_0^{\mathrm{i}}| \gg |s_N^{\mathrm{i}}|$ for $N \neq 0$.

The excitation beam is a focused cylindrical vector beam characterized by its beam waist. Since the quasi-BIC radiation is dominated by magnetic octupolar radiation channel, the beam needs to be focused tightly in order to achieve high-order harmonics in its spatial structure. Tight focusing can be achieved in the non-paraxial regime when the beam waist radius becomes comparable to the mode wavelength. Figure 5.2b shows calculated dependence of the spatial coupling efficiency $\varkappa_1$ on the ratio between the beam waist radius and the pump wavelength. The simulation results for the azimuthally polarized pump confirm the qualitative estimation and show that the highest coupling efficiency is achieved for the beam waist radius smaller than the wavelength. The coupling efficiency for the radially and linearly polarized pumps are equal to zero.

For the experimental conditions, discussed further, the spatial coupling is $\varkappa_1 \simeq 0.33$.

5.2.2 Mode engineering

Spatial cross-coupling. The SH power is proportional to the spatial cross-coupling coefficient $\varkappa_{12}$ depending on the symmetry of $\hat{\chi}^{(2)}$. The structure of $\hat{\chi}^{(2)}$ determines the selection rules for SHG in double-resonant structures [197], i.e. the induced nonlinear currents excite only the modes that are spatially matched to the nonlinear polarization, which spatial distribution is determined by the quasi-BIC near-field profile (see Eq. 5.4).

The nanodisk is made of AlGaAs with the symmetry of the zincblende crystalline structure,

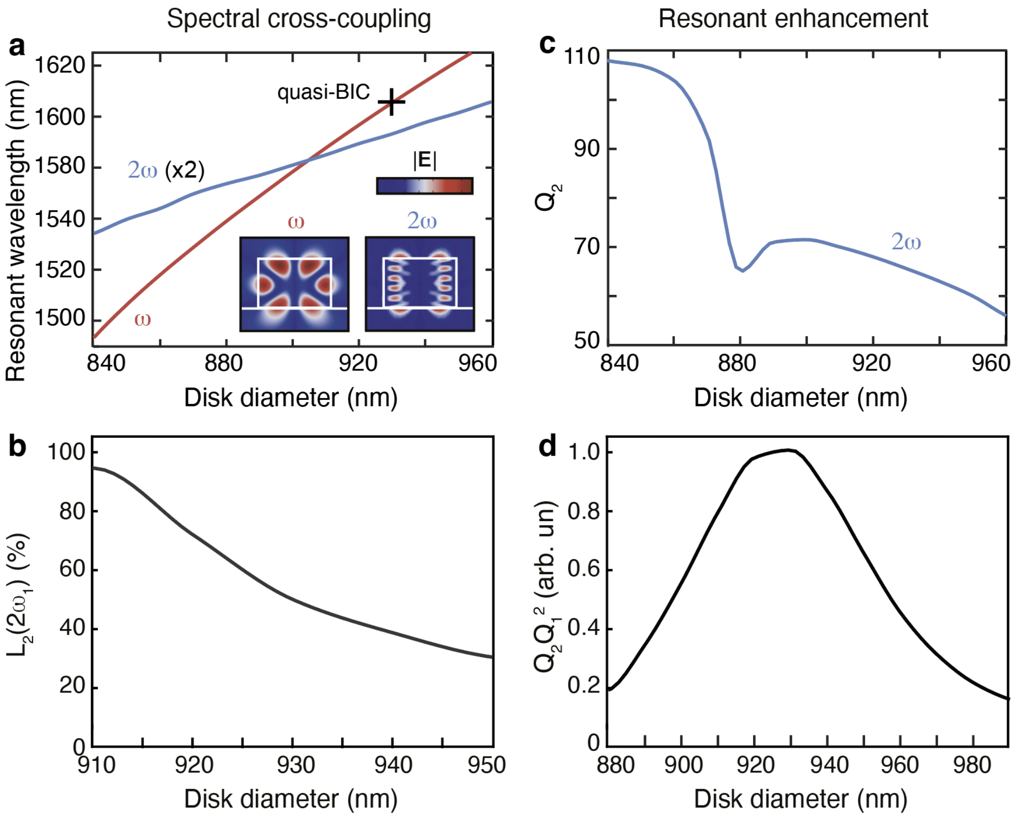

Figure 5.3: Mode engineering. (a) Dispersion of the high-Q mode at the pump wavelength (red) and the mode at the second harmonic wavelength (blue) vs. disk diameter. The wavelength of the SH mode is doubled for a direct comparison. The inset shows the near-field profiles of both the modes. (b) Spectral overlap $L_2(2\omega_1)$ between the high-Q mode at the pump frequency and the high-order Mie mode at the SH frequency vs. the disk diameter. (c) Q factor evolution for the mode at the second harmonic wavelength vs. disk diameter. (d) Dependence of the resonant enhancement factor $Q_2Q_1^2$ on the disk diameter.

so $\varkappa_{12}$ can be simplified to

$$\varkappa_{12} \propto \left(\chi^{(2)}_{zxy}\right)^2 \left| \int d\mathbf{r}\, E_{2,z} E^2_{1,\varphi} \sin(2\varphi) \right|^2 . \tag{5.26}$$

The quasi-BIC is azimuthally symmetric with the only nonzero field component $E_{1,\varphi}$ in the spherical reference frame. Thus, x- and y- field components will depend on the azimuthal angle as $\cos\varphi$ and $\sin\varphi$. This means only the SH modes with $|m| = 2$ will give nonzero contribution to $\varkappa_{12}$.

Numerical calculations show that $\varkappa_{12} \simeq 10^{-8}\left(\chi^{(2)}_{zxy}\right)^2$.

Spectral cross-coupling. The designed structure supports a range of modes at the SH wavelengths 750—850 nm, but only one of the modes is characterized with $|m| = 2$ azimuthal symmetry. Figure 5.3a shows the calculated resonant wavelength of the SH mode and quasi-BIC depending on the disk diameter. The structure is exactly double-resonant $\omega_2 = 2\omega_1$ for the diameter of 915 nm, while in the quasi-BIC regime the dispersion curves are close. Quantitatively, the contribution of the spectral mismatch to the SH power is governed by the cross-coupling coefficient $L_2(2\omega_1)$

$$L_2(2\omega_1) = \frac{\gamma_2^2}{(2\omega_1 - \omega_2)^2 + \gamma_2^2}. \tag{5.27}$$

Figure 5.3b shows the calculated dependence of the spectral mismatch on the disk diameter. One can see that at the quasi-BIC regime the coupling efficiency reaches $L_2(2\omega_1) = 0.5$. The SH mode has magnetic hexadecapolar nature with orbital index $l = 4$. The near-field of the SH mode is shown in the inset of Fig. 5.3a.

Resonant enhancement. The resonant enhancement of the SH power is determined by the mode Q factors Q_1 and Q_2. Figure 5.3c shows the calculated dependence of Q_2 on the disk diameter. The SH mode Q factor has weak dependence on the disk diameter. In the quasi-BIC regime it reaches $Q_2 = 65$. Figure 5.3d shows the calculated dependence of resonant enhancement factor $Q_2 Q_1^2$ on the disk diameter. One can see that it is dominated by quasi-BIC response because Q_1 has pronounced dependence on the disk diameter (see Fig. 4.9d) and its contribution is squared due to nonlinearity.

Outcoupling. The outcoupling coefficient $\varkappa_2 = 1$ for the free-standing nanoresonator. For the structure on a substrate $\varkappa_2$ describes the collection efficiency and is determined by the geometry of the collection setup. More specific, it depends on the direction the SH power collection and the NA of the collection objective. Assuming the SH power is collected in one direction on the surface S, we can write the outcoupling coefficient as

$$\varkappa_2 = \frac{\int_S d\mathbf{S} \cdot \mathrm{Re}\left[\mathbf{E}_2 \times \mathbf{H}_2^*\right]}{\oint_{S_V} d\mathbf{S} \cdot \mathrm{Re}\left[\mathbf{E}_2 \times \mathbf{H}_2^*\right]}. \tag{5.28}$$

In the collection aperture is small, $\varkappa_2$ can be increased by improving the directionality of the SH mode in the collection direction [198]. We note that for collection of the SH power in the transmission geometry, the substrate needs to be transparent at SH wavelengths.

5.2.3 Substrate engineering

For optical experiments, the resonator is usually fabricated on a substrate which causes additional radiation losses due to a higher refractive index than that for air. To compensate the decrease of the Q factor induced by energy leakage, we insert a reflective layer in the substrate [199]. The schematic of design is shown in Fig. 5.4a. The reflective layer is represented by a layer of ITO exhibiting an epsilon-near-zero transition acting as a conductor above 1200 nm wavelength (i.e. at the quasi-BIC wavelength), and as an insulator below this wavelength (i.e. at the SH mode wavelength), see Fig. 5.4b. The thickness of ITO layer is 300 nm to prevent radiation from transmission through it. The ITO layer is separated from the res-

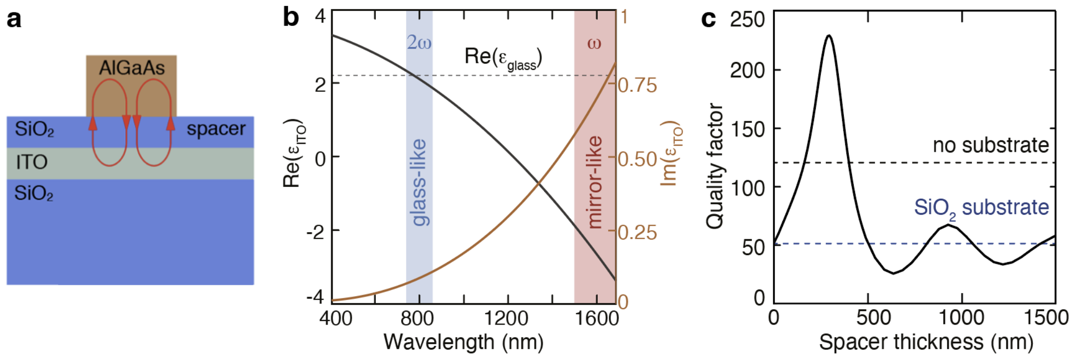

Figure 5.4: Substrate engineering. (a) Schematic of an AlGaAs nanodisk on a structured three-layer substrate (SiO_2/ITO/SiO_2). (b) Experimental ellipsometry data for the permittivity of the ITO layer. Wavelength ranges of the excitation and collection are marked with the red and blue shadings, respectively. (c) Calculated Q factor of the quasi-BIC vs. SiO_2 spacer thickness compared to the Q factors of a nanoresonator in air and on a bulk SiO_2 substrate (dashed lines).

onator by a SiO_2 spacer. As shown in Fig. 5.4c, the thickness of the SiO_2 spacer layer provides control over the phase of reflection, increasing the Q factor. One can see that for the optimal spacer thickness between 300 and 400 nm, the Q factor reaches the maximal predicted value of 235. This value is two times larger than for the free-standing AlGaAs disk and more than four times larger than for the same disk on a bulk SiO_2 substrate. Engineering substrate to be transparent at the SH wavelength allows for collection of the SH power in the transmission geometry.

5.3 Experimental observation of second-harmonic generation

In this section we provide experimental results on observation of SH generation from AlGaAs disk nanoresonators tuned to the quasi-BIC regime. For nonlinear experiments we use the samples fabricated for linear measurements, described in Sec. 4.3. Each sample is an individual AlGaAs (20% Al) nanodisk with 635 nm height and diameter varying in the range from 890 nm to 990 nm. The nanodisks are placed on an engineered three-layer substrate (SiO_2/ITO/SiO_2) with 300 nm SiO_2 spacer and 350 nm ITO layer. The quasi-BIC with the resonant wavelength 1570 nm and Q factor of order of 190 is realized for the disk with 930 nm diameter (see Sec. 4.3). The quasi-BIC lifetime is $\tau_1 = 1/(2\gamma_1) = 160$ fs.

We perform experimental analysis of the SHG enhancement in the fabricated quasi-BIC resonators. We excite the fabricated set of nanoparticles with laser pulses with 2 ps duration in the wavelength range from 1500 to 1700 nm. To pump the structures, we use the structured light in the form of a tighly focused cylindrical vector beam with azimuthal polarization [200]. The beam waist radius is measured using the knife-edge method and is equal to 1800 nm. We measure the SH signal in the forward and backward direction. Figure 5.5a shows the maps of the SHG intensity vs. the pump wavelength and resonator diameter. The experimental data reveal a sharp enhancement of the nonlinear signal in the quasi-BIC regime. We did

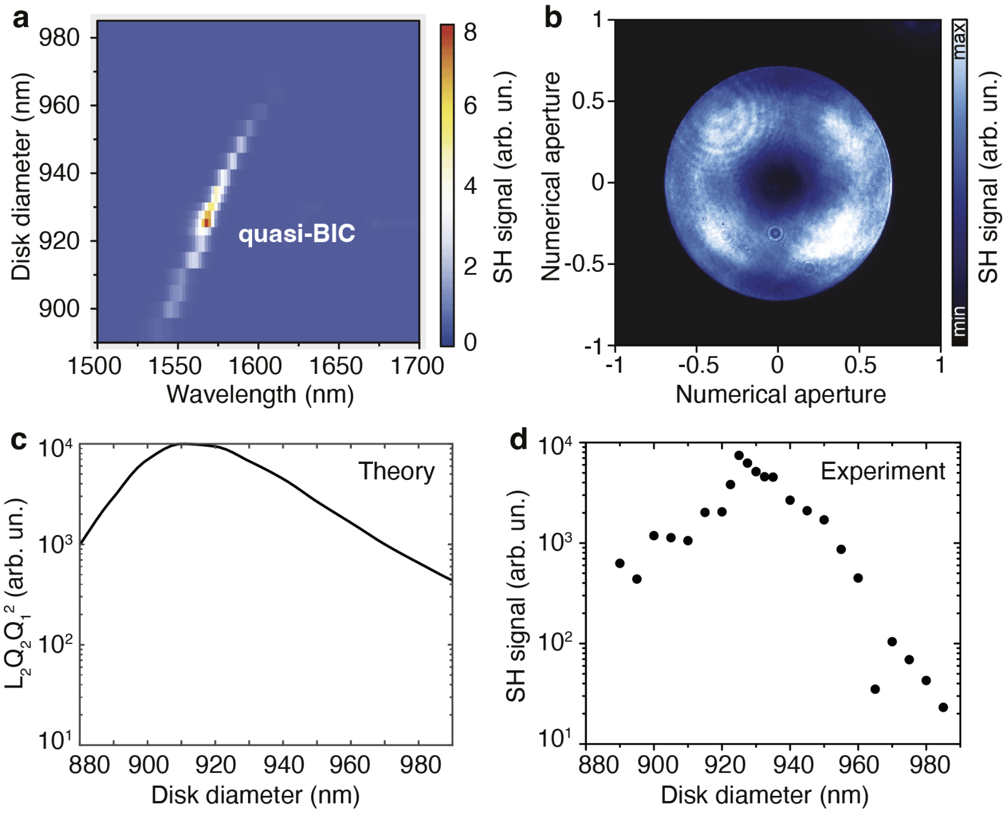

Figure 5.5: Observation of SH generation from AlGaAs disk nanoresonators tuned to the quasi-BIC regime. (a) Map of the SH intensity measured as a function of the pump wavelength and disk diameter for the azimuthally polarized pump. (b) Experimentally measured directionality diagram of SH signal for a disk with a diameter of 930 nm in the backward forward direction. (c) The enhancement factor $L_2(2\omega_1)Q_2Q_1^2$ dependence on the disk diameter. (d) The measured SH signal evaluated along the quasi-BIC dispersion. The data in (c) and (d) is normalised independently.

additional experiments pumping nanodisks with cylindrical vector beams of linear and radial polarization. For these pump polarizations the SH spectra do not show any sharp features around the quasi-BIC wavelength. Next, we measure the directionality diagram of the SH signal in backward direction within the numerical aperture of a pair of confocal objective lenses, shown in Fig 5.5b. The diagram in the backward direction features distinct maxima in four directions which are qualitatively similar to the far-field pattern of the mode excited at the SH wavelength with the azimuthal index $|m| = 2$, as it was discussed in Sec. 5.2. Next, we measure the SHG conversion efficiency at the quasi-BIC wavelength. For the peak pump power of 7.2 W, the directly measured peak SH power is 0.06 mW which gives the value of the conversion efficiency of 1.2×10^{-6} W^{-1}. The measured SHG efficiency is more than two orders of magnitude higher than that the efficiencies achieved for nonlinear plasmonic and dielectric antennas earlier [37, 39, 57, 195].

Finally, we compare the evolution of the SH signal in the resonant regime with increase of the disk diameter with the predictions of the model described in Sec. 5.2. The spectral coupling coefficient $\varkappa_p = 0.5$ for $\tau_p = 2$ ps and $\tau_1 = 160$ fs. The spatial coupling coefficient is

0.33 for the beam waist radius of 1800 nm. Figure 5.5c shows the dependence of the resonant enhancement multiplied by the spectral cross-coupling coefficient $L_2(\omega_1)Q_2Q_1^2$ on the disk diameter evaluated at the frequency of the high-Q mode (quasi-BIC branch), see Fig. 4.9c. The other parameters, including the spatial cross-coupling coefficient $\varkappa_{12}$ and the outcoupling efficiency $\varkappa_2$ have weak dependence on the disk diameter and are omitted in the model. Figure 5.5d shows the evolution of the measured SH signal evaluated along the quasi-BIC dispersion. The simulated and measured data is in good agreement. The mismatch for the high values of the disk diameter is because the objective collection efficiency and the dependence of other coefficients on the disk diameter were neglected. The numerical estimation of the SHG efficiency for the experimental conditions using the formulas Eq. 5.9 and 5.17 gives 10^{-5} W^{-1}. This value is in a good agreement with the experimental value of 1.2×10^{-6} W^{-1}.

5.4 Summary

In summary, in this chapter we analysed the second-harmonic generation process from double-resonant individual nanoresonators supporting high-Q quasi-BICs at the pump frequency and other Mie mode in the vicinity of the SH frequency. We developed a theoretical model for double-resonant nanosctructures in the regime of weak-field excitation beyond the phase matching. We expressed the emitted SH power in the form of product of independent terms, describing spectral and spatial coupling efficiency of the pump to the quasi-BIC, spectral and spatial cross-coupling between the quasi-BIC and SH Mie mode, resonant enhancement at the pump and SH frequencies and outcoupling efficiency. We derived closed-form analytical expressions for each term. We provided a general framework of optimization of SHG efficiency by optimizing the mode structure, structuring the pump and the substrate. We showed that pump structured to match the field profile of the quasi-BIC allows to enhance the coupling efficiency of energy to tens of percent for tightly focused vector beams. We showed that engineering substrate with a reflective layer positioned at specific distance from the resonator can increase the quasi-BIC Q factor by two times compared to a free-standing case.We applied the developed model to describe the SHG from an AlGaAs nanodisk resonator on a structured substrate supporting a quasi-BIC in the near-IR range and excited with an azimuthally polarized vector beam. We showed good agreement of the simulations and model results with the experimental measurements. The measured conversion efficiency at the quasi-BIC exceeded the efficiencies of SHG reported earlier for non-BIC plasmonic and dielectric nanoantennas by more than two orders of magnitude.

6 Conclusion and outlook

In this thesis, we investigated the fundamental physical properties of optical quasi-BICs in dielectric metasurfaces and individual subwavelength meta-atoms and explored their practical feasibility for strong light confinement and the resonant enhancement of optical nonlinearities. Using these findings, we established novel concepts and approaches for efficient light trapping in resonant dielectric nanostructures, specifically, for nonlinear applications, as summarized below.

In Chapters 2 and 3 we developed a new approach to confine electromagnetic radiation efficiently in dielectric metasurfaces with broken in-plane symmetry and demonstrated theoretically and experimentally the high performance of these structures as nonlinear metasurfaces. Figure 6.1 summarizes the main ideas and results of the thesis presented in these Chapters.

Firstly, we generalized the results of numerous earlier studies reporting on sharp resonances in asymmetric plasmonic and dielectric metasurfaces which resonant response can be controlled somehow with the change of asymmetry. We showed that all observed effects independently on how they were called (sharp Fano resonances, electromagnetically induced transparency, dark modes, trapped resonances) originate from the resonant effects described by the fundamental physics of symmetry-protected optical BICs in periodic photonic structures. With the knowledge of symmetry-protected BIC nature of these resonances, we used the concept of quasi-BICs to explain why and how the Q factor determining the sharpness of the peaks changes with the asymmetry.

Secondly, we, for the first time to the best of our knowledge, explored the importance of parasitic losses originating due to fabrication imperfections in realistic metasurfaces on the value of the field enhancement. We showed that for maximal field enhancement the optimal coupling condition needs to be satisfied with the rate of parasitic losses equal to the rate of pure radiative losses. Therefore, we extended the concept of optimal (critical) coupling to the effects of parasitic losses, while previously it was known only for absorptive structures. We used these findings to propose the general procedure of designing a planar dielectric metasurface for strong local field enhancement with resonant properties *on demand*. The developed procedure is based on the engineering of quasi-BICs for a selected application and includes (i) the geometric scaling of the metasurface as a whole to tune the quasi-BIC resonant wavelength; (ii) the determination of the parasitic losses of the practical metasurface; (iii) the tuning of the asymmetry of meta-atoms to adjust the radiative Q factor of the quasi-BIC to

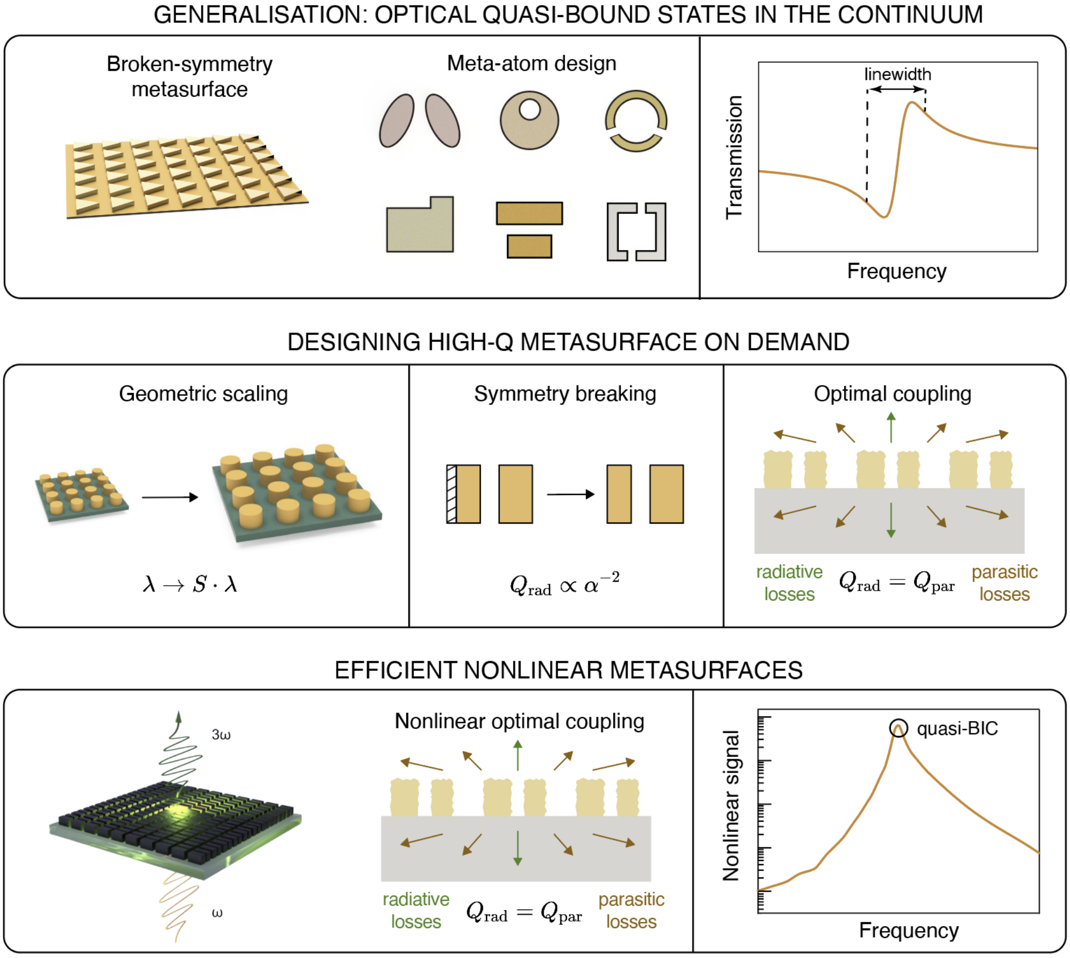

Figure 6.1: Summary of results on quasi-BICs in broken-symmetry metasurfaces, presented in Chapters 2 and 3.

the measured parasitic Q factor.

Thirdly, we extended the developed optimal coupling concept for nonlinear metasurfaces with quasi-BICs and showed that harmonic generation efficiency in the undepleted pump approximation can be maximized when the rates of radiative and parasitic losses are equal. We used this concept to design one universal nonlinear Si metasurface which was re-scaled and fabricated for five different experiments on harmonic generation and the observation of self-action effects in different frequency ranges. For low intensity excitation, we showed experimentally that the optimized Si metasurfaces with quasi-BICs can generate efficient THG for the near-IR excitation and THG, 5HG for the mid-IR excitation. We also showed experimentally that SHG from monolayers of transition metal dichalcogenides integrated with optimized Si metasurfaces with quasi-BICs can be enhanced by more than three orders of magnitude. For strong field excitation, we showed experimentally that optimized Si metasurfaces with quasi-BICs can generate from the third to the eleventh odd harmonics for the mid-IR pump. We showed experimentally self-action effects in these metasurfaces for the near- and mid-IR pump and developed analytical model to explain these effects in the terms of photoionization of Si enhanced by sharp resonances.

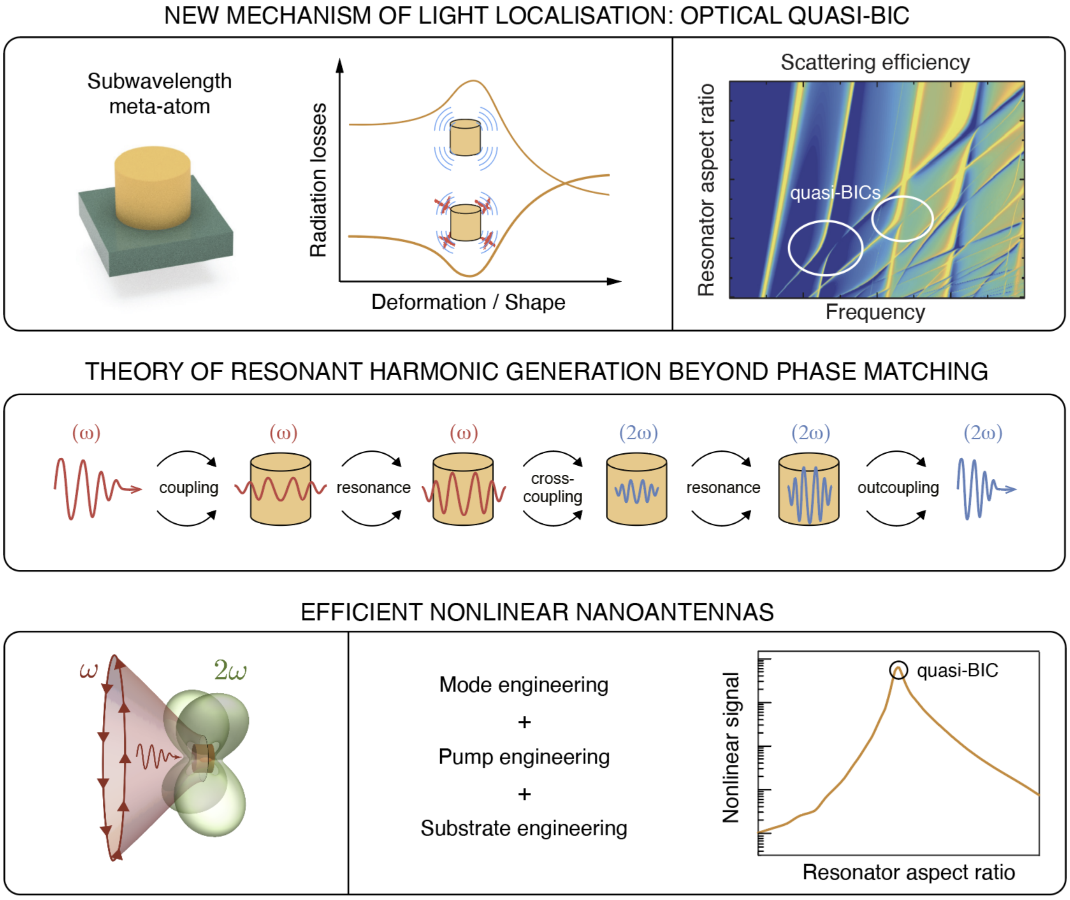

Figure 6.2: Summary of results on quasi-BICs in individual subwavelength meta-atoms, presented in Chapters 4 and 5.

In Chapters 4 and 5 we proposed the new concept of quasi-BICs in individual subwavelength dielectric meta-atoms and showed theoretically and experimentally that it can be used for efficient light trapping and harmonic generation in nonlinear nanoantennas. Figure 6.2 summarizes the main ideas and results of the thesis presented in these Chapters.

Firstly, we suggested the new concept of light localization in individual subwavelength dielectric meta-atoms by the formation of quasi-BICs with a large Q factor. We, for the first time to the best of our knowledge, demonstrated that the quasi-BIC regime can be achieved for fully subwavelength compact electromagnetic resonators without the use of materials with extreme parameters, such as epsilon-near-zero or perfect electric conductor layers. We studied the mechanism of quasi-BIC formation, their near- and far-field properties, and explained their connection to the scattering features. In more detail, we explained the formation of quasi-BICs in the framework of the interaction of two strongly coupled Mie resonances at the point of the avoided crossing of their dispersion branches via the radiation continuum. We showed that the regime of the suppression of radiation losses can be achieved in subwavelength dielectric resonators with simple geometries, such as cylinder-shaped particles, by tuning their aspect ratio which induces mode interaction for the specific values of geometrical parameters. We demonstrated that the quasi-BICs can realized for any low-loss dielectric

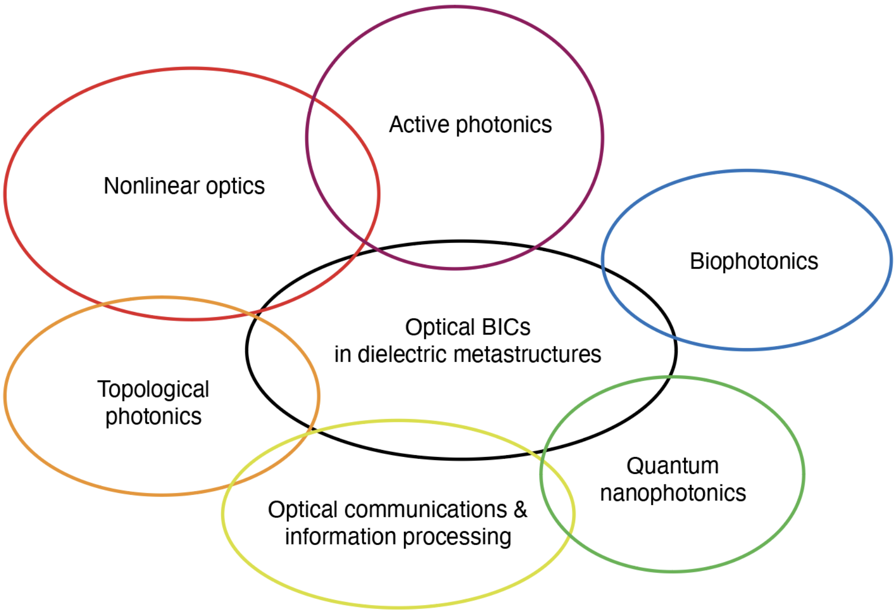

Figure 6.3: The frontiers of nanophotonics that can potentially benefit from using resonant dielectric metastructures supporting optical quasi-BICs.

particles with the refractive index more than 2 in various spectral ranges from the visible to microwaves. For a dielectric disk-shaped resonator, we showed that the quasi-BIC is formed by mixing of radially and axially polarized Mie modes with identical multipolar structure of the radiation and the dominant multipolar component of the far-field is suppressed because of this interaction. We demonstrated that in the scattering spectra the quasi-BICs are manifested as symmetric Lorentzian peaks and away from the quasi-BIC regime the profile of the resonant feature transforms to the asymmetric Fano shape. With this finding, we outlined the connection between the maximization of the mode Q factor and the peculiarities of the scattering spectra. We verified the developed analytical models and results of numerical simulations in the proof-of-principle experiments in the near-IR and radiofrequency range.

Secondly, we developed the theoretical framework for the description of harmonic generation process and the calculation of its efficiency in subwavelength nonlinear nanoresonators operating beyond the phase matching. In the model, we characterized the harmonic signal intensity using the expansion of the linear and nonlinear fields into the contributions of resonant Mie modes. More specifically, we studied SHG from double-resonant nanoresonators made of nonlinear crystals without an inversion symmetry that support Mie modes in the vicinity of the pump and second-harmonic wavelength. We expressed the emitted power in the form of an analytical expression composed of the product of independent terms, describing spectral and spatial coupling efficiency of the pump to the Mie mode at the pump frequency, spectral and spatial cross-coupling between the pump Mie mode and harmonic Mie mode, resonant enhancement at the pump and SH frequencies, and outcoupling efficiency. For each term, we derived the closed form expression using the theory of Green's function expansion into quasi-normal modes for open electromagnetic systems.

Thirdly, we showed that the conversion efficiency in nanoantennas with strong second-order nonlinearities can be maximized by the excitation of high-Q quasi-BIC resonances and the consequent engineering of the resonator mode structure, the spatial and temporal profile of the pump, and the substrate properties. We fabricated nonlinear AlGaAs nanoantennas with optimized properties and demonstrated experimentally a record-high SHG efficiency at the quasi-BIC wavelength that exceeds the SH conversion efficiencies reported earlier for compact plasmonic and dielectric nanoantennas by more than two orders of magnitude.

The topics covered in this thesis can be extended to a few immediate and long term research directions. As an outlook, we anticipate that planar and compact dielectric metastructures operating at sharp quasi-BIC resonances with tunable properties may find versatile applications in many frontier areas of the modern nanophotonics, illustrated in Fig. 6.3. They include but not limited to nonlinear optics, active photonics, optical communications and information processing, quantum nanophotonics, biophotonics, and active photonics.

Appendix

A.1 Methods. Numerical simulations and data analysis

A.1.1 Eigenmode and scattering spectra

For numerical simulations of the transmission,reflection and scattering spectra, we use the finite-element-method solver in COMSOL Multiphysics in the frequency domain. The near-field distributions and eigenmode spectra are simulated using the eigenmode solver in COMSOL Multiphysics. The material properties, including absorption losses, are extracted from the ellipsometry data or imported from the tabulated data, as specified in the text.

Metasurfaces. All calculations were realized for a metasurface placed on a semi-infinite substrate surrounded by a perfectly matched layer mimicking an infinite region. The simulation area is the unit cell extended to an infinite metasurface by using the Bloch boundary conditions. The incident field is a plane wave in the normal excitation geometry, the polarization is defined in the text.

Individual resonators. All calculations are realized for a single resonator (free-standing or on a semi-infinite substrate) surrounded by a perfectly matched layer mimicking an infinite region.

A.1.2 Multipolar decomposition

For quantitative characterization of the disk eigenmodes, we employ the mode decomposition method over the irreducible spherical multipoles [181], characterized by the orbital ($l = 1, 2, \ldots$) and azimuthal ($m = 0, \pm 1, \ldots, \pm |l|$) indices defined with respect to the disk axis. The decomposition is realized as a custom built-in routine for the eigenmode solver in COMSOL Multiphysics. For multipole classification, we use the following notations: electric/magnetic dipole (ED/MD, $l = 1$), electric/magnetic quadrupole (EQ/MQ, $l = 2$), electric/magnetic octupole (EO/MO, $l = 3$). The multipolar decomposition for eigenmodes of open resonators is approximate due to divergence of field amplitudes in the far-field zone. Despite that, it still gives good quantitative results for the modes with a Q factor more than 10.

A.1.3 Harmonic generation

For numerical simulations of the nonlinear response at the harmonic frequency, we employ the approach based on the undepleted pump approximation [156] which is justified for the pump powers below the saturation threshold of the resonator. We use two steps to calculate the intensity of the radiated nonlinear signal. Using the simulated field amplitudes at the pump wavelength, we obtain the nonlinear polarization induced inside the resonator. Then, we employ the polarization as a source for the electromagnetic simulation at the harmonic wavelength to obtain the generated harmonic field.

Si Metasurfaces. For TH generation in Si the nonlinear susceptibility function $\chi^{(3)}_{\mathrm{Si}}$ was considered as a tensor corresponding to the cubic crystallographic point group with $\chi^{(3)}_{\mathrm{xxxx}} = 2.45 \times 10^{-19}$ m^2/V^2. For nonlinear simulations we take into account the parasitic losses Q_{par} which are simulated manually by adding of artificial absorption losses via extinction $k = n/2Q_{\mathrm{par}}$, where n is the refractive index and Q_{par} is extracted from the linear scattering data. We note that for the nonlinear enhancement the effect of absorption losses is equivalent to the effect of parasitic ones, as can be seen from Eq. 3.10, while in the linear spectra the shape of resonant features depends on the exact mechanism of losses.

AlGaAs nanodisk resonators. The nonlinear susceptibility tensor corresponds to the zincblende crystalline structure with $\chi^{(2)}_{xyz} = 290$ pm/V [156].

A.1.4 Extraction of data. Fitting procedure.

The resonant parameters (frequency, linewidth, Fano asymmetry parameter) are extracted from the simulated and experimental scattering spectra using the single-peak fitting to the generalized Fano lineshape implemented into Python programming language via the Levenberg–Marquardt algorithm with custom multi-step re-evaluation of initial conditions and extraction of resonance related data from the background. The error is directly extracted from the fitting procedure.

A.2 Modes of the radiation continuum

In this section we summarize some properties of the modes of the radiation continuum (free-space) in spherical and Cartesian coordinates. The free-space modes form a discrete set of basis functions $\mathbf{E}_N$ and $\mathbf{H}_N$ for a fixed frequency ω that satisfy

$$\begin{aligned} \nabla \times \mathbf{E}_N &= ik\mathbf{H}_N, \\ \nabla \times \mathbf{H}_N &= -ik\mathbf{E}_N. \end{aligned} \tag{A.1}$$

Here, $k = \omega/c$ is the wavevector in air surrounding the photonic structure, and N labels the radiation channels.

We normalize the basis functions using integral relation between outgoing and incoming waves [201]

$$i \oint_{S_V} d\mathbf{S} \cdot \left(\mathbf{E}^{\mathrm{i}}_{N} \times \mathbf{H}^{\mathrm{o}}_{N'} - \mathbf{E}^{\mathrm{o}}_{N'} \times \mathbf{H}^{\mathrm{i}}_{N}\right) = \delta_{NN'}. \tag{A.2}$$

where S_V is the surface enclosing the minimal convex volume V.

Spherical basis. In spherical basis, the outgoing and incoming functions are vector spherical waves. The radiation channel N is labeled by l, m and s- or p-polarization. Their fields are given by [201]

$$\begin{aligned}
\mathbf{E}^{\mathrm{o,i}}_{s,lm}(\mathbf{r}) &= N_l \frac{\xi^{\mathrm{o,i}}_l(kr)}{r\sqrt{l(l+1)}} \boldsymbol{\Phi}_{lm}(\hat{\mathbf{r}}), \\
\mathbf{H}^{\mathrm{o,i}}_{s,lm}(\mathbf{r}) &= i \frac{N_l}{r\sqrt{l(l+1)}} \left[\frac{l(l+1)\xi^{\mathrm{o,i}}_l(kr)}{kr} \boldsymbol{Y}_{lm}(\hat{\mathbf{r}}) + \left(\xi^{\mathrm{o,i}}_l\right)'(kr) \boldsymbol{\Psi}_{lm}(\hat{\mathbf{r}}) \right], \\
\mathbf{E}^{\mathrm{o,i}}_{p,lm}(\mathbf{r}) &= -\frac{N_l}{r\sqrt{l(l+1)}} \left[\frac{l(l+1)\xi^{\mathrm{o,i}}_l(kr)}{kr} \boldsymbol{Y}_{lm}(\hat{\mathbf{r}}) + \left(\xi^{\mathrm{o,i}}_l\right)'(kr) \boldsymbol{\Psi}_{lm}(\hat{\mathbf{r}}) \right], \\
\mathbf{H}^{\mathrm{o,i}}_{p,lm}(\mathbf{r}) &= -iN_l \frac{\xi^{\mathrm{o,i}}_l(kr)}{r\sqrt{l(l+1)}} \boldsymbol{\Phi}_{lm}(\hat{\mathbf{r}}).
\end{aligned} \tag{A.3}$$

Here, $\xi^{\mathrm{o,i}}_l(z) = z h^{(1),(2)}_l(z)$ is the outgoing (incoming) Riccati-Bessel function, and $\boldsymbol{\Phi}_{lm}$, $\boldsymbol{Y}_{lm}$, $\boldsymbol{\Psi}_{lm}$ are vector spherical harmonics

$$\boldsymbol{Y}_{lm} = \hat{\mathbf{e}}_r Y_{lm}, \quad \boldsymbol{\Psi}_{lm} = r\nabla Y_{lm}, \quad \boldsymbol{\Phi}_{lm} = \mathbf{r} \times \nabla Y_{lm}, \tag{A.4}$$

where Y_{lm} are scalar orthonormal spherical harmonics with dependence of φ in the form of $\exp(im\varphi)$.

Using Eq. (A.2), the normalization constant can be expressed as

$$N_l^{-2} = 2i\,\mathrm{Re}\left[i\xi^{\mathrm{o}}_l \left(\xi^{\mathrm{i}}_l\right)'\right]_{r=R}, \tag{A.5}$$

where R is the radius of the spherical resonator with volume V. For real k the normalization constant is simplified to $N_l = 1/\sqrt{2i}$. For real k the orthogonality condition for radiation waves can be simplified to

$$\oint_{S_V} d\mathbf{S} \cdot \left[\mathbf{E}^{\mathrm{o}}_{\tau,l,m} \times (\mathbf{H}^{\mathrm{o}}_{\tau',l',m'})^* + (\mathbf{E}^{\mathrm{o}}_{\tau',l',m'})^* \times \mathbf{H}^{\mathrm{o}}_{\tau,l,m}\right] = (-1)^m \delta_{\tau,\tau'} \delta_{l,l'} \delta_{m,-m'}. \tag{A.6}$$

Here, $\tau = s, p$. This correspondence also holds for complex k-vectors with small imaginary part, e.g. at the resonant frequencies of high-Q modes.

Basis of diffraction modes. For periodic photonic structures, the basis functions are propagating and evanescent plane waves. The surface S_V represents the top and bottom surfaces of the unit cell, while the integral in periodic directions vanishes. The radiation channel N is labeled by top and bottom indices, and s- or p-polarization. We are interested in the sub-diffractive regime and the resonant properties at the Γ point of the reciprocal space, so the waves carrying energy are the plane waves propagating along the surface normal [201]

$$
\begin{aligned}
\mathbf{E}_s^{\mathrm{i},\pm}(\mathbf{r}) &= \sqrt{\frac{i}{2S_0}}\mathrm{e}^{\pm ikz}\begin{pmatrix}0\\1\\0\end{pmatrix}H_\theta(\pm z),\\
\mathbf{H}_s^{\mathrm{i},\pm}(\mathbf{r}) &= \sqrt{\frac{i}{2S_0}}\mathrm{e}^{\pm ikz}\begin{pmatrix}\mp1\\0\\0\end{pmatrix}H_\theta(\pm z),\\
\mathbf{E}_p^{\mathrm{i},\pm}(\mathbf{r}) &= \sqrt{\frac{i}{2S_0}}\mathrm{e}^{\pm ikz}\begin{pmatrix}1\\0\\0\end{pmatrix}H_\theta(\pm z),\\
\mathbf{H}_p^{\mathrm{i},\pm}(\mathbf{r}) &= \sqrt{\frac{i}{2S_0}}\mathrm{e}^{\pm ikz}\begin{pmatrix}0\\\pm1\\0\end{pmatrix}H_\theta(\pm z).
\end{aligned}
\tag{A.7}
$$

Here, we assume that the z-axis is directed from the top to the bottom surface as in Fig. 2.6a. The ± sign denotes top and bottom radiation channels, respectively. The function $H_\theta(\pm z)$ is the Heaviside theta function. The area of the unit cell surface is S_u. The outgoing functions are the same as incoming in Eq. A.7 but with opposite sign of propagating exponents.

For radiation modes from the zeroth order diffraction order (normal to the surface plane) and for real k Eq. A.2 can be simplified to

$$
\oint_{S_V} d\mathbf{S}\cdot\left[\mathbf{E}_N^{\mathrm{o}}\times(\mathbf{H}_{N'}^{\mathrm{o}})^* + (\mathbf{E}_{N'}^{\mathrm{o}})^*\times\mathbf{H}_N^{\mathrm{o}}\right] = \delta_{N,N'}. \tag{A.8}
$$

This correspondence also holds for complex k-vectors with small imaginary part, e.g. at the resonant frequencies of high-Q modes.

A.3 Resonant states (quasi-normal modes) of resonators

A.3.1 Definition, normalization and orthogonality

In this section we summarize some properties of resonant states (quasi-normal modes), which are eigenmodes of open electromagnetic systems. The eigenmodes of the structure are self-standing electromagnetic excitations characterized by a discrete set of complex resonant frequencies $\Omega_n = \omega_n - i\gamma_n$, where γ_n is a half of inverse mode radiative lifetime. In this section, we assume that the material is a lossless dielectric. For extended photonic structures of infinite size, the spectrum of RSs includes the contribution from the Rayleigh anomalies, representing a continuous distribution of modes in the cuts of ω-plane [144]. We introduce the complex wavevector for resonant states (RSs) as $k_n = (\omega_n - i\gamma_n)/c$. The electromagnetic fields of RSs satisfy

$$\begin{aligned} \nabla \times \mathbf{E}_n &= i k_n \mathbf{H}_n, \\ \nabla \times \mathbf{H}_n &= -i k_n \varepsilon(\mathbf{r}) \mathbf{E}_n. \end{aligned} \tag{A.9}$$

The RSs are divergent at large distances from the structure and require specific normalization to compensate the divergence. We impose the RS normalization proposed by the group of E. Muljarov [202]

$$N_n = \int\limits_V dV \left(\varepsilon \mathbf{E}_n \cdot \mathbf{E}_n - \mathbf{H}_n \cdot \mathbf{H}_n\right) + i \oint\limits_{S_V} d\mathbf{S} \cdot \left(\mathbf{E}_n \times \frac{\partial \mathbf{H}_n^{(\mathrm{reg})}}{\partial k} - \frac{\partial \mathbf{E}_n^{(\mathrm{reg})}}{\partial k} \times \mathbf{H}_n \right). \tag{A.10}$$

Here, N_n is the normalization constant which is usually equal to 1. The volume and surface integration are performed over the minimal convex volume V and its surface S_V. For compact finite-size resonators V and S_V coincide with the volume and surface of the resonator, respectively. For periodic photonic structures, such as metasurfaces, the integration includes one unit cell of the metasurface, and the surface integration goes over the top and bottom surfaces only, because in the periodic directions the integral vanishes. The functions $\mathbf{E}_n^{(\mathrm{reg})}$ and $\mathbf{H}_n^{(\mathrm{reg})}$ are the analytical continuation of $\mathbf{E}_n$ and $\mathbf{H}_n$, respectively, over the entire ω-plane, which can be evaluated by decomposition into plane waves at the structure surface [see Eq. (A.17)] [144].

Orthogonality condition for the RSs can be derived from Eqs. (A.9) for n-th and m-th modes using the non-conjugated form of the reciprocity theorem

$$0 = (k_n + k_m) \int\limits_V dV \left(\varepsilon \mathbf{E}_n \cdot \mathbf{E}_m + \mathbf{H}_n \cdot \mathbf{H}_m\right) + i \oint\limits_{S_V} d\mathbf{S} \cdot \left(\mathbf{E}_n \times \mathbf{H}_m + \mathbf{E}_m \times \mathbf{H}_n\right). \tag{A.11}$$

The electric-electric Green's function of the resonator $\hat{\mathbf{G}}(\omega, \mathbf{r}, \mathbf{r}')$ satisfies the equation

$$-\nabla \times \nabla \times \hat{\mathbf{G}}\left(\omega, \mathbf{r}, \mathbf{r}'\right) + k^2 \varepsilon(\mathbf{r}) \hat{\mathbf{G}}\left(\omega, \mathbf{r}, \mathbf{r}'\right) = \hat{\mathbf{1}} \delta\left(\mathbf{r} - \mathbf{r}'\right) \tag{A.12}$$

It can be decomposed into partial contributions of RSs

$$\hat{\mathbf{G}}\left(\omega, \mathbf{r}, \mathbf{r}'\right) = \sum_n c^2 \frac{\mathbf{E}_n(\mathbf{r}) \otimes \mathbf{E}_n(\mathbf{r}')}{\omega\left(\omega - \omega_n + i\gamma_n\right) N_n}. \tag{A.13}$$

The full Green's function of the resonator $\hat{\mathbf{G}}_{6\times 6}(\omega, \mathbf{r}, \mathbf{r}')$ can be decomposed as

$$\hat{\mathbf{G}}_{6\times 6}\left(\omega, \mathbf{r}, \mathbf{r}'\right) = \sum_n c \frac{|F_n(\mathbf{r})\rangle \otimes |F_n(\mathbf{r}')\rangle}{\left(\omega - \omega_n + i\gamma_n\right) N_n}. \tag{A.14}$$

Here,

$$|F_n(\mathbf{r})\rangle = \begin{pmatrix} \mathbf{E}_n(\mathbf{r}) \\ i\mathbf{H}_n(\mathbf{r}) \end{pmatrix}. \tag{A.15}$$

In time domain, it reads

$$\hat{\mathbf{G}}_{6\times 6}\left(t,\mathbf{r},\mathbf{r}'\right) = \sum_n c\frac{|F_n(\mathbf{r})\rangle \otimes |F_n(\mathbf{r}')\rangle}{N_n} e^{-i(\omega_n - i\gamma_n)t}. \tag{A.16}$$

A.3.2 Expansion into modes of the radiation continuum

The RSs form a basis inside the minimal convex volume V including the structure or its unit cell. On the surface of this volume S_V RSs can be expanded over the outgoing waves of the radiation continuum $\mathbf{E}_N^{\mathrm{o}}$ and $\mathbf{H}_N^{\mathrm{o}}$ [201]

$$\begin{aligned} \mathbf{E}_n(\mathbf{r}\in S_V) &= \sum_N \kappa_{nN}\mathbf{E}_N^{\mathrm{o}}(\mathbf{r}\in S_V, k_n), \\ \mathbf{H}_n(\mathbf{r}\in S_V) &= \sum_N \kappa_{nN}\mathbf{H}_N^{\mathrm{o}}(\mathbf{r}\in S_V, k_n). \end{aligned} \tag{A.17}$$

The field distributions outside of V can be restored by continuation of the Eqs. (A.17) to the exterior region. The expansion coefficients are given by overlap integral of RSs with the incoming waves $\mathbf{E}_N^{\mathrm{i}}$ and $\mathbf{H}_N^{\mathrm{i}}$ [201]

$$\kappa_{nN} = -i\oint_{S_V} d\mathbf{S}\cdot\left(\mathbf{E}_n \times \mathbf{H}_N^{\mathrm{i}}(k_n) - \mathbf{E}_N^{\mathrm{i}}(k_n)\times\mathbf{H}_n\right). \tag{A.18}$$

A.3.3 Radiative lifetime and quality factor

From Eqs. (A.9) it follows that for each RS with the fields $\mathbf{E}_n$ and $\mathbf{H}_n$, and nonzero real part of k_n, there is always a conjugated RS in the spectrum with the fields $\mathbf{E}_n^*$, $\mathbf{H}_n^*$, and wavevector $-k_n^*$. Applying the orthogonality condition Eq. (A.11) for a pair of conjugated RSs, we get the equation for the mode radiative lifetime τ_n

$$\frac{1}{\tau_n} = 2\gamma_n = \frac{c\oint_{S_V} d\mathbf{S}\cdot\left(\mathbf{E}_n\times\mathbf{H}_n^* + \mathbf{E}_n^*\times\mathbf{H}_n\right)}{\int_V dV\left(\varepsilon|\mathbf{E}_n|^2 + |\mathbf{H}_n|^2\right)}. \tag{A.19}$$

We see that τ_n^{-1} is the ratio the Poynting's vector flux through the surface S_V and the total energy in the volume V, which in agreement with the Poynting's theorem [192]. The quality factor Q_n can be evaluated as

$$Q = \omega_n\tau_n. \tag{A.20}$$

We can express the radiative lifetime via the coupling coefficients of RSs to the modes of the radiation continuum.

Periodic structures. We select a normalized basis of radiation waves with the fields $\mathbf{E}_N$ and $\mathbf{H}_N$ [see Eqs. (A.7)] evaluated for the complex k-vector k_n and expand the RSs using Eqs. (A.17). For periodic photonic structures the radiation continuum is discretized into diffraction channels. Assuming sub-diffractive regime and sufficiently large mode quality factor $Q > 10$, we can expand the numerator of Eq. (A.19) neglecting the outgoing flux of higher order diffraction modes due to $\operatorname{Re} k_n \gg \operatorname{Im} k_n$. Then, the contribution of higher-order diffraction modes to the integral will be zero and using Eq. A.8 we get

$$\oint_{S_V} d\mathbf{S} \cdot \left(\mathbf{E}_n \times \mathbf{H}_n^* + \mathbf{E}_n^* \times \mathbf{H}_n\right) = \sum_{\tilde{N}} |\kappa_{n\tilde{N}}|^2. \tag{A.21}$$

The summation goes over $\tilde{N}$ (s and p polarization, and top and bottom indices) which include the zeroth order diffraction waves only. The radiative linewidth is given by

$$\frac{2\gamma_n}{c} = \frac{\sum_{\tilde{N}} |\kappa_{n\tilde{N}}|^2}{W_n}, \tag{A.22}$$

$$W_n = \int_V dV \left(\varepsilon |\mathbf{E}_n|^2 + |\mathbf{H}_n|^2\right). \tag{A.23}$$

Individual resonators. We select a normalized basis of radiation modes with the fields $\mathbf{E}_N$ and $\mathbf{H}_N$ [see Eqs. (A.3)] evaluated for the complex k-vector k_n and expand the RSs using Eqs. (A.17). Assuming sufficiently large mode quality factor $Q > 10$, we can expand the numerator of Eq. (A.19) and using Eq. A.6 we get

$$\oint_{S_V} d\mathbf{S} \cdot \left(\mathbf{E}_n \times \mathbf{H}_n^* + \mathbf{E}_n^* \times \mathbf{H}_n\right) = \sum_{N} \kappa_{nN}^* \overline{\kappa}_{nN}. \tag{A.24}$$

Here,

$$\overline{\kappa}_{nN} = \sum_{N'} \hat{O}_{N,N'} \kappa_{nN'}, \tag{A.25}$$

and $\hat{O}$ is the time reversal matrix for the resonant amplitude [203]

$$\hat{O}_{N,N'} = (-1)^m \delta_{\tau,\tau'} \delta_{l,l'} \delta_{m,-m'} \tag{A.26}$$

The radiative linewidth is given by

$$\frac{2\gamma_n}{c} = \frac{\sum_N \kappa_{nN}^* \overline{\kappa}_{nN}}{W_n}. \tag{A.27}$$

A.3.4 Scattering matrix decomposition

The S-matrix of a resonant photonic structure can be decomposed into contributions of RS via the pole expansion method [201]

$$\hat{S}_{NN'} = \hat{S}^{\mathrm{nr}}_{NN'} + \sum_n \frac{\kappa_{nN}\kappa_{nN'}}{N_n(k-k_n)}. \tag{A.28}$$

The first term represents the so-called non-resonant (background) contribution to the S-matrix [204]. It can be evaluated numerically. The coefficients κ_{nN} are the frequency independent coupling constants between the n-th RS and the N-th channel of the radiation continuum. The coupling coefficients can be evaluated as the residues of the S-matrix at $k = k_n$[201]

$$\kappa_{nN} = -k_n \int_V dV\ (\varepsilon(\mathbf{r})-1)\mathbf{E}_n \cdot \mathbf{E}^{\mathrm{i}}_N(k_n). \tag{A.29}$$

Here, $\mathbf{E}_N$ is the normalized electric field of the N-th mode of the radiation continuum. Using the non-conjugated form of the reciprocity theorem for the fields $\mathbf{E}_n$, $\mathbf{H}_n$, $\mathbf{E}^{\mathrm{i}}_N$, and $\mathbf{H}^{\mathrm{i}}_N$, we can transform the volume integral in Eq. (A.29) to the surface integral

$$\begin{aligned} &\nabla\left(\mathbf{E}_n \times \mathbf{H}^{\mathrm{i}}_N(k_n) - \mathbf{E}^{\mathrm{i}}_N(k_n)\times\mathbf{H}_n\right) = \\ &\qquad \mathbf{H}^{\mathrm{i}}_N(k_n)\cdot\nabla\times\mathbf{E}_n - \mathbf{E}_n\cdot\nabla\times\mathbf{H}^{\mathrm{i}}_N(k_n) + \mathbf{E}^{\mathrm{i}}_N(k_n)\cdot\nabla\times\mathbf{H}_n - \mathbf{H}_n\cdot\nabla\times\mathbf{E}^{\mathrm{i}}_N(k_n) = \\ &\qquad\qquad -ik_n(\varepsilon(\mathbf{r})-1)\mathbf{E}_n\cdot\mathbf{E}^{\mathrm{i}}_N(k_n). \end{aligned} \tag{A.30}$$

Integrating the left and right side over the volume V we get

$$\kappa_{nN} = -i\oint_{S_V} d\mathbf{S}\cdot\left(\mathbf{E}_n\times\mathbf{H}^{\mathrm{i}}_N(k_n) - \mathbf{E}^{\mathrm{i}}_N(k_n)\times\mathbf{H}_n\right). \tag{A.31}$$

This expression coincides with Eq. (A.18), which is a consequence of the reciprocity of the system. The same correspondence holds for any background field satisfying the Maxwell's equations of the system without the resonator

$$-k_n\int_V dV\ (\varepsilon(\mathbf{r})-1)\mathbf{E}_n\cdot\mathbf{E}_{\mathrm{bg}}(k_n) = -i\oint_{S_V} d\mathbf{S}\cdot\left(\mathbf{E}_n\times\mathbf{H}_{\mathrm{bg}}(k_n) - \mathbf{E}_{\mathrm{bg}}(k_n)\times\mathbf{H}_n\right). \tag{A.32}$$

A.3.5 Resonant state expansion for individual disk resonators

To calculate the spectrum of complex eigenfrequencies of a dielectric cylindrical resonator we apply the resonant-state expansion [143]. We expand the fields $\mathbf{E}_n$ of resonant state of the cylindrical resonator over the resonant state $\mathbf{E}^{(0)}_\alpha$ of a homogeneous dielectric sphere with the same value of permittivity as for the cylindrical resonator, describing the cylinder

$$\mathbf{E}_n = \sum_\alpha b^n_\alpha \mathbf{E}^{(0)}_\alpha, \tag{A.33}$$

where $\mathbf{E}_{\alpha}^{(0)}$ satisfies

$$\nabla\times\nabla\times\mathbf{E}_{\alpha}^{(0)} = \varepsilon(\mathbf{r})\frac{\omega_{\alpha}^{2}}{c^{2}}\mathbf{E}_{\alpha}^{(0)}. \tag{A.34}$$

Resonant states $\mathbf{E}_{j}$ satisfy the perturbed equation

$$\nabla\times\nabla\times\mathbf{E}_{n} = [\varepsilon(\mathbf{r})+\delta\varepsilon(\mathbf{r})]\,\frac{\Omega_{n}^{2}}{c^{2}}\mathbf{E}_{n}, \tag{A.35}$$

where $\delta\varepsilon(\mathbf{r})$ is a perturbation that transforms a sphere into an inscribed cylinder.

The problem is reduced to the matrix equation [189, 190]

$$\frac{1}{\omega_{\alpha}}\sum_{\beta}\left[\delta_{\alpha\beta}+W_{\alpha\beta}\right]b_{\beta}^{n} = \frac{1}{\Omega_{n}}b_{\alpha}^{n}, \tag{A.36}$$

with the elements of the perturbation matrix $W_{\alpha\beta}$ were defined as

$$W_{\alpha\beta} = \frac{1}{2}\int dV\ \delta\varepsilon(\mathbf{r})\mathbf{E}_{\alpha}^{(0)}\cdot\mathbf{E}_{\beta}^{(0)}. \tag{A.37}$$

.

A.4 Local field enhancement engineering

In this section we derive the exact expression for the field enhancement of the local field. The scattered field can be decomposed into contributions of resonant states

$$\mathbf{E}_{\mathrm{sc}}(\omega,\mathbf{r}) = \sum_{n} a_{n}(\omega)\frac{\mathbf{E}_{n}(\mathbf{r})}{N_{n}}, \tag{A.38}$$

where a_{n} is the resonant amplitude and its frequency dependence is a simple pole dependence, and N_{n} is the RS normalization. To get the expression for the resonant amplitude, we evaluate $\mathbf{E}_{\mathrm{sc}}$ by using the Lippmann-Schwinger equation

$$\mathbf{E}_{\mathrm{sc}}(\omega,\mathbf{r}) = -k^{2}\int d\mathbf{r}'\left(\epsilon(\mathbf{r}')-1\right)\hat{\mathbf{G}}\left(\omega,\mathbf{r},\mathbf{r}'\right)\cdot\mathbf{E}_{\mathrm{bg}}\left(\omega,\mathbf{r}'\right). \tag{A.39}$$

Here, $\hat{\mathbf{G}}$ is the resonator's Green's function and $\mathbf{E}_{\mathrm{bg}}$ is the background field satisfying the Maxwell's equations for the system without the resonator. By using Eq. A.13 we decompose the Green's function into contributions of RSs and get the expression for the resonant amplitudes

$$a_{n}(\omega) = -\frac{\omega}{\left(\omega-\omega_{n}+i\gamma_{n}\right)}\int_{V} d\mathbf{r}(\epsilon(\mathbf{r})-1)\mathbf{E}_{n}(\mathbf{r})\cdot\mathbf{E}_{\mathrm{bg}}(\omega,\mathbf{r}). \tag{A.40}$$

We assume the excitation frequency $\omega\simeq\omega_{0}$ is in the vicinity of the RS with $n=0$ and the RS has low radiation losses $d\gamma_{0}/c\ll 1$, where d is the characteristic size of the resonating system. Then, the volume integral in the resonant amplitude can be recast to the surface integral according to Eq. A.32

$$a_0(\omega) = (-i)\frac{c}{(\omega - \omega_0 + i\gamma_0)} \oint_{S_V} d\mathbf{S} \cdot \left(\mathbf{E}_0 \times \mathbf{H}_{\mathrm{bg}}(\omega) - \mathbf{E}_{\mathrm{bg}}(\omega) \times \mathbf{H}_0\right). \tag{A.41}$$

Here, the surface integration goes over the minimal convex volume that includes the resonator. The volume is chosen in the way to make the modes of the radiation continuum to be orthogonal on its surface.

The background field can be expanded into incoming and outgoing radiation waves. The outgoing waves do not contribute to the surface integral because the RS mode has outgoing nature. So, we can write

$$a_0(\omega) = \frac{c \sum\limits_N \kappa_{0N} s_N^{\mathrm{i}}}{\omega - \omega_0 + i\gamma_0} \tag{A.42}$$

Here, s_N^{i} is the amplitudes of incoming waves in the background field expansion. Thus, the scattered field is

$$\mathbf{E}_{\mathrm{sc}}(\omega, \mathbf{r}) = a_0(\omega)\frac{\mathbf{E}_0(\mathbf{r})}{N_0} \tag{A.43}$$

Periodic structures. We assume that $\mathbf{E}_{\mathrm{bg}}$ is a p-polarized monochromatic plane wave propagating along the positive z-direction and express it using the incoming and outgoing radiation waves (see Eq. A.7). We assume that z-axis is directed from top to the bottom surface of the metasurface. In this case the incoming amplitude is nonzero for the top p-polarized radiation channel $s_{t,p}^{\mathrm{i}} = \sqrt{-2S_{\mathrm{u}}\, i}\, E_{\mathrm{inc}}$. Thus, at the resonance $\omega = \omega_0$ the amplitude a_0 can be expressed via the coupling coefficient $\kappa_{0,t,p}$ (see Eq. 2.22)

$$a_0(\omega_0) = \frac{(2iS_{\mathrm{u}})^{1/2} c}{\gamma_0} \kappa_{0,t,p} E_{\mathrm{inc}}, \tag{A.44}$$

where $E_{\mathrm{inc}} = |\mathbf{E}_{\mathrm{bg}}|$. For periodic photonic structures in the sub-diffraction limit $\kappa_{0,t,p}$ can be expressed via the radiative linewidth $\gamma_{0,\mathrm{rad}}$ assuming the structure possesses up-down symmetry and the RS of interest is coupled to one polarization only (see Eq. 2.24). Then,

$$|a_0|^2 = 2cS_{\mathrm{u}} W_0 \frac{\gamma_{0,\mathrm{rad}}}{\gamma_0^2} |E_{\mathrm{inc}}|^2. \tag{A.45}$$

For further analysis we introduce the exact mode volume V_0 [151]

$$V_0(\mathbf{r}) = \frac{N_0}{2\left(\mathbf{E}_0(\mathbf{r}) \cdot \mathbf{e}(\mathbf{r})\right)^2}, \tag{A.46}$$

where $\mathbf{e}$ is a unit vector of a test dipole at the point $\mathbf{r}$. The maximal local field is achieved at the point $\mathbf{r}_0$ where the mode volume is minimal. To find the minimal mode volume we evaluate Eq. A.46 at the field hotspot and find the dipole orientation which provides the highest overlap. In this case we can define the maximal local field E_{loc} as

$$E_{\text{loc}} = a_0 \frac{\mathbf{E}_0(\mathbf{r}_0)\cdot\mathbf{e}(\mathbf{r}_0)}{N_0} = \frac{a_0}{(2N_0 V_0(\mathbf{r}_0))^{1/2}}. \tag{A.47}$$

Finally, the local field enhancement $|u|^2$ is given by

$$|u|^2 = \frac{|E_{\text{loc}}|^2}{|E_{\text{inc}}|^2} = \frac{c S_{\text{u}} W_0}{|N_0|} \frac{\gamma_{0,\text{rad}}}{\gamma_0^2 V_0}. \tag{A.48}$$

Also, we can rewrite it as

$$|u|^2 = \frac{1}{\pi}\left(\frac{\lambda S_{\text{u}}}{V_0}\right)\frac{Q_0^2}{Q_{0,\text{rad}}}. \tag{A.49}$$

Here, we assume $W_0 \simeq |N_0|$ because the radiation losses for the RS are low $d\gamma_0/c \ll 1$.

Individual subwavelength resonators Following the procedure described above, the local field enhancement can be written as

$$|u|^2 = \frac{2}{\pi}\left(\frac{\lambda S_0^{\text{eff}}}{V_0}\right)\frac{Q_0^2}{Q_{0,\text{rad}}}. \tag{A.50}$$

Here, S_0^{eff} is the effective antenna aperture

$$S_0^{\text{eff}} = \frac{1}{2|E_{\text{inc}}|^2} \frac{|\sum_N \kappa_{0N} s_N^{\text{i}}|^2}{\sum_N \kappa_{0N}^* \overline{\kappa}_{0N}} \tag{A.51}$$

A.5 Generalized Fano formula

A.5.1 Transmittance of metasurfaces

We derive analytical expressions for the transmittance of the metasurface in subdiffraction limit in the vicinity of one resonant state. The scattering matrix of the metasurface operating in the sub-diffraction limit and for fixed incident polarization is a 2×2 matrix. We consider a p-polarized incident plane wave propagating from top to bottom as shown in Fig. 2.6a. The S-matrix can be decomposed into contributions of RSs via pole expansion. The transmission amplitude t is the non-diagonal element of the S-matrix from Eq. (A.28)

$$t(\omega) = \tau(\omega) + \sum_n \frac{(-1)^{p_n}\left(\kappa_{n,p}^{\text{t}}\right)^2}{N_n(k-k_n)}. \tag{A.52}$$

Here, $p_n = 0, 1$ is the n-th mode parity with respect up-down reflection symmetry.

We study the transmission coefficient in the vicinity of one of the RSs with $n = 0$. Then, the expression for the transmission can be rewritten as

$$t(\omega) = B(\omega) - i\frac{A}{\Delta\omega + i}, \tag{A.53}$$

$$A = \frac{W_0}{|N_0|}\exp\left(2i\arg(\kappa_{0,p}) + i\pi(p_0 + 1/2) - i\arg(N_0)\right) \tag{A.54}$$

$$B(\omega) = \tau(\omega) + \sum_{n\neq 0}\frac{(-1)^{p_n}\left(\kappa^{\mathrm{t}}_{n,p}\right)^2}{N_n(k - k_n)}, \tag{A.55}$$

$$\Delta\omega = \frac{(\omega - \omega_0)}{\gamma_0}. \tag{A.56}$$

By straightforward but quite cumbersome rearrangements of terms of Eq. (A.53) the transmittance $T = |t|^2$ can be written as a generalized Fano formula

$$T(\omega) = \frac{T_{\mathrm{A}}}{1+q^2}\frac{(q+\Delta\omega)^2}{1+\Delta\omega^2} + T_{\mathrm{nr}}. \tag{A.57}$$

The parameters are

$$q(\omega) = \tan\frac{\psi}{2}, \tag{A.58}$$

$$\cot\psi = \cot\varphi - \frac{|A|}{2|B|\sin\phi}, \tag{A.59}$$

$$\phi = \arg(AB^*), \tag{A.60}$$

$$T_{\mathrm{A}} = |A||A - 2B|, \tag{A.61}$$

$$T_{\mathrm{nr}} = |B|^2 - \frac{T_{\mathrm{A}}}{1+q^2}. \tag{A.62}$$

Here q is the Fano asymmetry parameter, T_{A} and T_{nr} describe the background contribution of non-resonant modes to the resonant peak amplitude and the offset, respectively.

A.5.2 Scattering cross section of individual resonators

We study the scattering cross section of a disk resonator characterized by isotropic dielectric permittivity $\epsilon(\mathbf{r})$. The resonator is lossless which implies that absorption is zero at the frequency region of interest. The incident wave is a linearly polarized plane wave $\mathbf{E}_{\mathrm{inc}}$

$$\mathbf{E}_{\mathrm{bg}}(\omega, \mathbf{r}) = \mathbf{E}_{\mathrm{inc}}\exp(i\mathbf{k}_{\mathrm{inc}}\cdot\mathbf{r}), \tag{A.63}$$

where the amplitude $\mathbf{E}_{\mathrm{inc}}$ is real, and $\mathbf{k}_{\mathrm{inc}} = k\mathbf{n}_{\mathrm{inc}}$

The scattering cross section σ_{sc} is equal to the extinction cross section. We apply the optical theorem to calculate the extinction cross section [142]

$$\sigma_{\mathrm{sc}} = \frac{4\pi}{k|\mathbf{E}_{\mathrm{inc}}|^2}\mathrm{Im}\left[\mathbf{E}_{\mathrm{inc}}\cdot\hat{\mathbf{E}}_{\mathrm{sc}}(\mathbf{n}_{\mathrm{inc}})\right], \tag{A.64}$$

where $\hat{\mathbf{E}}_{\mathrm{sc}}(\mathbf{n}_{\mathrm{inc}})$ is the amplitude of scattered field in the direction of the incident wave $\mathbf{n}_{\mathrm{inc}}$.

The scattered field satisfies the Lippmann-Schwinger equation

$$\mathbf{E}_{\mathrm{sc}}(\mathbf{r}) = -k^2 \int d\mathbf{r}\ (\epsilon(\mathbf{r})-1)\mathbf{G}_{\mathrm{f}}(\omega,\mathbf{r},\mathbf{r})\cdot\left[\mathbf{E}_{\mathrm{bg}}(\omega,\mathbf{r})+\mathbf{E}_{\mathrm{sc}}(\mathbf{r})\right], \tag{A.65}$$

where $\mathbf{G}_{\mathrm{f}}$ is the free space dyadic Green's function.

The amplitude of the far-field distribution of $\hat{\mathbf{G}}_{\mathrm{f}}$ in the direction of incident field is given by

$$\hat{\mathbf{G}}_{\mathrm{f}}(\omega,\mathbf{n}_{\mathrm{inc}},\mathbf{r}^{'}) = -\left[\hat{I}-\mathbf{n}_{\mathrm{inc}}\otimes\mathbf{n}_{\mathrm{inc}}\right]\frac{\exp[-i\mathbf{k}_{\mathrm{inc}}\cdot\mathbf{r}^{'})]}{4\pi}. \tag{A.66}$$

Substitution of Eq. A.65 and Eq. A.66 into Eq. A.64 gives

$$\sigma_{\mathrm{sc}} = \frac{1}{|\mathbf{E}_{\mathrm{inc}}|^2}\mathrm{Im}\left\{k\int d\mathbf{r}\ (\epsilon(\mathbf{r})-1)\mathbf{E}^{*}_{\mathrm{bg}}(\omega,\mathbf{r})\cdot\left[\mathbf{E}_{\mathrm{bg}}(\omega,\mathbf{r})+\mathbf{E}_{\mathrm{sc}}(\mathbf{r})\right]\right\}. \tag{A.67}$$

The scattered field can be expanded into contributions of resonant states

$$\mathbf{E}_{\mathrm{sc}}(\mathbf{r}) = -k\sum_n \frac{\mathbf{E}_n(\mathbf{r})}{N_n(k-k_n)}\int d\mathbf{r}^{'}\ \left(\epsilon(\mathbf{r}^{'})-1\right)\mathbf{E}_n(\mathbf{r}^{'})\cdot\mathbf{E}_{\mathrm{bg}}(\omega,\mathbf{r}^{'}). \tag{A.68}$$

Since the disk resonator possesses inversion symmetry, each resonant state can be classified with respect to the inversion symmetry as $\mathbf{E}_n(-\mathbf{r}) = (-1)^{p_n}\mathbf{E}_n(\mathbf{r})$, where $p_n = 0,1$ is the parity defining even or odd resonant state, respectively. Using this properties, we can re-write the expression for σ_{sc} as

$$\sigma_{\mathrm{sc}} = \frac{1}{k^2}\left(C(\omega)-\mathrm{Im}\sum_n\frac{(-1)^{p_n}D_n^2}{N_n(k-k_n)}\right), \tag{A.69}$$

Here, $C(\omega)$ and the coupling coefficients $D(\omega)$ are

$$C(\omega) = k^3\int d\mathbf{r}\ (\epsilon(\mathbf{r})-1), \tag{A.70}$$

$$D_n(\omega) = -k^2\int d\mathbf{r}\ (\epsilon(\mathbf{r})-1)\mathbf{E}_n(\mathbf{r})\cdot\frac{\mathbf{E}_{\mathrm{bg}}(\omega,\mathbf{r})}{|\mathbf{E}_{\mathrm{inc}}|}. \tag{A.71}$$

We focus on frequencies in the vicinity of the eigenfrequency $\Omega_0 = \omega_0 - i\gamma_0$ of the particular resonant state with $n = 0$. For the RS with low radiation losses $d\gamma_0/c \ll 1$, where d is the characteristic scale of the resonator, the coupling coefficient can be rewritten as

$$D_0 = -\frac{i\omega_0}{c|\mathbf{E}_{\mathrm{inc}}|}\oint_{S_V} d\mathbf{S}\cdot\left(\mathbf{E}_0\times\mathbf{H}_{\mathrm{bg}}(\omega_0)-\mathbf{E}_{\mathrm{bg}}(\omega_0)\times\mathbf{H}_0\right). \tag{A.72}$$

Here, the surface integration S_V goes over the minimal convex volume that includes the resonator. The volume is chosen in the way to make the modes of the radiation continuum to be orthogonal on its surface. Such representation allows to expand D_0 via the coupling coefficients κ_{0N} of the RS with the radiation continuum incoming waves. For this we expand the incoming component of the background field into the incoming waves with amplitudes s_N^{i}. The outgoing waves do not contribute to the surface integral

$$D_0 = \sum_N d_{0N} \kappa_{0N}, \tag{A.73}$$

$$d_{0N} = \frac{\omega_0}{c|\mathbf{E}_{\mathrm{inc}}|} s_N^{\mathrm{i}}(\omega_0). \tag{A.74}$$

In general, the amplitudes are

$$s_N^{\mathrm{i}}(\omega_0) = i \oint_{S_V} d\mathbf{S} \cdot \left(\mathbf{E}_N^{\mathrm{o}} \times \mathbf{H}_{\mathrm{bg}}(\omega_0) - \mathbf{E}_{\mathrm{bg}}(\omega_0) \times \mathbf{H}_N^{\mathrm{o}}\right). \tag{A.75}$$

For the plane wave the amplitudes are

$$s_N^{\mathrm{i}}(\omega_0) = \frac{4\pi}{k} \left(\hat{\mathbf{E}}_N^{\mathrm{o}}(\mathbf{n}_{\mathrm{inc}})\right)^* \cdot \mathbf{E}_{\mathrm{inc}}. \tag{A.76}$$

Here, $\hat{\mathbf{E}}_N^{\mathrm{o}}$ is the far-field amplitude of the outgoing channel.

The SCS can be written as

$$\sigma_{\mathrm{sc}} = \frac{1}{k^2} \left[B(\omega) + \mathrm{Im}\left\{ \frac{A(\omega)}{\Delta\omega + i} \right\} \right], \tag{A.77}$$

where the coefficients are determined below

$$B(\omega) = C(\omega) - \mathrm{Im} \sum_{n \neq 0} \frac{(-1)^{p_n} D_n^2(\omega)}{N_n(k - k_n)}, \tag{A.78}$$

$$A(\omega) = (-1)^{p_0+1} \frac{c D_0^2}{W_0 \gamma_0}, \tag{A.79}$$

$$\Delta\omega = \frac{\omega - \omega_0}{\gamma_0}. \tag{A.80}$$

Here, we replaced the normalization N_0 with the full energy of the mode $W_0 = \int_V dV \left(\varepsilon |\mathbf{E}_0|^2 + |\mathbf{H}_0|^2\right)$ because the mode is high-Q.

Finally, we reduce Eq. A.77 to the generalized Fano formula

$$\sigma_{\mathrm{sc}} = \frac{1}{k^2} \left[\frac{I_{\mathrm{A}}}{1+q^2} \frac{(q+\Delta\omega)^2}{1+\Delta\omega^2} + I_{\mathrm{nr}}(\omega) \right]. \tag{A.81}$$

Here the Fano parameters are

$$q(\omega) = -\cot[\phi], \tag{A.82}$$

$$\phi(\omega) = \arg[D_0] + \pi(p_0 - 1)/2, \tag{A.83}$$

$$I_{\mathrm{A}} = |A| = \frac{c|D_0|^2}{W_0\gamma_0}, \tag{A.84}$$

$$I_{\mathrm{nr}}(\omega) = B(\omega) - \frac{I_{\mathrm{A}}}{1+q^2}. \tag{A.85}$$

Here, we assume $\arg[N_0] = 0$ because the mode has low radiation losses.

A.6 Keldysh theory for temporal dynamics of free-carrier generation

The temporal dynamics of free-carrier generation in Si under the applied field $\mathbf{E}(\mathbf{r}, t)$ can be calculated as [160]

$$\frac{\partial n_p(\mathbf{r})}{\partial t} = R(t, \omega, |\mathbf{E}(\mathbf{r}, t)|) \tag{A.86}$$

Here, the generation rate R is calculated using the Keldysh expression

$$R(t, \omega, |\mathbf{E}|) = 2\frac{2\omega}{9\pi}\left(\frac{m^*\omega}{\hbar}\frac{\sqrt{1+\gamma_K^2}}{\gamma_K}\right)^{\frac{3}{2}} Q\left(\gamma_K, \frac{\Delta_{\mathrm{eff}}}{\hbar\omega}\right) \times \exp\left[-\pi\left\langle\frac{\Delta_{\mathrm{eff}}}{\hbar\omega}+1\right\rangle\frac{\mathscr{K}(\phi)-\mathscr{E}(\phi)}{\mathscr{E}(\Theta)}\right] \tag{A.87}$$

where

$$Q(\gamma_K, x) = \sqrt{\frac{\pi}{2\mathscr{K}(\Theta)}} \times \sum_{m=0}^{\infty}\exp\left[-\pi\cdot\frac{\mathscr{K}(\phi)-\mathscr{E}(\phi)}{\mathscr{E}(\Theta)}\cdot m\right] \times \Phi\left[\sqrt{\frac{\pi(\langle x+1\rangle - x + m)}{2\cdot\mathscr{K}(\Theta)\cdot\mathscr{E}(\Theta)}}\right] \tag{A.88}$$

K and E are complete elliptic integrals of first and second kind, respectively, with dimensionless parameters

$$\Theta = \frac{1}{1+\gamma_K^2}, \qquad \phi = \frac{\gamma_K^2}{1+\gamma_K^2}. \tag{A.89}$$

Other parameters are defined as

$$\Phi(x) = \int_0^x \exp\left(\xi^2 - x^2\right) d\xi, \qquad \Delta_{\mathrm{eff}} = \frac{2}{\pi}\Delta\cdot\left[\frac{\sqrt{1+\gamma_K^2}}{\gamma_K}\mathscr{E}(\Theta)\right]. \tag{A.90}$$

The Keldysh parameter is defined as

$$\gamma_K(\mathbf{r}) = \frac{\omega\sqrt{m^*\Delta}}{\mathrm{e}|\mathbf{E}(\mathbf{r},t)|}. \tag{A.91}$$

Here, Δ is the intrinsic Si band gap, m^* is the reduced mass of the effective electron and hole masses.

Bibliography

[1] P. N. Prasad, *Nanophotonics.* John Wiley & Sons, 2004.

[2] R. Kirchain and L. Kimerling, "A roadmap for nanophotonics," *Nature Photonics*, vol. 1, no. 6, pp. 303–305, 2007.

[3] A. F. Koenderink, A. Alù, and A. Polman, "Nanophotonics: Shrinking light-based technology," *Science*, vol. 348, no. 6234, pp. 516–521, 2015.

[4] S. A. Maier *et al.*, *Plasmonics: fundamentals and applications*, vol. 1. Springer, 2007.

[5] J. A. Schuller, E. S. Barnard, W. Cai, Y. C. Jun, J. S. White, and M. L. Brongersma, "Plasmonics for extreme light concentration and manipulation," *Nature materials*, vol. 9, no. 3, pp. 193–204, 2010.

[6] J. R. Lakowicz, "Plasmonics in biology and plasmon-controlled fluorescence," *Plasmonics*, vol. 1, no. 1, pp. 5–33, 2006.

[7] H. A. Atwater and A. Polman, "Plasmonics for improved photovoltaic devices," *Materials for sustainable energy: a collection of peer-reviewed research and review articles from Nature Publishing Group*, pp. 1–11, 2011.

[8] M. S. Tame, K. McEnery, Ş. Özdemir, J. Lee, S. A. Maier, and M. Kim, "Quantum plasmonics," *Nature Physics*, vol. 9, no. 6, pp. 329–340, 2013.

[9] J. B. Pendry, A. J. Holden, D. J. Robbins, and W. Stewart, "Magnetism from conductors and enhanced nonlinear phenomena," *IEEE transactions on microwave theory and techniques*, vol. 47, no. 11, pp. 2075–2084, 1999.

[10] A. B. Evlyukhin, S. M. Novikov, U. Zywietz, R. L. Eriksen, C. Reinhardt, S. I. Bozhevolnyi, and B. N. Chichkov, "Demonstration of magnetic dipole resonances of dielectric nanospheres in the visible region," *Nano letters*, vol. 12, no. 7, pp. 3749–3755, 2012.

[11] A. I. Kuznetsov, A. E. Miroshnichenko, Y. H. Fu, J. Zhang, and B. Luk'Yanchuk, "Magnetic light," *Scientific reports*, vol. 2, no. 1, pp. 1–6, 2012.

[12] I. Staude, A. E. Miroshnichenko, M. Decker, N. T. Fofang, S. Liu, E. Gonzales, J. Dominguez, T. S. Luk, D. N. Neshev, I. Brener, *et al.*, "Tailoring directional scattering through magnetic and electric resonances in subwavelength silicon nanodisks," *ACS nano*, vol. 7, no. 9, pp. 7824–7832, 2013.

[13] D. Lin, P. Fan, E. Hasman, and M. L. Brongersma, "Dielectric gradient metasurface optical elements," *science*, vol. 345, no. 6194, pp. 298–302, 2014.

[14] M. Khorasaninejad, W. T. Chen, R. C. Devlin, J. Oh, A. Y. Zhu, and F. Capasso, "Metalenses at visible wavelengths: Diffraction-limited focusing and subwavelength resolution imaging," *Science*, vol. 352, no. 6290, pp. 1190–1194, 2016.

[15] L. Wang, S. Kruk, H. Tang, T. Li, I. Kravchenko, D. N. Neshev, and Y. S. Kivshar, "Grayscale transparent metasurface holograms," *Optica*, vol. 3, no. 12, pp. 1504–1505, 2016.

[16] W. Yang, S. Xiao, Q. Song, Y. Liu, Y. Wu, S. Wang, J. Yu, J. Han, and D.-P. Tsai, "All-dielectric metasurface for high-performance structural color," *Nature communications*, vol. 11, no. 1, pp. 1–8, 2020.

[17] A. Arbabi, Y. Horie, M. Bagheri, and A. Faraon, "Dielectric metasurfaces for complete control of phase and polarization with subwavelength spatial resolution and high transmission," *Nature nanotechnology*, vol. 10, no. 11, pp. 937–943, 2015.

[18] S. Kruk, B. Hopkins, I. I. Kravchenko, A. Miroshnichenko, D. N. Neshev, and Y. S. Kivshar, "Invited article: Broadband highly efficient dielectric metadevices for polarization control," *Apl Photonics*, vol. 1, no. 3, p. 030801, 2016.

[19] A. I. Kuznetsov, A. E. Miroshnichenko, M. L. Brongersma, Y. S. Kivshar, and B. Luk'yanchuk, "Optically resonant dielectric nanostructures," *Science*, vol. 354, no. 6314, 2016.

[20] D. G. Baranov, D. A. Zuev, S. I. Lepeshov, O. V. Kotov, A. E. Krasnok, A. B. Evlyukhin, and B. N. Chichkov, "All-dielectric nanophotonics: the quest for better materials and fabrication techniques," *Optica*, vol. 4, no. 7, pp. 814–825, 2017.

[21] R. Won, "Into the 'mie-tronic'era," 2019.

[22] I. Staude and J. Schilling, "Metamaterial-inspired silicon nanophotonics," *Nature Photonics*, vol. 11, no. 5, pp. 274–284, 2017.

[23] A. B. Evlyukhin, C. Reinhardt, A. Seidel, B. S. Luk'yanchuk, and B. N. Chichkov, "Optical response features of si-nanoparticle arrays," *Physical Review B*, vol. 82, no. 4, p. 045404, 2010.

[24] A. E. Krasnok, A. E. Miroshnichenko, P. A. Belov, and Y. S. Kivshar, "Huygens optical elements and yagi—uda nanoantennas based on dielectric nanoparticles," *JETP letters*, vol. 94, no. 8, pp. 593–598, 2011.

[25] J.-M. Geffrin, B. García-Cámara, R. Gómez-Medina, P. Albella, L. Froufe-Pérez, C. Eyraud, A. Litman, R. Vaillon, F. González, M. Nieto-Vesperinas, *et al.*, "Magnetic and electric coherence in forward-and back-scattered electromagnetic waves by a single dielectric subwavelength sphere," *Nature communications*, vol. 3, no. 1, pp. 1–8, 2012.

[26] S. Kruk and Y. Kivshar, “Functional meta-optics and nanophotonics governed by mie resonances,” *Acs Photonics*, vol. 4, no. 11, pp. 2638–2649, 2017.

[27] A. V. Kildishev, A. Boltasseva, and V. M. Shalaev, “Planar photonics with metasurfaces,” *Science*, vol. 339, no. 6125, p. 1232009, 2013.

[28] P. Genevet, F. Capasso, F. Aieta, M. Khorasaninejad, and R. Devlin, “Recent advances in planar optics: from plasmonic to dielectric metasurfaces,” *Optica*, vol. 4, no. 1, pp. 139–152, 2017.

[29] S. M. Kamali, E. Arbabi, A. Arbabi, and A. Faraon, “A review of dielectric optical metasurfaces for wavefront control,” *Nanophotonics*, vol. 7, no. 6, pp. 1041–1068, 2018.

[30] F. S. Roux, “Geometric phase lens,” *JOSA A*, vol. 23, no. 2, pp. 476–482, 2006.

[31] M. Decker, I. Staude, M. Falkner, J. Dominguez, D. N. Neshev, I. Brener, T. Pertsch, and Y. S. Kivshar, “High-efficiency dielectric huygens’ surfaces,” *Advanced Optical Materials*, vol. 3, no. 6, pp. 813–820, 2015.

[32] J. B. Mueller, N. A. Rubin, R. C. Devlin, B. Groever, and F. Capasso, “Metasurface polarization optics: independent phase control of arbitrary orthogonal states of polarization,” *Physical review letters*, vol. 118, no. 11, p. 113901, 2017.

[33] Y. Yang, W. Wang, P. Moitra, I. I. Kravchenko, D. P. Briggs, and J. Valentine, “Dielectric meta-reflectarray for broadband linear polarization conversion and optical vortex generation,” *Nano letters*, vol. 14, no. 3, pp. 1394–1399, 2014.

[34] Y. Zhou, H. Zheng, I. I. Kravchenko, and J. Valentine, “Flat optics for image differentiation,” *Nature Photonics*, vol. 14, no. 5, pp. 316–323, 2020.

[35] M. R. Shcherbakov, D. N. Neshev, B. Hopkins, A. S. Shorokhov, I. Staude, E. V. Melik-Gaykazyan, M. Decker, A. A. Ezhov, A. E. Miroshnichenko, I. Brener, *et al.*, “Enhanced third-harmonic generation in silicon nanoparticles driven by magnetic response,” *Nano letters*, vol. 14, no. 11, pp. 6488–6492, 2014.

[36] G. Grinblat, Y. Li, M. P. Nielsen, R. F. Oulton, and S. A. Maier, “Enhanced third harmonic generation in single germanium nanodisks excited at the anapole mode,” *Nano letters*, vol. 16, no. 7, pp. 4635–4640, 2016.

[37] V. F. Gili, L. Carletti, A. Locatelli, D. Rocco, M. Finazzi, L. Ghirardini, I. Favero, C. Gomez, A. Lemaître, M. Celebrano, *et al.*, “Monolithic algaas second-harmonic nanoantennas,” *Optics Express*, vol. 24, no. 14, pp. 15965–15971, 2016.

[38] R. Camacho-Morales, M. Rahmani, S. Kruk, L. Wang, L. Xu, D. A. Smirnova, A. S. Solntsev, A. Miroshnichenko, H. H. Tan, F. Karouta, *et al.*, “Nonlinear generation of vector beams from algaas nanoantennas,” *Nano letters*, vol. 16, no. 11, pp. 7191–7197, 2016.

[39] J. Cambiasso, G. Grinblat, Y. Li, A. Rakovich, E. Cortés, and S. A. Maier, "Bridging the gap between dielectric nanophotonics and the visible regime with effectively lossless gallium phosphide antennas," *Nano letters*, vol. 17, no. 2, pp. 1219–1225, 2017.

[40] M. R. Shcherbakov, A. S. Shorokhov, D. N. Neshev, B. Hopkins, I. Staude, E. V. Melik-Gaykazyan, A. A. Ezhov, A. E. Miroshnichenko, I. Brener, A. A. Fedyanin, *et al.*, "Nonlinear interference and tailorable third-harmonic generation from dielectric oligomers," *Acs Photonics*, vol. 2, no. 5, pp. 578–582, 2015.

[41] A. S. Shorokhov, E. V. Melik-Gaykazyan, D. A. Smirnova, B. Hopkins, K. E. Chong, D.-Y. Choi, M. R. Shcherbakov, A. E. Miroshnichenko, D. N. Neshev, A. A. Fedyanin, *et al.*, "Multifold enhancement of third-harmonic generation in dielectric nanoparticles driven by magnetic fano resonances," *Nano letters*, vol. 16, no. 8, pp. 4857–4861, 2016.

[42] Y. Yang, W. Wang, A. Boulesbaa, I. I. Kravchenko, D. P. Briggs, A. Puretzky, D. Geohegan, and J. Valentine, "Nonlinear fano-resonant dielectric metasurfaces," *Nano letters*, vol. 15, no. 11, pp. 7388–7393, 2015.

[43] S. Liu, M. B. Sinclair, S. Saravi, G. A. Keeler, Y. Yang, J. Reno, G. M. Peake, F. Setzpfandt, I. Staude, T. Pertsch, *et al.*, "Resonantly enhanced second-harmonic generation using iii–v semiconductor all-dielectric metasurfaces," *Nano letters*, vol. 16, no. 9, pp. 5426–5432, 2016.

[44] L. Wang, S. Kruk, K. Koshelev, I. Kravchenko, B. Luther-Davies, and Y. Kivshar, "Nonlinear wavefront control with all-dielectric metasurfaces," *Nano letters*, vol. 18, no. 6, pp. 3978–3984, 2018.

[45] J. Bar-David and U. Levy, "Nonlinear diffraction in asymmetric dielectric metasurfaces," *Nano Letters*, vol. 19, no. 2, pp. 1044–1051, 2019.

[46] S. S. Kruk, L. Wang, B. Sain, Z. Dong, J. Yang, T. Zentgraf, and Y. Kivshar, "Asymmetric parametric generation of images with nonlinear dielectric metasurfaces," *Nature Photonics*, pp. 1–5, 2022.

[47] Y. Gao, Y. Fan, Y. Wang, W. Yang, Q. Song, and S. Xiao, "Nonlinear holographic all-dielectric metasurfaces," *Nano letters*, vol. 18, no. 12, pp. 8054–8061, 2018.

[48] H. Liu, C. Guo, G. Vampa, J. L. Zhang, T. Sarmiento, M. Xiao, P. H. Bucksbaum, J. Vučković, S. Fan, and D. A. Reis, "Enhanced high-harmonic generation from an all-dielectric metasurface," *Nature Physics*, vol. 14, no. 10, pp. 1006–1010, 2018.

[49] S. Makarov, S. Kudryashov, I. Mukhin, A. Mozharov, V. Milichko, A. Krasnok, and P. Belov, "Tuning of magnetic optical response in a dielectric nanoparticle by ultrafast photoexcitation of dense electron–hole plasma," *Nano letters*, vol. 15, no. 9, pp. 6187–6192, 2015.

[50] S. Kruk, A. Poddubny, D. Smirnova, L. Wang, A. Slobozhanyuk, A. Shorokhov, I. Kravchenko, B. Luther-Davies, and Y. Kivshar, "Nonlinear light generation in topological nanostructures," *Nature nanotechnology*, vol. 14, no. 2, pp. 126–130, 2019.

[51] D. Smirnova, S. Kruk, D. Leykam, E. Melik-Gaykazyan, D.-Y. Choi, and Y. Kivshar, "Third-harmonic generation in photonic topological metasurfaces," *Physical review letters*, vol. 123, no. 10, p. 103901, 2019.

[52] G. Li, S. Zhang, and T. Zentgraf, "Nonlinear photonic metasurfaces," *Nature Reviews Materials*, vol. 2, no. 5, pp. 1–14, 2017.

[53] A. Krasnok, M. Tymchenko, and A. Alù, "Nonlinear metasurfaces: a paradigm shift in nonlinear optics," *Materials Today*, vol. 21, no. 1, pp. 8–21, 2018.

[54] B. Sain, C. Meier, and T. Zentgraf, "Nonlinear optics in all-dielectric nanoantennas and metasurfaces: a review," *Advanced Photonics*, vol. 1, no. 2, p. 024002, 2019.

[55] G. Grinblat, "Nonlinear dielectric nanoantennas and metasurfaces: frequency conversion and wavefront control," *ACS Photonics*, vol. 8, no. 12, pp. 3406–3432, 2021.

[56] D. A. Smirnova, A. B. Khanikaev, L. A. Smirnov, and Y. S. Kivshar, "Multipolar third-harmonic generation driven by optically induced magnetic resonances," *Acs Photonics*, vol. 3, no. 8, pp. 1468–1476, 2016.

[57] S. S. Kruk, R. Camacho-Morales, L. Xu, M. Rahmani, D. A. Smirnova, L. Wang, H. H. Tan, C. Jagadish, D. N. Neshev, and Y. S. Kivshar, "Nonlinear optical magnetism revealed by second-harmonic generation in nanoantennas," *Nano letters*, vol. 17, no. 6, pp. 3914–3918, 2017.

[58] M. Rahmani, G. Leo, I. Brener, A. V. Zayats, S. A. Maier, C. De Angelis, H. Tan, V. F. Gili, F. Karouta, R. Oulton, *et al.*, "Nonlinear frequency conversion in optical nanoantennas and metasurfaces: materials evolution and fabrication," *Opto-Electronic Advances*, vol. 1, no. 10, pp. 180021–1, 2018.

[59] C. Schlickriede, S. S. Kruk, L. Wang, B. Sain, Y. Kivshar, and T. Zentgraf, "Nonlinear imaging with all-dielectric metasurfaces," *Nano letters*, vol. 20, no. 6, pp. 4370–4376, 2020.

[60] S. Liu, P. P. Vabishchevich, A. Vaskin, J. L. Reno, G. A. Keeler, M. B. Sinclair, I. Staude, and I. Brener, "An all-dielectric metasurface as a broadband optical frequency mixer," *Nature communications*, vol. 9, no. 1, pp. 1–6, 2018.

[61] M. R. Shcherbakov, P. P. Vabishchevich, A. S. Shorokhov, K. E. Chong, D.-Y. Choi, I. Staude, A. E. Miroshnichenko, D. N. Neshev, A. A. Fedyanin, and Y. S. Kivshar, "Ultrafast all-optical switching with magnetic resonances in nonlinear dielectric nanostructures," *Nano letters*, vol. 15, no. 10, pp. 6985–6990, 2015.

[62] G. Vampa, B. Ghamsari, S. Siadat Mousavi, T. Hammond, A. Olivieri, E. Lisicka-Skrek, A. Y. Naumov, D. Villeneuve, A. Staudte, P. Berini, *et al.*, "Plasmon-enhanced high-harmonic generation from silicon," *Nature Physics*, vol. 13, no. 7, pp. 659–662, 2017.

[63] M. R. Shcherbakov, H. Zhang, M. Tripepi, G. Sartorello, N. Talisa, A. AlShafey, Z. Fan, J. Twardowski, L. A. Krivitsky, A. I. Kuznetsov, *et al.*, "Generation of even and odd high harmonics in resonant metasurfaces using single and multiple ultra-intense laser pulses," *Nature communications*, vol. 12, no. 1, pp. 1–6, 2021.

[64] C. W. Hsu, B. Zhen, J. Lee, S.-L. Chua, S. G. Johnson, J. D. Joannopoulos, and M. Soljačić, "Observation of trapped light within the radiation continuum," *Nature*, vol. 499, no. 7457, p. 188, 2013.

[65] H. M. Doeleman, F. Monticone, W. Hollander, A. Alù, and A. F. Koenderink, "Experimental observation of a polarization vortex at an optical bound state in the continuum," *Nature Photonics*, p. 1, 2018.

[66] Y. Plotnik, O. Peleg, F. Dreisow, M. Heinrich, S. Nolte, A. Szameit, and M. Segev, "Experimental observation of optical bound states in the continuum," *Physical review letters*, vol. 107, no. 18, p. 183901, 2011.

[67] E. Bulgakov and A. Sadreev, "Fibers based on propagating bound states in the continuum," *Physical Review B*, vol. 98, no. 8, p. 085301, 2018.

[68] Z. Sadrieva, M. Belyakov, M. Balezin, P. Kapitanova, E. Nenasheva, A. Sadreev, and A. Bogdanov, "Experimental observation of a symmetry-protected bound state in the continuum in a chain of dielectric disks," *Physical Review A*, vol. 99, no. 5, p. 053804, 2019.

[69] Y. Akahane, T. Asano, B.-S. Song, and S. Noda, "High-q photonic nanocavity in a two-dimensional photonic crystal," *nature*, vol. 425, no. 6961, pp. 944–947, 2003.

[70] A. B. Matsko and V. S. Ilchenko, "Optical resonators with whispering-gallery modes-part i: basics," *IEEE Journal of selected topics in quantum electronics*, vol. 12, no. 1, pp. 3–14, 2006.

[71] A. Kodigala, T. Lepetit, Q. Gu, B. Bahari, Y. Fainman, and B. Kanté, "Lasing action from photonic bound states in continuum," *Nature*, vol. 541, no. 7636, p. 196, 2017.

[72] M. Wu, S. T. Ha, S. Shendre, E. G. Durmusoglu, W.-K. Koh, D. R. Abujetas, J. A. Sánchez-Gil, R. Paniagua-Dominguez, H. V. Demir, and A. I. Kuznetsov, "Room-temperature lasing in colloidal nanoplatelets via mie-resonant bound states in the continuum," *Nano Letters*, 2020.

[73] S. Han, L. Cong, Y. K. Srivastava, B. Qiang, M. V. Rybin, A. Kumar, R. Jain, W. X. Lim, V. G. Achanta, S. S. Prabhu, *et al.*, "All-dielectric active terahertz photonics driven by bound states in the continuum," *Advanced Materials*, p. 1901921, 2019.

[74] C. Huang, C. Zhang, S. Xiao, Y. Wang, Y. Fan, Y. Liu, N. Zhang, G. Qu, H. Ji, J. Han, L. Ge, Y. Kivshar, and Q. Song, "Ultrafast control of vortex microlasers," *Science*, vol. 367, no. 6481, pp. 1018–1021, 2020.

[75] B. Wang, W. Liu, M. Zhao, J. Wang, Y. Zhang, A. Chen, F. Guan, X. Liu, L. Shi, and J. Zi, "Generating optical vortex beams by momentum-space polarization vortices centred at bound states in the continuum," *Nature Photonics*, pp. 1–6, 2020.

[76] Z. Yu, X. Xi, J. Ma, H. K. Tsang, C.-L. Zou, and X. Sun, "Photonic integrated circuits with bound states in the continuum," *Optica*, vol. 6, no. 10, pp. 1342–1348, 2019.

[77] D. A. Bykov, E. A. Bezus, and L. L. Doskolovich, "Bound states in the continuum and strong phase resonances in integrated gires-tournois interferometer," *Nanophotonics*, vol. 9, no. 1, pp. 83–92, 2020.

[78] C. W. Hsu, B. Zhen, A. D. Stone, J. D. Joannopoulos, and M. Soljačić, "Bound states in the continuum," *Nature Reviews Materials*, vol. 1, no. 9, p. 16048, 2016.

[79] A. F. Sadreev, "Interference traps waves in an open system: bound states in the continuum," *Reports on Progress in Physics*, vol. 84, no. 5, p. 055901, 2021.

[80] A. E. Miroshnichenko, S. Flach, and Y. S. Kivshar, "Fano resonances in nanoscale structures," *Reviews of Modern Physics*, vol. 82, no. 3, p. 2257, 2010.

[81] M. F. Limonov, M. V. Rybin, A. N. Poddubny, and Y. S. Kivshar, "Fano resonances in photonics," *Nature Photonics*, vol. 11, no. 9, pp. 543–554, 2017.

[82] A. E. Miroshnichenko, A. B. Evlyukhin, Y. F. Yu, R. M. Bakker, A. Chipouline, A. I. Kuznetsov, B. Luk'yanchuk, B. N. Chichkov, and Y. S. Kivshar, "Nonradiating anapole modes in dielectric nanoparticles," *Nature communications*, vol. 6, no. 1, pp. 1–8, 2015.

[83] Y. Yang and S. I. Bozhevolnyi, "Nonradiating anapole states in nanophotonics: from fundamentals to applications," *Nanotechnology*, vol. 30, no. 20, p. 204001, 2019.

[84] K. V. Baryshnikova, D. A. Smirnova, B. S. Luk'yanchuk, and Y. S. Kivshar, "Optical anapoles: concepts and applications," *Advanced Optical Materials*, vol. 7, no. 14, p. 1801350, 2019.

[85] J. von Neumann and E. P. Wigner, "Über merkwürdige diskrete eigenwerte," *Z. Physik*, vol. 30, pp. 465–467, 1929.

[86] D. Marinica, A. Borisov, and S. Shabanov, "Bound states in the continuum in photonics," *Physical review letters*, vol. 100, no. 18, p. 183902, 2008.

[87] E. N. Bulgakov and A. F. Sadreev, "Bound states in the continuum in photonic waveguides inspired by defects," *Physical Review B*, vol. 78, no. 7, p. 075105, 2008.

[88] E. N. Bulgakov and A. F. Sadreev, "Bloch bound states in the radiation continuum in a periodic array of dielectric rods," *Physical Review A*, vol. 90, no. 5, p. 053801, 2014.

[89] J. M. Foley, S. M. Young, and J. D. Phillips, “Symmetry-protected mode coupling near normal incidence for narrow-band transmission filtering in a dielectric grating,” *Physical Review B*, vol. 89, no. 16, p. 165111, 2014.

[90] Y. Wang, J. Song, L. Dong, and M. Lu, “Optical bound states in slotted high-contrast gratings,” *JOSA B*, vol. 33, no. 12, pp. 2472–2479, 2016.

[91] E. N. Bulgakov and D. N. Maksimov, “Avoided crossings and bound states in the continuum in low-contrast dielectric gratings,” *Physical Review A*, vol. 98, no. 5, p. 053840, 2018.

[92] X. Gao, B. Zhen, M. Soljacic, H. Chen, and C. W. Hsu, “Bound states in the continuum in fiber bragg gratings,” *ACS Photonics*, 2019.

[93] P. Pankin, B.-R. Wu, J.-H. Yang, K.-P. Chen, I. Timofeev, and A. Sadreev, “One-dimensional photonic bound states in the continuum,” *Communications Physics*, vol. 3, no. 1, pp. 1–8, 2020.

[94] J. Lee, B. Zhen, S.-L. Chua, W. Qiu, J. D. Joannopoulos, M. Soljačić, and O. Shapira, “Observation and differentiation of unique high-q optical resonances near zero wave vector in macroscopic photonic crystal slabs,” *Physical review letters*, vol. 109, no. 6, p. 067401, 2012.

[95] Y. Yang, C. Peng, Y. Liang, Z. Li, and S. Noda, “Analytical perspective for bound states in the continuum in photonic crystal slabs,” *Physical review letters*, vol. 113, no. 3, p. 037401, 2014.

[96] R. Gansch, S. Kalchmair, P. Genevet, T. Zederbauer, H. Detz, A. M. Andrews, W. Schrenk, F. Capasso, M. Lončar, and G. Strasser, “Measurement of bound states in the continuum by a detector embedded in a photonic crystal,” *Light: Science & Applications*, vol. 5, no. 9, p. e16147, 2016.

[97] L. L. Doskolovich, E. A. Bezus, and D. A. Bykov, “Integrated flat-top reflection filters operating near bound states in the continuum,” *arXiv preprint arXiv:1907.04113*, 2019.

[98] D. R. Abujetas, A. Barreda, F. Moreno, J. J. Saenz, A. Litman, J.-M. Geffrin, and J. A. Sanchez-Gil, “Brewster quasi bound states in the continuum in all-dielectric metasurfaces from single magnetic-dipole resonance meta-atoms,” *arXiv preprint arXiv:1902.07148*, 2019.

[99] D. R. Abujetas, A. Barreda, F. Moreno, A. Litman, J.-M. Geffrin, and J. A. Sanchez-Gil, “High-q transparency band in all-dielectric metasurfaces induced by a quasi bound state in the continuum,” *arXiv preprint arXiv:2006.12258*, 2020.

[100] S. A. Dyakov, M. V. Stepikhova, A. A. Bogdanov, A. V. Novikov, D. V. Yurasov, M. V. Shaleev, Z. F. Krasilnik, S. G. Tikhodeev, and N. A. Gippius, “Photonic bound states in the continuum in si structures with the self-assembled ge nanoislands,” *Laser & Photonics Reviews*, vol. 15, no. 7, p. 2000242, 2021.

[101] E. N. Bulgakov and A. F. Sadreev, “Light trapping above the light cone in a one-dimensional array of dielectric spheres,” *Physical Review A*, vol. 92, no. 2, p. 023816, 2015.

[102] E. N. Bulgakov and A. F. Sadreev, “Propagating bloch bound states with orbital angular momentum above the light line in the array of dielectric spheres,” *JOSA A*, vol. 34, no. 6, pp. 949–952, 2017.

[103] Z. Hu and Y. Y. Lu, “Resonances and bound states in the continuum on periodic arrays of slightly noncircular cylinders,” *Journal of Physics B: Atomic, Molecular and Optical Physics*, vol. 51, no. 3, p. 035402, 2018.

[104] S. Kim, K.-H. Kim, and J. F. Cahoon, “Optical bound states in the continuum with nanowire geometric superlattices,” *Physical Review Letters*, vol. 122, no. 18, p. 187402, 2019.

[105] Z. F. Sadrieva, I. S. Sinev, K. L. Koshelev, A. Samusev, I. V. Iorsh, O. Takayama, R. Malureanu, A. A. Bogdanov, and A. V. Lavrinenko, “Transition from optical bound states in the continuum to leaky resonances: role of substrate and roughness,” *Acs Photonics*, vol. 4, no. 4, pp. 723–727, 2017.

[106] S. T. Ha, Y. H. Fu, N. K. Emani, Z. Pan, R. M. Bakker, R. Paniagua-Domínguez, and A. I. Kuznetsov, “Directional lasing in resonant semiconductor nanoantenna arrays,” *Nature nanotechnology*, vol. 13, no. 11, p. 1042, 2018.

[107] K. Koshelev, S. Sychev, Z. F. Sadrieva, A. A. Bogdanov, and I. Iorsh, “Strong coupling between excitons in transition metal dichalcogenides and optical bound states in the continuum,” *Physical Review B*, vol. 98, no. 16, p. 161113, 2018.

[108] V. Kravtsov, E. Khestanova, F. A. Benimetskiy, T. Ivanova, A. K. Samusev, I. S. Sinev, D. Pidgayko, A. M. Mozharov, I. S. Mukhin, M. S. Lozhkin, *et al.*, “Nonlinear polaritons in a monolayer semiconductor coupled to optical bound states in the continuum,” *Light: Science & Applications*, vol. 9, no. 1, pp. 1–8, 2020.

[109] A. Tittl, A. Leitis, M. Liu, F. Yesilkoy, D.-Y. Choi, D. N. Neshev, Y. S. Kivshar, and H. Altug, “Imaging-based molecular barcoding with pixelated dielectric metasurfaces,” *Science*, vol. 360, no. 6393, pp. 1105–1109, 2018.

[110] F. Yesilkoy, E. R. Arvelo, Y. Jahani, M. Liu, A. Tittl, V. Cevher, Y. Kivshar, and H. Altug, “Ultrasensitive hyperspectral imaging and biodetection enabled by dielectric metasurfaces,” *Nature Photonics*, vol. 13, no. 6, pp. 390–396, 2019.

[111] D. R. Abujetas, J. J. Sáenz, and J. A. Sánchez-Gil, “Narrow fano resonances in si nanocylinder metasurfaces: Refractive index sensing,” *Journal of Applied Physics*, vol. 125, no. 18, p. 183103, 2019.

[112] B. Zhen, C. W. Hsu, L. Lu, A. D. Stone, and M. Soljačić, “Topological nature of optical bound states in the continuum,” *Physical review letters*, vol. 113, no. 25, p. 257401, 2014.

[113] B. Bahari, F. Vallini, T. Lepetit, R. Tellez-Limon, J. Park, A. Kodigala, Y. Fainman, and B. Kante, “Integrated and steerable vortex lasers,” *arXiv preprint arXiv:1707.00181*, 2017.

[114] X. Yin, J. Jin, M. Soljačić, C. Peng, and B. Zhen, “Observation of topologically enabled unidirectional guided resonances,” *Nature*, vol. 580, no. 7804, pp. 467–471, 2020.

[115] J. Jin, X. Yin, L. Ni, M. Soljačić, B. Zhen, and C. Peng, “Topologically enabled ultrahigh-q guided resonances robust to out-of-plane scattering,” *Nature*, vol. 574, no. 7779, pp. 501–504, 2019.

[116] K. Koshelev and Y. Kivshar, “Light trapping gets a boost,” 2019.

[117] M.-S. Hwang, H.-C. Lee, K.-H. Kim, K.-Y. Jeong, S.-H. Kwon, K. Koshelev, Y. Kivshar, and H.-G. Park, “Ultralow-threshold laser using super-bound states in the continuum,” *Nature Communications*, vol. 12, no. 1, pp. 1–9, 2021.

[118] A. Overvig, N. Yu, and A. Alu, “Chiral quasi-bound states in the continuum,” *arXiv preprint arXiv:2006.05484*, 2020.

[119] M. V. Gorkunov, A. A. Antonov, and Y. S. Kivshar, “Metasurfaces with maximum chirality empowered by bound states in the continuum,” *arXiv preprint arXiv:2006.15884*, 2020.

[120] M. V. Gorkunov, A. A. Antonov, V. R. Tuz, A. S. Kupriianov, and Y. S. Kivshar, “Bound states in the continuum underpin near-lossless maximum chirality in dielectric metasurfaces,” *Advanced Optical Materials*, p. 2100797, 2021.

[121] V. R. Tuz, V. V. Khardikov, A. S. Kupriianov, K. L. Domina, S. Xu, H. Wang, and H.-B. Sun, “High-quality trapped modes in all-dielectric metamaterials,” *Optics express*, vol. 26, no. 3, pp. 2905–2916, 2018.

[122] V. Fedotov, M. Rose, S. Prosvirnin, N. Papasimakis, and N. Zheludev, “Sharp trapped-mode resonances in planar metamaterials with a broken structural symmetry,” *Physical review letters*, vol. 99, no. 14, p. 147401, 2007.

[123] A. Forouzmand and H. Mosallaei, “All-dielectric c-shaped nanoantennas for light manipulation: Tailoring both magnetic and electric resonances to the desire,” *Advanced Optical Materials*, vol. 5, no. 14, p. 1700147, 2017.

[124] A. B. Evlyukhin, S. I. Bozhevolnyi, A. Pors, M. G. Nielsen, I. P. Radko, M. Willatzen, and O. Albrektsen, “Detuned electrical dipoles for plasmonic sensing,” *Nano letters*, vol. 10, no. 11, pp. 4571–4577, 2010.

[125] F. Zhang, X. Huang, Q. Zhao, L. Chen, Y. Wang, Q. Li, X. He, C. Li, and K. Chen, “Fano resonance of an asymmetric dielectric wire pair,” *Applied Physics Letters*, vol. 105, no. 17, p. 172901, 2014.

[126] S. Campione, S. Liu, L. I. Basilio, L. K. Warne, W. L. Langston, T. S. Luk, J. R. Wendt, J. L. Reno, G. A. Keeler, I. Brener, *et al.*, "Broken symmetry dielectric resonators for high quality factor fano metasurfaces," *ACS Photonics*, vol. 3, no. 12, pp. 2362–2367, 2016.

[127] P. P. Vabishchevich, S. Liu, M. B. Sinclair, G. A. Keeler, G. M. Peake, and I. Brener, "Enhanced second-harmonic generation using broken symmetry iii–v semiconductor fano metasurfaces," *ACS Photonics*, 2018.

[128] W. X. Lim and R. Singh, "Universal behaviour of high-q fano resonances in metamaterials: terahertz to near-infrared regime," *Nano convergence*, vol. 5, no. 1, p. 5, 2018.

[129] V. V. Khardikov, E. O. Iarko, and S. L. Prosvirnin, "Trapping of light by metal arrays," *Journal of Optics*, vol. 12, no. 4, p. 045102, 2010.

[130] R. Singh, I. A. Al-Naib, Y. Yang, D. Roy Chowdhury, W. Cao, C. Rockstuhl, T. Ozaki, R. Morandotti, and W. Zhang, "Observing metamaterial induced transparency in individual fano resonators with broken symmetry," *Applied Physics Letters*, vol. 99, no. 20, p. 201107, 2011.

[131] S. I. Bozhevolnyi, A. B. Evlyukhin, A. Pors, M. G. Nielsen, M. Willatzen, and O. Albrektsen, "Optical transparency by detuned electrical dipoles," *New Journal of Physics*, vol. 13, no. 2, p. 023034, 2011.

[132] Y. Yang, I. I. Kravchenko, D. P. Briggs, and J. Valentine, "All-dielectric metasurface analogue of electromagnetically induced transparency," *Nature communications*, vol. 5, p. 5753, 2014.

[133] J. Hu, T. Lang, Z. Hong, C. Shen, and G. Shi, "Comparison of electromagnetically induced transparency performance in metallic and all-dielectric metamaterials," *Journal of Lightwave Technology*, vol. 36, no. 11, pp. 2083–2093, 2018.

[134] W. Cao, R. Singh, C. Zhang, J. Han, M. Tonouchi, and W. Zhang, "Plasmon-induced transparency in metamaterials: Active near field coupling between bright superconducting and dark metallic mode resonators," *Applied Physics Letters*, vol. 103, no. 10, p. 101106, 2013.

[135] A. Jain, P. Tassin, T. Koschny, and C. M. Soukoulis, "Large quality factor in sheet metamaterials made from dark dielectric meta-atoms," *Physical review letters*, vol. 112, no. 11, p. 117403, 2014.

[136] E. Bochkova, S. N. Burokur, A. de Lustrac, and A. Lupu, "Direct dark modes excitation in bi-layered enantiomeric atoms-based metasurface through symmetry matching," *Optics letters*, vol. 41, no. 2, pp. 412–415, 2016.

[137] L. D. Landau and E. M. Lifshitz, *Quantum mechanics: non-relativistic theory*, vol. 3. Elsevier, 2013.

[138] M. O. Scully and M. S. Zubairy, “Quantum optics,” 1999.

[139] H. Friedrich and D. Wintgen, “Interfering resonances and bound states in the continuum,” *Physical Review A*, vol. 32, pp. 3231–3242, dec 1985.

[140] H. Cao and J. Wiersig, “Dielectric microcavities: Model systems for wave chaos and non-hermitian physics,” *Reviews of Modern Physics*, vol. 87, no. 1, p. 61, 2015.

[141] C. Schinke, P. Christian Peest, J. Schmidt, R. Brendel, K. Bothe, M. R. Vogt, I. Kröger, S. Winter, A. Schirmacher, S. Lim, *et al.*, “Uncertainty analysis for the coefficient of band-to-band absorption of crystalline silicon,” *AIP Advances*, vol. 5, no. 6, p. 067168, 2015.

[142] A. B. Evlyukhin, T. Fischer, C. Reinhardt, and B. N. Chichkov, “Optical theorem and multipole scattering of light by arbitrarily shaped nanoparticles,” *Physical Review B*, vol. 94, no. 20, p. 205434, 2016.

[143] E. A. Muljarov, W. Langbein, and R. Zimmermann, “Brillouin-wigner perturbation theory in open electromagnetic systems,” *EPL (Europhysics Letters)*, vol. 92, no. 5, p. 50010, 2011.

[144] T. Weiss, M. Mesch, M. Schäferling, H. Giessen, W. Langbein, and E. A. Muljarov, “From dark to bright: first-order perturbation theory with analytical mode normalization for plasmonic nanoantenna arrays applied to refractive index sensing,” *Physical review letters*, vol. 116, no. 23, p. 237401, 2016.

[145] B. Gallinet and O. J. Martin, “Ab initio theory of fano resonances in plasmonic nanostructures and metamaterials,” *Physical Review B*, vol. 83, no. 23, p. 235427, 2011.

[146] E. N. Bulgakov and D. N. Maksimov, “Light enhancement by quasi-bound states in the continuum in dielectric arrays,” *Optics Express*, vol. 25, no. 13, pp. 14134–14147, 2017.

[147] E. E. Maslova, M. V. Rybin, A. A. Bogdanov, and Z. F. Sadrieva, “Bound states in the continuum in periodic structures with structural disorder,” *Nanophotonics*, vol. 10, no. 17, pp. 4313–4321, 2021.

[148] J. Kühne, J. Wang, T. Weber, L. Kühner, S. A. Maier, and A. Tittl, “Fabrication robustness in bic metasurfaces,” *Nanophotonics*, vol. 10, no. 17, pp. 4305–4312, 2021.

[149] S. Fan, W. Suh, and J. D. Joannopoulos, “Temporal coupled-mode theory for the fano resonance in optical resonators,” *JOSA A*, vol. 20, no. 3, pp. 569–572, 2003.

[150] S. A. Maier, “Plasmonic field enhancement and sers in the effective mode volume picture,” *Optics Express*, vol. 14, no. 5, pp. 1957–1964, 2006.

[151] S. Both and T. Weiss, “Resonant states and their role in nanophotonics,” *Semiconductor Science and Technology*, vol. 37, no. 1, p. 013002, 2021.

[152] T. J. Seok, A. Jamshidi, M. Kim, S. Dhuey, A. Lakhani, H. Choo, P. J. Schuck, S. Cabrini, A. M. Schwartzberg, J. Bokor, *et al.*, "Radiation engineering of optical antennas for maximum field enhancement," *Nano letters*, vol. 11, no. 7, pp. 2606–2610, 2011.

[153] C. Cui, C. Zhou, S. Yuan, X. Qiu, L. Zhu, Y. Wang, Y. Li, J. Song, Q. Huang, Y. Wang, *et al.*, "Multiple fano resonances in symmetry-breaking silicon metasurface for manipulating light emission," *ACS Photonics*, vol. 5, no. 10, pp. 4074–4080, 2018.

[154] A. Ndao, L. Hsu, W. Cai, J. Ha, J. Park, R. Contractor, Y. Lo, and B. Kanté, "Differentiating and quantifying exosome secretion from a single cell using quasi-bound states in the continuum," *Nanophotonics*, vol. 1, no. ahead-of-print, 2020.

[155] Z. Liu, Y. Xu, Y. Lin, J. Xiang, T. Feng, Q. Cao, J. Li, S. Lan, and J. Liu, "High-q quasibound states in the continuum for nonlinear metasurfaces," *Physical review letters*, vol. 123, no. 25, p. 253901, 2019.

[156] R. W. Boyd, *Nonlinear optics.* Academic press, 2020.

[157] J. Lee, M. Tymchenko, C. Argyropoulos, P.-Y. Chen, F. Lu, F. Demmerle, G. Boehm, M.-C. Amann, A. Alu, and M. A. Belkin, "Giant nonlinear response from plasmonic metasurfaces coupled to intersubband transitions," *Nature*, vol. 511, no. 7507, pp. 65–69, 2014.

[158] W. Tong, C. Gong, X. Liu, S. Yuan, Q. Huang, J. Xia, and Y. Wang, "Enhanced third harmonic generation in a silicon metasurface using trapped mode," *Optics express*, vol. 24, no. 17, pp. 19661–19670, 2016.

[159] S. Ghimire and D. A. Reis, "High-harmonic generation from solids," *Nature physics*, vol. 15, no. 1, pp. 10–16, 2019.

[160] G. Vampa, C. McDonald, G. Orlando, D. Klug, P. Corkum, and T. Brabec, "Theoretical analysis of high-harmonic generation in solids," *Physical review letters*, vol. 113, no. 7, p. 073901, 2014.

[161] Y. Yang, J. Lu, A. Manjavacas, T. S. Luk, H. Liu, K. Kelley, J.-P. Maria, E. L. Runnerstrom, M. B. Sinclair, S. Ghimire, *et al.*, "High-harmonic generation from an epsilon-near-zero material," *Nature Physics*, vol. 15, no. 10, pp. 1022–1026, 2019.

[162] M. R. Shcherbakov, K. Werner, Z. Fan, N. Talisa, E. Chowdhury, and G. Shvets, "Photon acceleration and tunable broadband harmonics generation in nonlinear time-dependent metasurfaces," *Nature communications*, vol. 10, no. 1, pp. 1–9, 2019.

[163] S. A. Akhmanov, A. P. Sukhorukov, and R. V. Khokhlov, "Self-focusing and diffraction of light in a nonlinear medium," *Soviet physics USPEKHI*, vol. 10, no. 5, p. 609, 1968.

[164] N. Karl, P. P. Vabishchevich, M. R. Shcherbakov, S. Liu, M. B. Sinclair, G. Shvets, and I. Brener, "Frequency conversion in a time-variant dielectric metasurface," *Nano Letters*, vol. 20, no. 10, pp. 7052–7058, 2020.

[165] V. V. Zubyuk, P. A. Shafirin, M. R. Shcherbakov, G. Shvets, and A. A. Fedyanin, "Externally driven nonlinear time-variant metasurfaces," *ACS Photonics*, 2020.

[166] L. Keldysh *et al.*, "Ionization in the field of a strong electromagnetic wave," *Sov. Phys. JETP*, vol. 20, no. 5, pp. 1307–1314, 1965.

[167] P. Balling and J. Schou, "Femtosecond-laser ablation dynamics of dielectrics: basics and applications for thin films," *Reports on progress in physics*, vol. 76, no. 3, p. 036502, 2013.

[168] L. Zhang, R. Gogna, W. Burg, E. Tutuc, and H. Deng, "Photonic-crystal exciton-polaritons in monolayer semiconductors," *Nature communications*, vol. 9, no. 1, pp. 1–8, 2018.

[169] A. S. Solntsev, G. S. Agarwal, and Y. S. Kivshar, "Metasurfaces for quantum photonics," *Nature Photonics*, vol. 15, no. 5, pp. 327–336, 2021.

[170] X. Yin, Z. Ye, D. A. Chenet, Y. Ye, K. O'Brien, J. C. Hone, and X. Zhang, "Edge nonlinear optics on a mos2 atomic monolayer," *Science*, vol. 344, no. 6183, pp. 488–490, 2014.

[171] A. Dasgupta, J. Gao, and X. Yang, "Atomically thin nonlinear transition metal dichalcogenide holograms," *Nano letters*, vol. 19, no. 9, pp. 6511–6516, 2019.

[172] A. Autere, H. Jussila, Y. Dai, Y. Wang, H. Lipsanen, and Z. Sun, "Nonlinear optics with 2d layered materials," *Advanced Materials*, vol. 30, no. 24, p. 1705963, 2018.

[173] X. Han, K. Wang, P. D. Persaud, X. Xing, W. Liu, H. Long, F. Li, B. Wang, M. R. Singh, and P. Lu, "Harmonic resonance enhanced second-harmonic generation in the monolayer ws2–ag nanocavity," *Acs Photonics*, vol. 7, no. 3, pp. 562–568, 2020.

[174] D. R. Abujetas, J. Olmos-Trigo, J. J. Sáenz, and J. A. Sánchez-Gil, "Coupled electric and magnetic dipole formulation for planar arrays of particles: Resonances and bound states in the continuum for all-dielectric metasurfaces," *Physical Review B*, vol. 102, no. 12, p. 125411, 2020.

[175] U. Zywietz, A. B. Evlyukhin, C. Reinhardt, and B. N. Chichkov, "Laser printing of silicon nanoparticles with resonant optical electric and magnetic responses," *Nature communications*, vol. 5, no. 1, pp. 1–7, 2014.

[176] C. F. Bohren and D. R. Huffman, *Absorption and scattering of light by small particles*. John Wiley & Sons, 2008.

[177] C. J. Foot, *Atomic physics*, vol. 7. OUP Oxford, 2004.

[178] A. B. Evlyukhin, C. Reinhardt, and B. N. Chichkov, "Multipole light scattering by nonspherical nanoparticles in the discrete dipole approximation," *Physical Review B*, vol. 84, no. 23, p. 235429, 2011.

[179] P. D. Terekhov, V. E. Babicheva, K. V. Baryshnikova, A. S. Shalin, A. Karabchevsky, and A. B. Evlyukhin, “Multipole analysis of dielectric metasurfaces composed of nonspherical nanoparticles and lattice invisibility effect,” *Physical Review B*, vol. 99, no. 4, p. 045424, 2019.

[180] S. Gladishev, K. Frizyuk, and A. Bogdanov, “Symmetry analysis and multipole classification of eigenmodes in electromagnetic resonators for engineering their optical properties,” *arXiv preprint arXiv:2002.11411*, 2020.

[181] P. Grahn, A. Shevchenko, and M. Kaivola, “Electromagnetic multipole theory for optical nanomaterials,” *New Journal of Physics*, vol. 14, no. 9, p. 093033, 2012.

[182] M. Kerker, D.-S. Wang, and C. Giles, “Electromagnetic scattering by magnetic spheres,” *JOSA*, vol. 73, no. 6, pp. 765–767, 1983.

[183] S. Person, M. Jain, Z. Lapin, J. J. Sáenz, G. Wicks, and L. Novotny, “Demonstration of zero optical backscattering from single nanoparticles,” *Nano letters*, vol. 13, no. 4, pp. 1806–1809, 2013.

[184] W. Liu and Y. S. Kivshar, “Generalized kerker effects in nanophotonics and meta-optics,” *Optics express*, vol. 26, no. 10, pp. 13085–13105, 2018.

[185] V. Savinov, N. Papasimakis, D. Tsai, and N. Zheludev, “Optical anapoles,” *Communications Physics*, vol. 2, no. 1, pp. 1–4, 2019.

[186] F. Monticone, D. Sounas, A. Krasnok, and A. Alù, “Can a nonradiating mode be externally excited? nonscattering states vs. embedded eigenstates,” *arXiv preprint arXiv:1908.00956*, 2019.

[187] F. Monticone and A. Alu, “Embedded photonic eigenvalues in 3d nanostructures,” *Physical Review Letters*, vol. 112, no. 21, p. 213903, 2014.

[188] I. Liberal and N. Engheta, “Nonradiating and radiating modes excited by quantum emitters in open epsilon-near-zero cavities,” *Science advances*, vol. 2, no. 10, p. e1600987, 2016.

[189] M. B. Doost, W. Langbein, and E. A. Muljarov, “Resonant-state expansion applied to three-dimensional open optical systems,” *Physical Review A*, vol. 90, no. 1, p. 013834, 2014.

[190] E. Muljarov, “Full electromagnetic green’s dyadic of spherically symmetric open optical systems and elimination of static modes from the resonant-state expansion,” *Physical Review A*, vol. 101, no. 5, p. 053854, 2020.

[191] M. I. Mishchenko, L. D. Travis, and D. W. Mackowski, “T-matrix computations of light scattering by nonspherical particles: A review,” *Journal of Quantitative Spectroscopy and Radiative Transfer*, vol. 55, no. 5, pp. 535–575, 1996.

[192] J. D. Jackson, “Classical electrodynamics,” 1999.

[193] E. Nenasheva, L. Mudroliubova, and N. Kartenko, “Microwave dielectric properties of ceramics based on catio3–lnmo3 system (ln–la, nd; m–al, ga),” *Journal of the European Ceramic Society*, vol. 23, no. 14, pp. 2443–2448, 2003.

[194] O. Sager and F. Tisi, “On eigenmodes and forced resonance-modes of dielectric spheres,” *Proceedings of the IEEE*, vol. 56, no. 9, pp. 1593–1594, 1968.

[195] M. Celebrano, X. Wu, M. Baselli, S. Großmann, P. Biagioni, A. Locatelli, C. De Angelis, G. Cerullo, R. Osellame, B. Hecht, *et al.*, “Mode matching in multiresonant plasmonic nanoantennas for enhanced second harmonic generation,” *Nature nanotechnology*, vol. 10, no. 5, pp. 412–417, 2015.

[196] M. R. Shcherbakov, P. Shafirin, and G. Shvets, “Overcoming the efficiency-bandwidth tradeoff for optical harmonics generation using nonlinear time-variant resonators,” *Physical Review A*, vol. 100, no. 6, p. 063847, 2019.

[197] K. Frizyuk, I. Volkovskaya, D. Smirnova, A. Poddubny, and M. Petrov, “Second-harmonic generation in mie-resonant dielectric nanoparticles made of noncentrosymmetric materials,” *Physical Review B*, vol. 99, no. 7, p. 075425, 2019.

[198] L. Carletti, A. Locatelli, D. Neshev, and C. De Angelis, “Shaping the radiation pattern of second-harmonic generation from algaas dielectric nanoantennas,” *ACS Photonics*, vol. 3, no. 8, pp. 1500–1507, 2016.

[199] J. Van de Groep and A. Polman, “Designing dielectric resonators on substrates: Combining magnetic and electric resonances,” *Optics express*, vol. 21, no. 22, pp. 26285–26302, 2013.

[200] N. M. Litchinitser, “Structured light meets structured matter,” *Science*, vol. 337, no. 6098, pp. 1054–1055, 2012.

[201] T. Weiss and E. A. Muljarov, “How to calculate the pole expansion of the optical scattering matrix from the resonant states,” *Physical Review B*, vol. 98, no. 8, p. 085433, 2018.

[202] E. A. Muljarov and T. Weiss, “Resonant-state expansion for open optical systems: generalization to magnetic, chiral, and bi-anisotropic materials,” *Optics letters*, vol. 43, no. 9, pp. 1978–1981, 2018.

[203] Z. Ruan and S. Fan, “Temporal coupled-mode theory for light scattering by an arbitrarily shaped object supporting a single resonance,” *Physical review A*, vol. 85, no. 4, p. 043828, 2012.

[204] F. Alpeggiani, N. Parappurath, E. Verhagen, and L. Kuipers, “Quasinormal-mode expansion of the scattering matrix,” *Physical Review X*, vol. 7, no. 2, p. 021035, 2017.